

Exploring Intensity Mapping Techniques Via Simulations

A thesis submitted in fulfilment of the requirements for the degree
of **Doctor of Philosophy**
in the Department of Physics and Electronics,
Rhodes University

Supervisors:

Author:

Theophilus ANSAH-NARH

Prof. Oleg M. SMIRNOV

Prof. Filipe B. ABDALLA

Dr. Khan M. B. ASAD

February 02, 2019

Statement of Originality

I, ANSAH-NARH Theophilus, assert that the ideas contained in this thesis are my own, and so the thesis has not been formerly put forward for a qualification at any other tertiary institution.

Signed:

Date:

Publications

This research is largely drawn from the following publications:

- T. Ansah-Narh, F. B. Abdalla, O. M. Smirnov, K. M. B. Asad and J. R. Shaw, (2018). Simulations of Systematic Direction-dependent Instrumental Effects in Intensity Mapping Experiments. *Monthly Notices of the Royal Astronomical Society*, 481 (2), 2694–2710.
- K. M. B. Asad, J. N. Girard, M. de Villiers, T. Ansah-Narh, K. Iheanetu, O. Smirnov, M. G. Santos, R. Lehmensiek, K. Thorat, S. Makhathini and others, Primary Beam Effects of Radio Astronomy Antennas – II. Modelling the MeerKAT L-band beam using holography. *Monthly Notices of the Royal Astronomical Society*, accepted.

I hereby confirm that some of the text and figures from these have been reproduced directly. In addition, where I have mentioned the work published by others, credit has been given to this effect.

Abstract

The study used intensity mapping technique to observe the combined radio emissions of CO and HI emanating from a diffuse source. Antenna elements with short separations like KAT-7 (not in operation now) and SKA1-mid can be used for such observation. Despite the potential of this technique, it is subject to exact foreground reduction of continuum signal from the Milky Way galaxy and other radio sources beyond. In addition, the signal is dominated by direction-dependent effects and the primary beam being the most serious effect, since it controls the full intensity of the measured signal. Furthermore, the inaccuracies in the receivers, cause part of the foreground to seep into the absolute intensity, making it difficult to observe the CO or HI signal. For the current on-going SKA instruments and future aperture arrays, these will be affected by antenna pointing errors and polarization leakages. To address these problems, first, we create a dense set of dipole positions with a complete secondary blockage to mimic the illumination pattern of KAT-7-like dish. Second, we use Zernike model to reconstruct MeerKAT L-band beams and then third, we try to simulate EM beams of SKA1-mid as an optical telescope. Next we perturb these beams by introducing realistic errors in them. We then simulate these beams (true and corrupted) with the foreground to estimate for the CO and HI signal. At the end, our simulation shows that, if we consider a correct model of the primary beam, then the intrinsic partial leakage of linear polarization ($|Q + iU|_T \rightarrow I$) is given at $\approx 1.0\%$. Furthermore, when we correct for the beam errors in Stokes I then, it is possible to evaluate the angular spectrum of both CO and HI at a multipole moment of $l \lesssim 50$, however, this is vice versa if we do calibrate for the beam errors. Finally, the study shows that, Zernike and convolution techniques are good models for intensity mapping experiments.

Acknowledgements

The completion of this research is made up of immense inputs from many people to whom I owe a debt of gratitude. First and foremost, I thank my supervisors: Prof. Oleg M. Smirnov who doubles as the SKA Chair in Radio Astronomy Techniques and Technologies (RATT), which is hosted by Rhodes University and my main supervisor, particularly, for the strong affection he puts in everything he does and for his enormous understanding in Computational Mathematics and Radio Interferometry, Prof. Filipe B. Abdalla, for his expertise in Cosmology and Intensity Mapping Experiments and for the patience he had in supporting me especially during the first year of the research. Also, Dr. Khan M. B. Asad for his understanding in Intensity Mapping Experiments. I also show my appreciation to everyone who directly took part in the realisation of this work, particularly to Dr. Richard Shaw for helping me out with the foreground simulations and Dr. Jamie Leech for teaching me how to use the GRASP software. My course mates deserve the best recognition. Sphe, Marcel, Ridhima, Liju, Kela, Alex and the others have been wonderful companions throughout the study period. I would like to thank my family, Mr. Francis D. Narh (father), Mrs. Salome Nortey (mother), Samuel Annor Narh (brother), Esther Amatsu Narh, Christiana Koryoonmaatso Narh (sisters), Patricia Opoku (wife), Adelaide and Salome (daughters) for their love and trust. Lastly, I am very grateful to the SKA and NRF for supporting this research.

Contents

Statement of Originality	i
Publications	ii
Abstract	iii
Acknowledgements	iv
List of Figures	ix
List of Tables	x
1 Introduction	1
1.1 The 21 cm Radio Emission Line	1
1.2 HI Intensity Mapping	2
1.3 Significance of Intensity Mapping Techniques	3
1.4 Problem Identification	4
1.5 Research Objective	5
1.6 Delimitation	6
1.7 Rationale and Motivation	6
1.8 Thesis Layout	6
2 Radio Antennas and Interferometry	8
2.1 Introduction	8
2.2 Antenna Parameters	9
2.2.1 Antenna Field Regions	10
2.2.2 Radiation Patterns	11
2.2.3 Radiation Intensity	12
2.2.4 Gain	12
2.3 EM Wave Polarization	12
2.3.1 Derivation of the Stokes Polarization Parameters	14
2.4 Antenna Arrays	16
2.4.1 Mathematical Formulation of Antenna Array	16

2.4.2	Beam-forming	17
2.4.3	Types of Radio Arrays	18
2.4.3.1	Phased-Array Feeds (PAFs)	18
2.4.3.2	Transiting Arrays	19
2.4.3.3	Aperture Arrays	19
2.5	Power gained from Radio Sources	20
2.6	Basic Concepts of Radio Interferometry	21
3	Radio Foregrounds and Rotation Measure Synthesis	23
3.1	Galactic Foreground	23
3.1.1	Diffuse Galactic Synchrotron Emission	24
3.2	Faraday Rotation Measure Synthesis	26
3.3	Simulation	27
4	Investigating Primary Beam Effects on HI Intensity Mapping	31
4.1	Modelling the Primary Beam	31
4.2	KAT-7 Beam Pattern Simulation	33
4.2.1	Jones and Mueller matrices	36
4.2.2	Primary Beam Perturbation	39
4.3	Convolution of Foreground Maps	40
4.3.1	Angular Power Spectrum	42
4.4	Results and Analysis	43
4.5	Conclusions	46
5	MeerKAT L-Band Primary Beams: Effects of HI Intensity Mapping	48
5.1	Introduction	48
5.2	Methodology	50
5.2.1	Mathematical Basis of Zernike Polynomials	50
5.2.2	Numerical Computation of Zernike Coefficients	52
5.2.3	Spatial Representation	52
5.2.4	Spectral Representation	54
5.3	Results and Discussion	57
5.4	Conclusion	58
6	SKA1-mid Multiband Primary Beams: Effects of HI and CO Intensity Mapping Experiments	60
6.1	Introduction	60
6.2	GRASP Beam Measurement	61
6.2.1	Model Specification	61
6.2.1.1	Reflector Antenna Models	61

6.2.1.2	Feed Models	62
6.3	Modelling EM Beams	62
6.3.1	Fitting 2D Zernike Polynomials on EM Beams	63
6.3.1.1	Spatial Representation	63
6.3.1.2	Spectral Representation	67
6.3.2	Model Beam Perturbation	67
6.3.3	Intrinsic Cross-Polarisation (IXR)	70
6.4	The CO Power Spectrum	71
6.5	Results and Analysis	72
6.6	Conclusion	78
7	Conclusions and Recommendations	80
Appendices		82
A	OSKAR BEAMPATTERN AND FOREGROUND SIMULATIONS	83
A.1	Modelled and measured beams	83
A.2	Measured Full-sky maps	85
B	Zernike Polynomial Sequence	88
B.1	Orthonormality	88
Bibliography		97

List of Figures

1.1	When the electron of a neutral hydrogen atom flips its spin, energy is released at a wavelength of 21 cm. This figure is obtained from [38, pg. 113].	2
1.2	Simulated variations in the 21 cm emission brightness temperature. The red rings in (a) show how to perform IM experiment by observing multiple patches in the sky with the radio telescope in order to measure the 21 cm emission to produce (b). Note that this figure is very similar to the one discussed in [86].	3
2.1	An illustration of the various field distributions at each field zone. <i>Source:</i> This figure is reproduced from [10, pg. 35] but originally produced by [90].	11
2.2	(a) Antenna radiation pattern showing the various lobes in angular scales. (b) Linear projection of the pattern in (a). <i>Source:</i> Obtained from [10, pg. 30]	11
2.3	The diagram shows how a polarizing element can polarize an unpolarized wave and also rotate the direction of incoming polarized wave.	13
2.4	PAFs showing the wide gain in the FoV. The third image from the left is the installation of APERTIF on WSRT. The last image from the left displays the PAFs fixed on ASKAP. <i>Source:</i> Reproduced from [43].	19
2.5	Transiting Arrays:- PAPER (top-left), LWA (bottom-left), Medicina Northern Cross (top-right) and MWA (bottom-right).	19
2.6	Aperture Array:- LOFAR.	20
2.7	SKA-2 Dense Aperture Arrays precursor telescope.	20
3.1	Brightness temperature distribution for the components of the Galactic foregrounds with respect to frequency. The angular resolution for the temperature of each smooth component is 1° . <i>Credit:</i> This figure is obtained from [88].	24

3.2	408 MHz Full-Sky Map [52] projected in HEALPix, ring and defined in Galactic coordinates. Data and images can be retrieved from the LAMBDA website.	25
3.3	1000 MHz full-sky simulated synchrotron maps. These synchrotron maps characterize the full-sky polarization maps for our low resolution simulated observations and are presented here in the mollweide projection form defined by equatorial coordinates in terms of Stokes parameters I, Q, U and V	28
3.4	Simulated foreground maps at 950 MHz displayed in mollweide form.	29
3.5	Simulated foreground maps at 450 MHz presented in mollweide form.	29
3.6	Simulated foreground maps at 990.5 MHz displayed in mollweide form.	29
3.7	Simulated foreground maps at 13.6 GHz presented in mollweide form.	30
4.1	The aperture illumination of dish-like surface is modelled using 80000 dipoles. LEFT PLOT: The ‘flat-top Gaussian’ radial distribution of dipole positions, mimicking a realistic aperture illumination where the dipoles get less dense towards the edge of the dish. RIGHT PLOT: The resulting 2D dipole distribution with a mask applied to mimic aperture blockage.	34
4.2	Jones matrix representation of the KAT-7-like beams produced by OSKAR and shown at 1 GHz: (a) real part (b) imaginary part. The intensity of the imaginary parts increases with fewer dipoles and becomes smaller when more dipoles are used. The four panels in (a) and (b) show XX (top-left), XY (top-right), YX (bottom-left) and YY (bottom-right). Note that the notations X and Y denote the horizontal and vertical linear polarised beams.	35
4.3	Histogram plots of the imaginary components in Fig. 4.2 showing the distribution of inaccuracies on the KAT-7 dish-like surface.	35
4.4	Mueller matrix representations of full polarization beams produced at 1 GHz (a) 4×4 images of KAT-7 uncorrupted OSKAR beams. (b) Fractional differences between the uncorrupted OSKAR beams in Fig. 4.4a and the gain and phase error beams in appendix A.1a (c) Fractional differences between uncorrupted OSKAR beams in Fig. 4.4a and the dipole orientation error beams in appendix A.1b. (d) Fractional differences between VLA holography measured beams in Figs. A.2a and A.2b.	38

4.5 Convolved full-sky polarization maps using the non-distorted OS-KAR beams. For example, we used the m_{II} beam in Fig. 4.4a to convolve Stokes I in Fig. 3.3 and produce the convolved map $I \rightarrow I$, then we used m_{QI} beam to convolve Stokes Q to obtain the convolved map $Q \rightarrow I$, also, using the m_{UI} beam to convolve Stokes U we produced the convolved map $U \rightarrow I$. The other convolved maps are produced in the same manner using their respective beams.	42
4.6 The 1 st row maps depict the measured foregrounds of Stokes I , Q and U for using the non-distorted fully polarised beams in Fig. 4.4a whilst the 2 nd and 3 rd rows represent the corrupted measured foregrounds due to gain and phase and dipole orientation errors introduced into the beams respectively. The next two maps are the corresponding errors in I , Q and U	43
4.7 Convolved angular power spectra estimation of foreground maps. First row: Shows Stokes I spectra plots for using simulated beams and holography measured beams. Second row: Displays Stokes Q spectra plots for using simulated beams and holography measured beams. Third row: Displays Stokes U spectra plots for using simulated beams and holography measured beams.	44
4.8 These are the spectra plots of the systematic errors as shown in Fig. A.3. The notations GP and XY in the legends denote the residuals for gain-phase and surface orientation errors in the simulated modelled beams, that of HB depicts the errors in the holography beams. These errors are then used to estimate the imperfections in the simulation by computing the expected value of the standard deviations of the sampling distributions of the residual maps to produce Table 4.1.	45

4.9	The spectra plots compare the effect of recovering the cosmological 21 cm signal by calibrating for the beam errors in Stokes I to when there is no beam correction at all. The solid circular spectrum is the simulated 21 cm brightness temperature described by [4] at a $z \approx 0.67$. LEFT SIDE PLOT: Here, we show how to estimate the 21 cm signal when we correct the errors in Stokes I . RIGHT SIDE PLOT: We quantify the amount of leakages into Stokes I when we do not perform any beam correction. The spectrum ($ Q + iU _T$), is the intrinsic leakage in I when we adopt true modelled beams as shown in Fig. 4.4a. The other plots ($ Q + iU _{GP}$, $ Q + iU _{XY}$, $ Q + iU _{VLA}$) are the leakages in I when we use perturbed modelled beams (i.e., gain, phase and main dish surface orientation errors) and holography measured beams respectively.	46
5.1	The distribution of the 64 antennas of MeerKAT, each identified by an integer ranging from 0 to 63. Note that the actual names of the antennas are given as M000, M001, M002 and so on. Left: The distribution outside the 1 km core. Right: The distribution inside the 1 km core is loosely delimited by a hexagonal boundary. The West-East and South-North distances are shown relative to the arbitrary centre located at $-30^{\circ}42'47.41''$ South, $21^{\circ}26'38.00''$ East.	49
5.2	The raster scanning patterns of three of the astro-holographic observations of MeerKAT. The title indicates the observation ID. More information about the observations can be found in Table 1 and inside the text.	49
5.3	Expansion of eight orthogonal radial polynomial $R^{ \alpha }(\rho)$ plots. Here, the value of unity can be obtained at the outer edge, since $R_\beta^{ \alpha }(1) = 1$	51
5.4	Representation of basis patterns of Zernike moments $Z_\beta^\alpha(\rho, \theta)$ of order 6, plotted on a unit circle.	51
5.5	The expected value of the squared error loss between the holography beam and the predicted beam model with respect to increase in the number of Zernike modes. (XX, YY) and (XY,YX) are the linear polarization for the gain and cross terms of the Jones beams respectively.	53

5.6	Zernike reconstructed MeerKAT beam model at 990 MHz, using 20 and 5 strongest coefficients to model the gain and cross components respectively. The first and fourth columns are the amplitude beams of XX and YY respectively whilst the beams in the second and third columns are XY and YX correspondingly.	53
5.7	Radial profile of Fig. 5.6. (a) Using 5 strongest Zernike coefficients for the Jones components. (b) Using 10 strongest Zernike coefficients for the Jones components. (c) Using 20 strongest Zernike coefficients for the gain components and 10 strongest Zernike coefficients for the cross components.	54
5.8	Histogram plots showing the residual distribution. (a) Plots obtained from using 10 strongest Zernike coefficients for the Jones components. (b) Plots obtained from using 10 strongest Zernike coefficients for the Jones components. (c) Plots obtained from using 20 strongest Zernike coefficients for the gain components and 10 strongest Zernike coefficients for the cross components.	54
5.9	Spectral representation of the amplitude of MeerKAT primary beams for L band. The light-gray vertical dashes are the missing gaps due to high RFI whilst the thin dotted lines are the DCT plots used to correct the bad channels for the respective Jones terms [XX (top) and XY (down)].	56
5.10	Spectral representation of the phase of MeerKAT primary beams for L band. The thick dotted lines are the Zernike plots with missing frequency channels due to high RFI whilst the solid lines are the Sine and Cosine plots used to correct the bad channels for the phase terms of XX and XY.	56
5.11	Measured Stokes I , Q and U convolved with reconstructed MeerKAT beam models with corresponding error maps. 1 st row: These are maps convolved with Zernike beams with 20 highest coefficients. 2 nd row: These are maps convolved with Zernike beams with 5 highest coefficients. 3 rd row: These are maps convolved with Zernike beams with 10 highest coefficients. The 4 th and 5 th rows are the corresponding residual maps between the 1 st and 2 nd rows and between the 1 st and 3 rd rows.	57
5.12	The distribution of angular power plots displaying the errors due to perturbed Zernike fits in Stokes I map (left plots) and the intrinsic leakage in I (right plots) affect the 21 cm signal (solid circular spectrum plot).	58

6.1	“Layout of the planned SKA1-MID telescope showing the locations of the antennas in the core and in the three spiral arms” (Fig. 6.1 and the caption are obtained from [102]).	60
6.2	A geometrical dual reflector model of SKA1-mid oriented in the $xz-$ direction and generating highly contoured beam.	62
6.3	Representation of MSE for using the number of ZP at 450 MHz (blue), 990.5 MHz (orange) and 13.6 GHz (green). Panel (a) shows the gain term (XX) for each channel band whilst Panel (b) displays the cross term (XY).	64
6.4	Top Row: Simulated EM model of SKA1-mid beam (in amplitude form) with a diameter of 6° at 450 MHz in a normalised unit. Middle Row: The restored model of the first row, using Zernike fit. Last Row: The respective beam errors between the top two rows. Here, columns one and four are the amplitude beams of XX and YY respectively whilst the beams in the second and third columns are XY and YX correspondingly.	64
6.5	Top Row: Simulated EM model of SKA1-mid beam (in amplitude form) with a diameter of 6° at 990.5 MHz in a normalised unit. Middle Row: The restored model of the first row, using Zernike fit. Last Row: The corresponding beam errors between the 1 st two rows. Here, columns one and four are the amplitude beams of XX and YY respectively whilst the beams in the second and third columns are XY and YX correspondingly.	65
6.6	Top Row: Simulated EM model of SKA1-mid beam (in amplitude form) with a diameter of 4° at 13.6 GHz in a normalised unit. Middle Row: The restored model of the first row, using Zernike fit. Last Row: The corresponding beam errors between the 1 st and 2 nd rows. Here, columns one and four are the amplitude beams of XX and YY respectively whilst the beams in the second and third columns are XY and YX correspondingly.	66
6.7	Spectral profile showing the various energy levels of Zernike coefficients for Band 1 (350 – 1050 MHz). The Zernike indexes (in the legends) are the activated basis functions that are frequent in all the channels.	67
6.8	Spectral profile showing the various energy levels of Zernike coefficients for Band 2 (950 – 1760 MHz). The Zernike indexes (in the legends) are the activated basis functions that are frequent in all the channels.	67

6.9	Spectral profile showing the various energy levels of Zernike coefficients for Band 5a (4.6 – 8.4 GHz). The Zernike indexes (in the legends) are the activated basis functions that are frequent in all the channels.	67
6.10	Spectral profile showing the various energy levels of Zernike coefficients for Band 5b (8.4 – 13.6 GHz). The Zernike indexes (in the legends) are the activated basis functions that are frequent in all the channels.	67
6.11	Perturbed beams for Band 1 at 450 MHz. The data part (row 1) represents the original EM beams and the second row shows the corrupted EM beams due to systematic phase errors. The last row reports the differences between the respective beams in the top beams. Note, the first and fourth columns are the amplitude beams of XX and YY respectively whilst the beams in the second and third columns are XY and YX correspondingly.	68
6.12	Perturbed beams for Band 2 at 990.5 MHz. The data part (row 1) represents the original EM beams and the second row shows the corrupted EM beams due to systematic phase errors. The last row reports the differences between the respective beams in the top beams. Note, the first and fourth columns are the amplitude beams of XX and YY respectively whilst the beams in the second and third columns are XY and YX correspondingly.	68
6.13	Perturbed beams for Band 5 at 13.6 GHz. The data part (row 1) represents the original EM beams and the second row shows the corrupted EM beams due to systematic phase errors. The last row reports the differences between the respective beams in the top beams. Note, the first and fourth columns are the amplitude beams of XX and YY respectively whilst the beams in the second and third columns are XY and YX correspondingly.	69
6.14	Representation of $IXR_{\mu\nu}$ (right panels) with the corresponding Stokes I beams (left panels) at 450 MHz, 990.5 MHz and 13.6 GHz. Stokes I is computed in Jones terms as $(j_{xx}j_{xx}^* + j_{xy}j_{xy}^* + j_{yx}j_{yx}^* + j_{yy}j_{yy}^*)/2$	70
6.15	Systematic errors of the measured maps in Stokes I, Q, U, due to feed displacement at 450 MHz.	72
6.16	Systematic errors of measured maps using Zernike model beams at 450 MHz.	73
6.17	Systematic errors of measured maps due to feed displacement at 990.5 MHz.	73

6.18	Systematic errors of measured maps using Zernike model beams at 990.5 MHz.	74
6.19	Systematic errors of measured maps due to feed displacement at 13.6 GHz.	75
6.20	Systematic errors of measured maps using Zernike model beams at 13.6 GHz.	76
6.21	Convolved full-sky maps at 13.6 GHz with respective error in Stokes I , Q and U	77
6.22	Comparing the distribution of angular power plots between corrected beam errors due to Zernike fits or feed displacement in Stokes I map (left plots) and intrinsic polarization leakage in I (right plots) and how these affect both the 21 cm and CO signal (solid circular spectrum plot). (a) For Band 1 at 450 MHz (b) For Band 2 at 990.5 MHz (c) For Band 5 at 13.6 GHz	78
A.1	Fully polarised distorted primary beams of KAT-7. (a) Due to gain and phase errors. (b) Due to dipole orientation errors.	83
A.2	1 GHz holography measured Mueller beams of VLA. (a) Antenna 5. (b) Antenna 6.	84
A.3	Systematic errors of full-sky maps produced by computing the relative error between the absolute of the convolved true sky maps and the corrupted sky maps due to gain and phase error beams.	85
A.4	Systematic differences of the full-sky polarisation maps produced by computing the relative error between the convolved sky using VLA PBs in Fig. A.2.	86
A.5	Measured Stokes I , Q and U for holography measured beams of JVLA with corresponding errors terms.	87

List of Tables

3.1	Measured Spectral Indices at Different Frequency Bands	25
4.1	Error introduced in the power spectrum estimation	45
B.1	Relationship between single and double index schemes to third order.	88

Chapter 1

Introduction

Overview

This chapter introduces us to the general background of the research by briefly discussing the origin of the 21 cm radio line and then moves on to discuss the significance of intensity mapping experiments. The research problems, key objectives, justification and the entire structure of the thesis are also outlined.

1.1 The 21 cm Radio Emission Line

Despite the fact that space is very empty and there is a great distance between the stars in the Milky Way, the gap between these stars consists of dust and a very diffuse medium of gas. Astronomers refer to this matter and the radiation in space as the *interstellar medium* (ISM¹). The interstellar gas can be found in molecular (mainly H₂), ionic (HII) or atomic (HI) form and it is composed of Hydrogen ($\approx 70\%$) followed by Helium ($\approx 28\%$) and the rest being heavy elements (Oxygen, Carbon and Nitrogen). The molecular and atomic Hydrogen gases are located in the colder dense regions of the ISM at ($T \sim 10 - 30$)K and ($T \sim 50 - 100$)K respectively whilst, the ionic gas is in the warmer ($T \sim 10^3 - 10^4$)K more dilute regions [63].

Nevertheless, a large portion of the hydrogen gas (mostly in atomic form) in the ISM is in the least energy state [62]. Usually, both the proton and electron of a Hydrogen atom spin in the same state but, it happens very occasionally that (in every 11 million years), the proton and the electron within the hydrogen atom will realign themselves slightly (that is, change the direction of the spin

¹<http://www-ssg.sr.unh.edu/ism/what1.html>

spontaneously) as shown in Fig. 1.1, making the electrons to flip a little bit closer to the proton in a very specific way. The fact that this is specific means that the frequency at which the EM radiation is given out is always the same, that is, the frequency is approximately 1420.406 MHz, and therefore, using large radio telescopes, radio astronomers can observe the 21 cm line (at 1420.406 MHz) even in very distant galaxies. This 21 cm radio emission line was first proposed in the early 1940s by van de Hulst and is very famous in radio astronomy because it is the most powerful way of observing HI and making maps from it. Most often, when we observe the emission line, the distribution of this line is Doppler shifted. This is because, a spiral galaxy rotates in such a way that, if it is marginally edge-on to our line of sight, a portion of the HI regions move away from us whilst others move towards us. This Doppler effect broadens the 21 cm line into a double peak. It redshifts the radiation from the regions that move away from us and blueshifts the vice versa. Therefore, the faster the rotation of the galaxy, the greater the line broadening. It redshifts the radiation from the regions that move away from us and blueshifts the vice versa. Therefore, the faster the rotation of the galaxy, the greater the line broadening. Many academic works [30, 124, 123] give an in-depth explanation of this section.

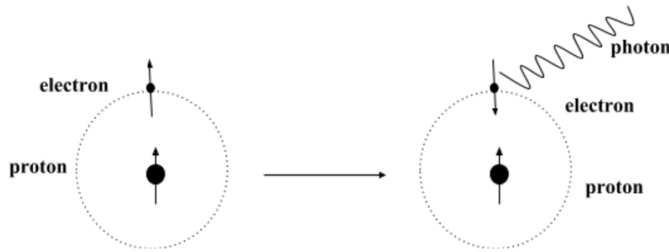


Figure 1.1: When the electron of a neutral hydrogen atom flips its spin, energy is released at a wavelength of 21 cm. This figure is obtained from [38, pg. 113].

The next section discusses how intensity mapping (IM) experiment is used to measure the distribution of the sky.

1.2 HI Intensity Mapping

The motivation to study cosmology in this present-day is to understand the massive size of the Universe, understand how the Universe expands and the distribution of everything. In order to do this, an observational time is needed to really map out the large volume of data. Over the past two decades, the

galaxy redshift surveys such as 2dF², 6dF³, WiggleZ⁴, BOSS⁵, and SDSS⁶ use the optical spectroscopy to specifically observe millions of individual galaxies, determine each redshift and use these to estimate the energy distribution for each [86, 98, 97]. This approach really consumes a lot of time due to the map out of individual galaxies and also, it is very difficult to resolve faint sources. The total optical surveys used to localize the Universe in this way is approximately 1% [86].

Meanwhile, recent researches [20, 26, 100, 129, 128] on IM have shown that, this alternative approach does not resolve all the structures in the Universe but can actually provide us with a very good idea of how things are distributed as displayed in Fig. 5.9b. Here, the figure shows the variations in the simulated HI brightness temperature, where red indicates over-density and blue under-density, making it possible to infer from this map. From a cosmological point of view, that is sufficient enough because we can still see a lot of the features in Fig. 5.9b map even though it's horribly pixelated as compared to Fig. 5.9a.

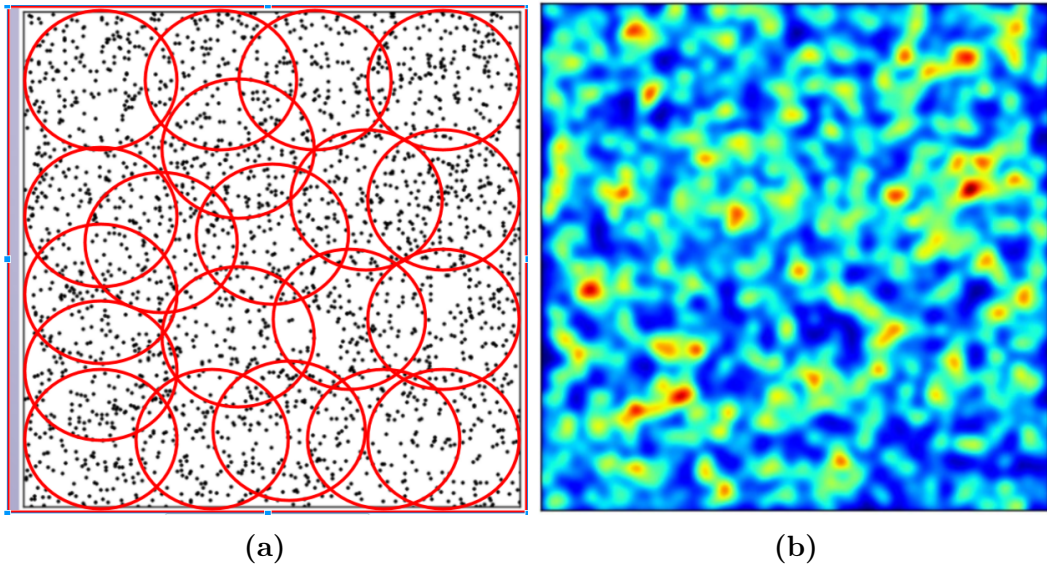


Figure 1.2: Simulated variations in the 21 cm emission brightness temperature. The red rings in (a) show how to perform IM experiment by observing multiple patches in the sky with the radio telescope in order to measure the 21 cm emission to produce (b). Note that this figure is very similar to the one discussed in [86].

In terms of the observing strategy, a radio telescope (usually a big dish) is used to point and scan over the sky to measure the 21 cm spectral line. With this complementary approach, we can effectively map a large volume of the sky,

²<http://www.2dfgrs.net/>

³<http://www-wfau.roe.ac.uk/6dFGS/>

⁴<http://wigglez.swin.edu.au/site/>

⁵<http://www.sdss3.org/surveys/boss.php>

⁶<http://www.sdss.org/>

since every frequency channel in the telescope will produce a different redshift of the HI. Note that, these big data obtained from the IM method can't really be achieved with any other method within the same period of time. These maps typically have a low spatial resolution, making it quite difficult to identify any single object as seen in Fig. 5.9b. Nevertheless, the maps do have high redshift resolution due to the signal to noise in the instrument channels. Therefore, HI IM is the technique of integrating the spectral line flux over the whole HI mass function without selecting individual neutral objects.

Section 1.3 briefly discusses the importance of IM observational techniques and some of the current radio instruments purposely designed to perform this kind of experiment.

1.3 Significance of Intensity Mapping Techniques

The IM technique has the advantage of not resolving sources but instead measures diffuse sources that can be used to generate tomographic maps of the Universe for many redshifts within the interval $0 < z < 6$ which is basically what the Square Kilometre Array (SKA) Phase I [44] is planning to do. In addition, the data produced from this technique contains spatial information that may be useful to measure Baryon Acoustic Oscillations (BAOs) [26] which is one of the major incentive explored by the cosmologists and has led to the establishment of this method. Measuring the BAOs for different redshifts would make us understand the expansion of the Universe. Furthermore, with the observational data from several lines, we will also be able to cross-correlate the lines which can be used to remove the foreground from 21 cm observations. Finally, the technique allows smaller and cheaper telescopes without long baselines such as HIRAX⁷, to be used in such experiments, hence increasing the science output in cosmology.

Presently, several IM experiments are in operation, such as the GBT⁸ (“Green Bank Telescope”), CHIME⁹ (“Canadian Hydrogen Intensity Mapping Experiment”), Tianlai¹⁰ and FAST¹¹ (“Five hundred metre Aperture Spherical Telescope”). Among these instruments for IM experiments, the GBT produced the first HI signal at $z \sim 0.8$, using the cross-correlation of the redshift survey by WiggleZ [27]. Moreover, the capabilities of upcoming instruments such as “dense aperture arrays for the SKA” [37] and HIRAX make it only more promising, due to the fact that, the technique is relatively “cheaper” compared to the

⁷<https://www.acru.ukzn.ac.za/~hirax/>

⁸<https://science.nrao.edu/facilities/gbt>

⁹<https://chime-experiment.ca/>

¹⁰<http://tianlai.bao.ac.cn/>

¹¹<http://fast.bao.ac.cn/en/>

usual galaxy surveys described in the first paragraph of Section 1.1. Furthermore, these new instruments will provide a broader range of frequencies and a very massive survey area in order to produce HI intensity maps. Lastly, in IM, observations can be made at different redshifts either in single dish mode like BINGO [11] or array mode like CHIME [77].

1.4 Problem Identification

Radio telescopes are primarily used to intercept the signal coming from a radio source. During observation, the propagation effects and antenna feed electronics transform the measured signal. The direction-independent effects (DIEs) are described by the complex gains of each instrument as well as the receiver configuration. These effects are calibrated and corrected separately from imaging. However, the direction-dependent effects (DDEs) are much more complicated, since they are applied during imaging and therefore, are modified into a convolution of the measured components. This makes it very relevant to both calibrate the unknown DDE and then correct the known or measured one. The ionospheric structure and the primary beam response of a two-axis mount telescope are the common sources of DDEs. They result in telescope mis-pointings and antenna structure deformation caused by the gravitational loads acting on the dish and differential heating. These two time-varying terms go a long way to affect observations with the existing and upcoming instruments. For instance, the challenges put forward by ionospheric structure are particularly stern at very low frequencies and this can affect radio arrays like LOFAR¹² [122].

Currently, the existing technique [5, 49] used for IM requires a precise separation of the weak 21 cm line signal from the Galactic foreground continuum signal. This present approach is acceptable when there is no instrumental distortion and the foreground signal is assumed to be smooth. However, DDEs are very crucial in physical observations and in IM experiments, the primary beam, in particular, is a challenge, as it modulates the intensity of the source with respect to the sky position, which is exactly what is being measured by this technique in the first place. In the case of Karoo Array Telescope (KAT-7¹³), MeerKAT¹⁴ and construction telescopes, these will be affected by pointing errors and DD polarization leakages. Present DD methods [108] can not be used directly since distinct galaxies are not localized by this experiment. Hence, an improved method to resolve DDEs in a stochastic way has to be developed.

¹²<http://www.lofar.org/>

¹³<http://public.ska.ac.za/kat-7>

¹⁴<http://www.ska.ac.za/gallery/meerkat/>

1.5 Research Objective

The key focus of this project is to develop IM techniques for mapping out primary beams of a radio telescope and then, introducing realistic errors to perturb these modelled beams. We then attempt a correction and calibration of these distorted modelled beams and ultimately, use the final data for intensity mapping experiments. Thus, we use these modelled beams to simulate the complete-sky maps and then, determine the foregrounds that have corrupted the total intensity due to polarization leakage and errors in the primary beams which have not been accounted for. The study used Oxford’s Square Kilometre Array Radio-telescope ([OSKAR¹⁵](#)), a beamforming simulator, specifically developed to generate simulated data from large aperture arrays, such as those envisaged for the SKA Phase I, to simulate the KAT-7 notional beams. The next beams produced for this study are Zernike models reconstructed from MeerKAT holography measured beams. The last primary beams used in this research are obtained from the Generalized Reflector Antenna farm analysis Software Package ([GRASP¹⁶](#)) of electromagneTIC RAdiation ([TICRA](#)) software.

In addition, apart from studying the 21 cm line, there are other spectral lines such as CII fine-structure line [47, [107](#), [132](#)], Ly α line [[111](#), [113](#), [133](#)], and the rotational CO lines [[70](#), [82](#), [119](#)] that detect different physical mechanisms. Therefore, this work will use the SKA1-mid to look into CO IM for high redshift in conjunction with HI IM at low redshift. Details of this will be discussed in Chapter [6](#).

1.6 Delimitation

The study’s main scope is to calibrate two outcomes:

- (i) the effect of polarization leakage to the estimated HI and CO spectra, using realistic primary beams and
- (ii) the inaccuracies in the estimate of (i) due to the perturbations that have not been modelled in the primary beams.

1.7 Rationale and Motivation

Normally, when a portion of two signals leak into each other due to inadequacies in the mechanical and electrical designs of the antenna, it is referred to as the *polarization leakage*. With regard to Stokes parameters, this creates an

¹⁵<http://www.oerc.ox.ac.uk/~ska/oskar2/>

¹⁶<http://www.ticra.com/products/software/grasp>

undesired spread of the signal from the absolute intensity I to polarization QUV and vice-versa. This problem is very unique in IM experiments and since Faraday effect rotates the polarization QU , the polarized foregrounds are generally not uniform across frequency [8]. This challenge can go a long way to limit observations not only with the present working telescopes but even those under construction. The study is motivated by this and therefore, concentrates rather on the effects of the primary beam particularly, DD polarization leakage. The potential of IM has already been demonstrated [129, 26, 128, 72, 100] and the capabilities of upcoming telescopes as mentioned in Section 1.3 make it only more promising. However, considerable research into this technique is necessary since there are some sort of technical challenges in terms of data analysis and in particular measuring the primary beam response, which has to be overcome in order to make such an experiment work to its full potential.

1.8 Thesis Layout

The study is divided into seven different chapters as follows:

Chapter 1 briefly introduces the research topic by commencing with the general background of 21 cm emission line and continues by presenting the significance of IM experiment and clearly stating the research problem and objective. This chapter also justifies why the study is conducted and briefly explains how the simulations are done to produce the primary beams for various antenna types.

Chapter 2 discusses radio telescope antennas, where we clearly look at the numerous designs, operations and performances of antennas. Radio array types and the concept of measurement equation are also reviewed in this chapter.

Foregrounds and rotation measure synthesis are discussed in Chapter 3. Here, the study mainly focused on synchrotron emission and concisely describe how we simulate the foreground and applied rotational measures.

Chapter 4 presents the first methodology employed in this research. In this chapter, we describe extensively the observational effects of primary beam perturbation of KAT-7, using the OSKAR software package. We then go ahead to determine the polarization leakage by introducing the convolution technique to simulate the foregrounds produced in Chapter 3. Here, KAT-7 is used as a conceptual example for the purposes of this study. The study moves on further to compare the energy profile of the simulated beams and the Jansky Very Large Array (JVLA¹⁷) holography measured beams.

Chapter 5 describes the second methodology of this study. In this chapter,

¹⁷<https://science.nrao.edu/facilities/vla>

we produce modelled beams by fitting Zernike polynomials on MeerKAT measured beams to compute the reconstructed beams with fewer coefficients. We then estimate the effect on IM by measuring the foregrounds in Chapter 3 with the Zernike-beams.

The third methodology in this work is presented in Chapter 6, where we generate GRASP simulated EM beams of SKA1-mid for bands 1, 2 and 5. These EM beams of various bands are reconstructed with the Zernike model, using the strongest Zernike coefficients (that is, selected number of coefficients) and in addition, we try to perturb these GRASP beams by introducing errors in the feed coordinates to displace the feed from its principal focus. Finally, we perform IM experiments by simulating the foregrounds in Chapter 3 with all these modelled beams to estimate not only HI flux at lower bands but also CO signals too at higher bands.

Conclusions and recommendations are discussed in Chapter 7.

Chapter 2

Radio Antennas and Interferometry

Overview

Chapter Two introduces us to the general antenna parameters that are significant to describing the operation and performance of an antenna. A further discussion is made on how to mathematically derive the Stokes parameters from wave propagation. Types of radio arrays are also discussed in this section. Finally, a brief description of radio interferometry is given.

2.1 Introduction

The fundamental laws that govern the complete EM phenomena can be explained by the famous Maxwell's equations as follows:

- The Gauss' law for electric field is defined as:

$$\oint \vec{\xi} \cdot d\vec{s} = \frac{q}{\epsilon_0} \quad (2.1)$$

where the charge q is circumscribed within a closed region and ϵ_0 is electric constant (also known as electric permittivity of free space). This relation means that whenever there is a charge q , there exist an electric field $\vec{\xi}$ and of course, anytime there is $\vec{\xi}$, there exist q .

- The Gauss' law for magnetic field is defined as:

$$\oint \vec{B} \cdot d\vec{s} = 0 \quad (2.2)$$

This equation shows that a magnetic field \vec{B} is always defined in a closed line. Here, \vec{B} has no static point and no termination.

- Equation 2.3 is Faraday's law of EM induction:

$$V_k = -\frac{d\phi_B}{dt} \quad (2.3)$$

Here, the rate of change of magnetic flux is equal to the voltage induced V_k and therefore, this induced potential difference can be expressed as $\oint \vec{\xi} \cdot d\vec{r} = -\frac{d}{dt} \vec{B} \cdot A$ with A being the cross section area. Note that whenever there is a change in \vec{B} , we obtain $\vec{\xi}$.

- The fourth equation is Ampere-Maxwell's law and this is given as:

$$\oint \vec{B} \cdot d\vec{l} = \mu_0 i_c + \mu_0 \epsilon_0 \frac{d\phi_\xi}{dt} \quad (2.4)$$

where ϕ_ξ is the change in electric flux, $d\vec{l}$ is the direction of the current, i_c is the conduction current and the magnetic constant (also known as magnetic permeability of free space) is denoted μ_0 . Equation 2.4 shows that, a change in an electric field creates a magnetic field.

The mathematical models in these four equations give a complete characterisation of how the fields $\vec{\xi}$ and \vec{B} are produced and altered by each other. The term $\oint \vec{B} \cdot d\vec{l} = \mu_0 \epsilon_0 \frac{d\phi_\xi}{dt}$ in Equation 2.4 depicts the existence of wave such that, $1/\sqrt{\mu_0 \epsilon_0}$ gives the speed of the wave. Therefore, Equations 2.3 and 2.4 are responsible for the prediction of EM wave due to the spatial and time variations of the fields. A comprehensive understanding of Maxwell's equations can be obtained from [51, 40].

In radio astronomy, we can intercept the EM wave with a *radio telescope*. The instrument operates in a reception mode such that the electric current induced on the input terminals, converts into a radio frequency (RF) signal and we can observe the signal at different ranges, called *bands*. Next, we present on the parameters of an antenna.

2.2 Antenna Parameters

The antennas we use in radio astronomy are devices that receive radio waves from the free space and convert them into electrical signals. Numerous designs

of an antenna make it necessary to define how the instrument operates. This requires a clear understanding of the parameters of the antenna and therefore, in this section, we present a review of some fundamental parameters of an antenna discussed by [10].

2.2.1 Antenna Field Regions

The antenna field zones illustrate how antenna radiates with respect to its position. There are basically three main classes of field zones as depicted in Fig. 2.1 and briefly discussed below:

- *Reactive near-field*: It is the immediate region surrounding the antenna where electric and magnetic fields are mostly not in phase. The energy in this region usually turns back to the antenna in a regenerative manner (thus, there is back and forth oscillation of energy) hence, storing the energy in this region [6]. The radius of this zone is computed as $r_1 < 0.62 \left(\frac{D^3}{\lambda} \right)^{1/2}$, where r is the separation from the antenna surface, D is the size of the antenna and λ is the wavelength in metres. The frequency of the EM wave is related to the wavelength such that, $\lambda = \frac{c}{\nu}$ where, $c \approx 3.0 \times 10^8$ m/s is the speed of light and ν is the frequency in Hz.
- *Radiating near-field* (also known as the *Fresnel* region): It is the next region after the reactive near-field where the field distribution begins to have some regular pattern as displayed in Fig. 2.1. Thus, part of the energy obtained in this region converts into radiation. This is because in this zone, the EM fields are not directly in or out of phase hence, making the field strength to become less reactive as compared to the immediate field zone. The radius of this zone is determined as $r_2 < 0.62 D^2 / \lambda$.
- *Far-field* (also known as the *Fraunhofer* region): This region exists at a distance $r_3 > 2 D^2 / \lambda$. The reactive fields are no longer present and only the radiation fields exist. Here, the EM fields are directly orthogonal with constant amplitude. Furthermore, the general radiation pattern in this region remains the same regardless of the distance from the antenna.

Therefore, as the space from the antenna changes from the near to the far fields, the radiation pattern of an antenna also varies in shape in terms of amplitude and phase. In Fig. 2.1, the radiation pattern is almost uniformly distributed in the reactive near-field region and gradually creates smooth lobes at the radiating near-field and eventually, gets fully formed at the far-field with minor and major lobes. In radio astronomy, the antenna of a radio telescope operates in the far-field of the feed system to produce the desired illumination of the antenna.

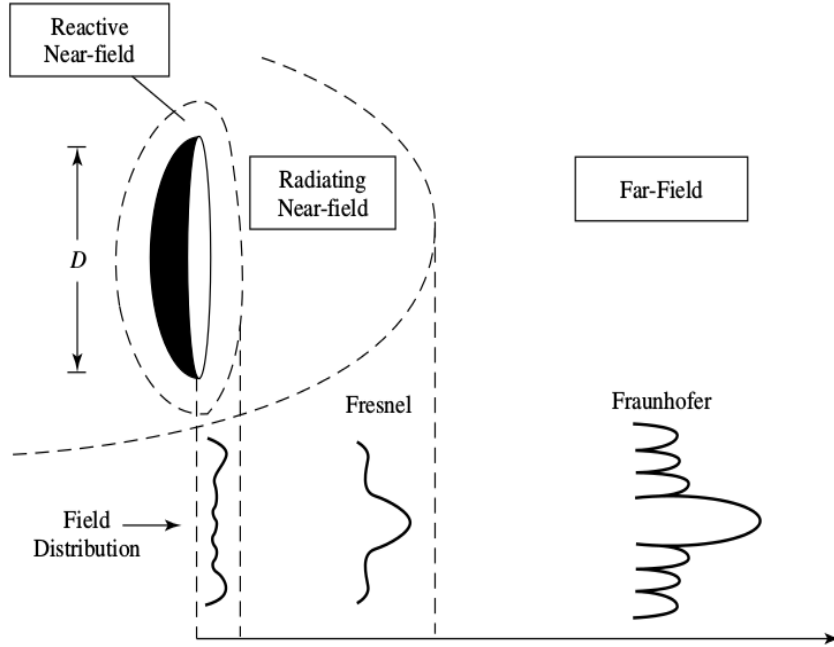


Figure 2.1: An illustration of the various field distributions at each field zone.
Source: This figure is reproduced from [10, pg. 35] but originally produced by [90].

2.2.2 Radiation Patterns

It is a visual description of the radiation properties of the antenna. The pattern of the antenna is mostly in 3D and measured in steradians, but can also be projected in a linear scale as shown in Fig. 2.2. There are actually two main types of this pattern, namely:

- *Field pattern*:- This is the amplitude of the electric field radiated by the antenna in the space coordinate. From the two plots in Fig. 2.2, we have the maximum radiation in the vertical region and the field region can be calculated by taking the Half Power Beam Width (HPBW) of the radiation pattern. The HPBW is the angular distance at the point of 0.707 of the maximum radiation.
- *Power pattern*:- It is the square of the magnitude of the electric field the antenna radiates with respect to the space position. Here, the HPBW is computed at the point of 0.5 of the maximum power radiated. The angular distance of this half power point of the maximum radiation is known as HPBW.

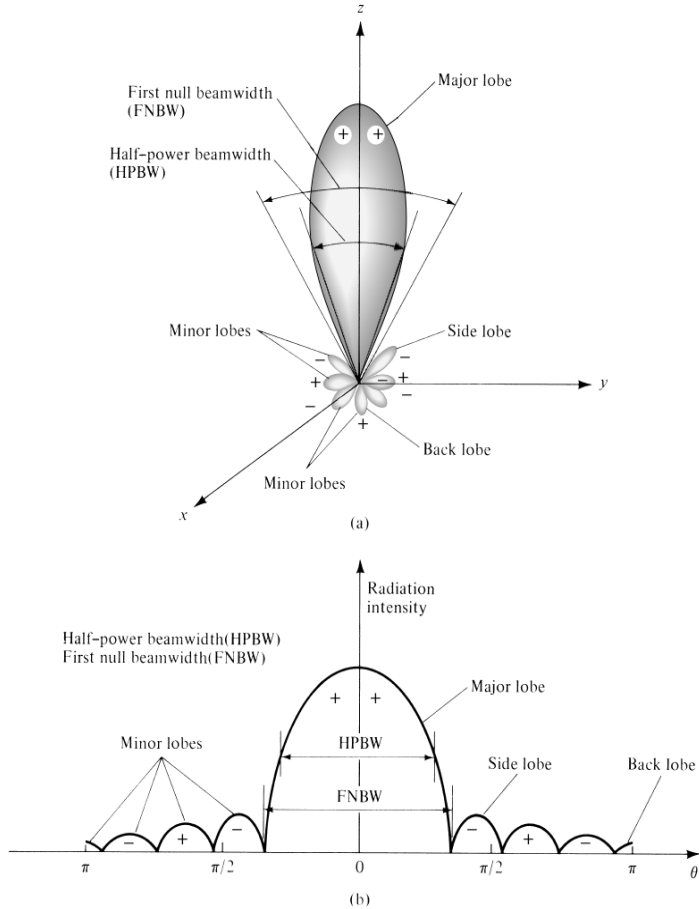


Figure 2.2: (a) Antenna radiation pattern showing the various lobes in angular scales. (b) Linear projection of the pattern in (a). *Source:* Obtained from [10, pg. 30]

The portion of the radiation in which the power is accommodated by the antenna is known as *lobes*. We can observe from Fig. 2.2 that in one direction there is maximum power radiation and other directions there are less power radiation. The maximum power radiated in whatever direction is giving us a big lobe of radiation known as the *major lobe*. The lobes other than the major lobe are termed *minor lobes*. These minor lobes are partitioned into *side lobes* and *back lobe*. In addition, there are certain directions where radiation drops to zero. The adjacent directions to the major lobe where the radiation drops to zero are known as *null* directions. The null direction close to the major lobe is called the *first null*.

Depending on the shape of the radiation pattern in free space, we have different kinds, namely:

- *Isotropic radiation pattern*:- As the name suggests, between halves there is equal power radiation in all directions. This type of pattern is practically not realistic but the ideal case.
- *Directional radiation pattern*:- Fig. 2.2 is a typical example of directional

antennas such as Cassegrain and Offset Gregorian dishes. Here, we have the maximum radiation in one direction and zero or less radiation in the other directions.

- *Omni-directional radiation pattern*:- It is when the radiation is not in one direction but in equal orthogonal planes.

2.2.3 Radiation Intensity

This is the power flow per unit solid angle. It can be expressed as;

$$\Phi_{\text{rad}} = r^2 \Psi_{\text{rad}} \quad (2.5)$$

where, Φ_{rad} is the radiation intensity in Wsr^{-1} , Ψ_{rad} is the intensity of the electric-field in Wm^{-2} and r is the radius of the electric field component.

2.2.4 Gain

The gain of an antenna is the maximum intensity in one direction to the intensity provided by the antenna if the power is radiated uniformly. Mathematically, we can define this as;

$$G = 4\pi \frac{\Phi_{\text{rad}}(\theta, \phi)}{P_{\text{in}}} \text{ (dimensionless)} \quad (2.6)$$

where, $\Phi_{\text{rad}}(\theta, \phi)$ is the radiation intensity in the direction (θ, ϕ) and P_{in} is the overall accepted power.

2.3 EM Wave Polarization

Consider a target source emits an EM wave such that this wave is said to be unpolarized, that is, the electric field of this wave oscillates in every possible position in a plane that is perpendicular to the direction of propagation in the positive z as displayed in Fig. 2.3. From Fig. 2.3, if the unpolarized wave passes through the polarizing element M1, then M1 will discard all the horizontal components and choose the components in its preferred direction. As a result, the wave that comes out is going to be polarized in the same phase as M1.

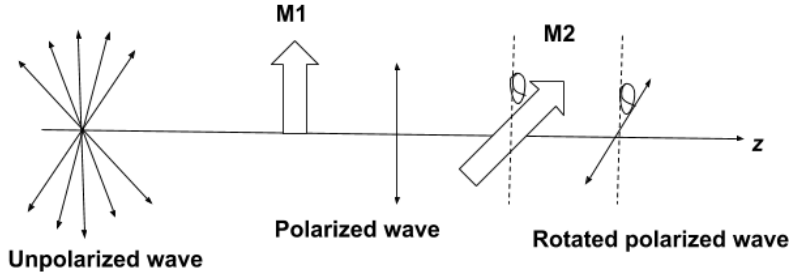


Figure 2.3: The diagram shows how a polarizing element can polarize an unpolarized wave and also rotate the direction of incoming polarized wave.

Note that, a polarizing element does not only polarize wave but can also rotate the wave. For instance, if the polarized wave in Fig. 2.3 goes through the polarizer M2 at an angle θ with respect to the vertical, then M2 ignores all the wave components that are not along the preferred direction and accepts those along angle θ . Therefore, the output wave will still be polarized but rotated at an angle θ . If $\theta = 90^\circ$, then M2 will have horizontal direction that it prefers by getting rid of all the vertical parts of the incoming wave. Hence, if M1 is vertical and M2 is horizontal, there would not be any wave that goes through M2.

In Fig. 2.3, if we let the electric field $\vec{\xi}$, to be polarized vertically and propagating in the direction z , then the magnetic field \vec{B} is polarized horizontally (perpendicularly). Here, $\vec{\xi}$ and \vec{B} conform with the wave equation such that the $\vec{\xi}$ units in the (x, y) coordinates of a plane-wave can be defined as Equation 2.7:

$$\xi_x(z, t) = \xi_1 \cos\{\omega t - \beta z + \varphi_x\} \quad (2.7a)$$

$$\xi_y(z, t) = \xi_2 \cos\{\omega t - \beta z + \varphi_y\} \quad (2.7b)$$

where, the constant terms ξ_1 and ξ_2 characterise the maximum amplitude of (x, y) components respectively, the radial frequency is $\omega = 2\pi\nu$, the ellipticity measure is expressed as $\beta = 2\pi/\lambda$ and φ_x, φ_y are phases of ξ_x and ξ_y respectively. Equations 2.7a and 2.7b represent the two linearly polarized waves in the horizontal and vertical orientations respectively. Rewriting Equation 2.7 vectorially, we get Equation 2.8:

$$\xi(z, t) = \hat{x}\xi_x(z, t) + \hat{y}\xi_y(z, t) \quad (2.8a)$$

$$= \hat{x}\xi_1 \cos\{\omega t - \beta z + \varphi_x\} + \hat{y}\xi_2 \cos\{\omega t - \beta z + \varphi_y\} \quad (2.8b)$$

where, \hat{x}, \hat{y} = unit vectors in x and y directions. Therefore, at $z = 0$, Equation 2.8 becomes:

$$\boldsymbol{\xi}(t) = \hat{\mathbf{x}}\xi_1 \cos\{\omega t + \varphi_x\} + \hat{\mathbf{y}}\xi_2 \cos\{\omega t + \varphi_y\} \quad (2.9)$$

As clearly presented in [66], by eliminating the time t in Equation 2.9, we obtain the most general expression of an ellipse as given in Equation 2.10:

$$a\xi_x^2 - b\xi_x\xi_y + c\xi_y^2 = 1 \quad (2.10)$$

where, $a = 1/\xi_1^2 \sin^2(\varphi)$, $b = 2 \cos(\varphi)/\xi_1\xi_2 \sin^2(\varphi)$, $c = 1/\xi_2^2 \sin^2(\varphi)$ and $\varphi = \varphi_y - \varphi_x$.

Equation 2.10 shows that at any specific time t , the locus of points characterised by the propagation of ξ_x and ξ_y will trace out this curve. In Equation 2.10, the product term $\xi_x\xi_y$ actually shows a rotated ellipse. Obviously, if $\xi_1 = 0$, Equation 2.8 becomes linearly polarized in the vertical orientation, and vice versa if $\xi_2 = 0$. When $\varphi = +90$ and $\xi_1 = \xi_2$, a *left circularly polarized* wave is produced and when $\varphi = -90$, it is known to be *right circularly polarized*.

2.3.1 Derivation of the Stokes Polarization Parameters

Section 2.3 dealt with fully polarized waves where, ξ_1, ξ_2 and φ are considered constants. A monochromatic (i.e. single-frequency) radiation is of that form. However, generally, in radio observation, the emission from astronomical objects expands across a multi-frequency range and the bandwidth $\Delta\nu$, consists of incoherently polarized waves due to the superposition of independent waves of different polarizations. In this section, we present a review of the formulation of Stokes parameters discussed by [66]. If we assume two plane waves are orthogonal and let $z = 0$ in Equation 2.7, we get Equation 2.11:

$$\xi_x(t) = \xi_1(t) \cos\{\omega t + \varphi_x(t)\} \quad (2.11a)$$

$$\xi_y(t) = \xi_2(t) \cos\{\omega t + \varphi_y(t)\} \quad (2.11b)$$

The time variations of $\xi_1(t), \xi_2(t), \varphi_x(t)$ and $\varphi_y(t)$ are very slow compared to that of the mean frequency, ν ($\omega = 2\pi\nu$) which is of the order of the bandwidth $\Delta\nu$. Eliminating ωt term explicitly between Equations 2.11a and 2.11b we get a similar expression in Equation 2.10:

$$\frac{\xi_x^2(t)}{\xi_1^2(t)} - 2\frac{\xi_x(t)\xi_y(t)}{\xi_1(t)\xi_2(t)} \cos \varphi(t) + \frac{\xi_y^2(t)}{\xi_2^2(t)} = \sin^2 \varphi(t) \quad (2.12)$$

where, $\varphi(t) = \varphi_y(t) - \varphi_x(t)$. Equation 2.12 reduces into Equation 2.10 when monochromatic radiation is considered, making ξ_x and ξ_y implicitly time dependent.

In order to measure the intensity of a radio wave, we compute the average per the time of observation and assume the time taken to be infinite because it takes a lot of time to oscillate per cycle. The time average for Equation 2.12 is therefore represented as:

$$\frac{\langle \xi_x^2(t) \rangle}{\xi_1^2} - 2 \frac{\langle \xi_x(t) \xi_y(t) \rangle}{\xi_1 \xi_2} \cos \varphi + \frac{\langle \xi_y^2(t) \rangle}{\xi_2^2} = \sin^2 \varphi \quad (2.13)$$

where the symbol $\langle \rangle$ denotes the time average and

$$\langle \xi_i(t) \xi_j(t) \rangle = \lim_{T \rightarrow \infty} \int_0^T \xi_i(t) \xi_j(t) dt, \quad i, j = x, y \quad (2.14)$$

Multiply Equation 2.13 by $4\xi_1^2 \xi_2^2$ and then use Equation 2.14 to compute the average terms in Equation 2.13 to get:

$$2\xi_1^2 \xi_2^2 - (2\xi_1 \xi_2 \cos \varphi)^2 + 2\xi_1^2 \xi_2^2 = (2\xi_1 \xi_2 \sin \varphi)^2 \quad (2.15)$$

Representing Equation 2.15 in perfect square form, we add and subtract $\xi_1^4 + \xi_2^4$ to get:

$$(\xi_1^2 + \xi_2^2)^2 - (2\xi_1 \xi_2 \cos \varphi)^2 - (\xi_1^2 - \xi_2^2)^2 = (2\xi_1 \xi_2 \sin \varphi)^2 \quad (2.16)$$

We can deduce the intensities from Equation 2.16:

$$P_I = \xi_1^2 + \xi_2^2 \quad (2.17a)$$

$$P_Q = \xi_1^2 - \xi_2^2 \quad (2.17b)$$

$$P_U = 2\xi_1 \xi_2 \cos \varphi \quad (2.17c)$$

$$P_V = 2\xi_1 \xi_2 \sin \varphi \quad (2.17d)$$

I, Q, U and V in Equation 2.17 are the real quantities of Stokes parameters with I being the total intensity. The parameter Q characterises the linear horizontal or vertical polarization; that of U characterises the amount of linear $\pm 45^\circ$ polarization and V represents circular polarization. We can calculate the degree of polarization P_{deg} , for a given state of polarization:

$$P_{\text{deg}} = \frac{I_{\text{pol}}}{I_{\text{tot}}} = \frac{(Q^2 + U^2 + V^2)^{1/2}}{I}, \quad 0 \leq P_{\text{deg}} \leq 1 \quad (2.18)$$

However, ignoring the time average approach and expressing Equations 2.11a

and 2.11b in terms of complex amplitudes to obtain Equation 4.27:

$$\xi_x(t) = \xi_x \exp\{i\omega t\} \quad (2.19a)$$

$$\xi_y(t) = \xi_y \exp\{i\omega t\} \quad (2.19b)$$

where $\xi_x = \xi_1 \exp\{i\varphi_x\}$ and $\xi_y = \xi_2 \exp\{i\varphi_y\}$ are the complex amplitudes. The Stokes polarization parameters from these complex amplitudes are:

$$P_I = \xi_x \xi_x^* + \xi_y \xi_y^* \quad (2.20a)$$

$$P_Q = \xi_x \xi_x^* - \xi_y \xi_y^* \quad (2.20b)$$

$$P_U = \xi_x \xi_y^* + \xi_y \xi_x^* \quad (2.20c)$$

$$P_V = i(\xi_x \xi_y^* - \xi_y \xi_x^*) \quad (2.20d)$$

These Stokes terms can be used to describe the full polarization state of a signal, for instance, the foregrounds are mostly presented in Stokes parameters. Chapter 4 gives a further detail on how to formulate the Stokes parameters in terms of the column matrix to obtain not only measurable intensities but also observables too.

2.4 Antenna Arrays

Array antenna (also known as interferometer) is the connection of at least two spatially distributed antennas used to measure or direct the radiation intensity of a source towards a desired angular sector in order to have an improved performance over a single antenna. One unique property of an interferometer is that the beam pattern can be changed when we electronically steer or scan the antenna elements towards some other direction by changing their relative amplitudes and phases. This operation can not be done with a single dish since the beam pattern remains constant.

2.4.1 Mathematical Formulation of Antenna Array

Consider N antenna elements with corresponding radiated electric field $\bar{E}_k(\theta, \phi) |_{k=1,2,3,\dots,N}$ such that the angle of elevation and azimuth of these elements are defined within the range of $-90^\circ \leq \theta \leq 90^\circ$ and $-180^\circ \leq \phi \leq 180^\circ$ respectively. Then, the overall electric field $\bar{E}(\theta, \phi)$ can be expressed as:

$$\bar{E}(\theta, \phi) = \sum_{n=1}^N w_n \bar{E}_n(\theta, \phi) \exp\{i\xi\psi_n(\theta, \phi)\} \quad (2.21)$$

where, the element location is $\psi_n = x_n \sin \theta \cos \phi + y_n \sin \theta \sin \phi + z_n \cos \theta$, $\xi = \frac{2\pi}{\lambda}$ is the wavenumber, $w_n|_{n=1,2,3,\dots,N}$ are the elements complex weights. If the antenna elements are identical, Equation 2.21 becomes;

$$\bar{E}(\theta, \phi) = \bar{E}_1(\theta, \phi) \sum_{n=1}^N w_n \exp\{i\xi\psi_n(\theta, \phi)\} \quad (2.22)$$

where $\bar{E}_1(\theta, \phi)$ is the element factor and $\sum_{n=1}^N w_n \exp\{i\xi\psi_n(\theta, \phi)\}$ is the array factor (AF). Equation 2.22 characterises the *array pattern multiplication*. Assuming we place N antenna elements uniformly linear on a particular axis with uniform spacing $n\Delta|_{n=0,1,2,3,\dots,N-1}$, then:

$$AF = \sum_{n=0}^{N-1} w_n \exp\{i\xi n\Delta \cos \theta\} \quad (2.23)$$

where $w_n = \exp\{-i\xi n\Delta \cos \theta_0\}$. Hence, substituting this into Equation 2.23, we get:

$$AF = \sum_{n=0}^{N-1} (\exp\{i\gamma\})^n, \quad \gamma = \xi\Delta(\cos \theta - \cos \theta_0) \quad (2.24)$$

From the geometrical progression theory, we can recall that:

$$\sum_{n=0}^{\infty} \alpha^n = \frac{1}{1-\alpha}, \alpha \neq 1 \text{ and } \sum_{n=0}^{N-1} \alpha^n = \frac{1-\alpha^N}{1-\alpha}, \alpha \neq 1$$

. Applying these two theories to Equation 2.24, we obtain Equation 2.25:

$$AF = \frac{1 - \exp\{iN\gamma\}}{1 - \exp\{i\gamma\}} \quad (2.25a)$$

$$= \frac{\exp\{iN\gamma/2\} \exp\{iN\gamma/2\} - \exp\{-iN\gamma/2\}}{\exp\{i\gamma/2\} \exp\{i\gamma/2\} - \exp\{-i\gamma/2\}} \quad (2.25b)$$

$$= \exp\{i(N-1)\gamma/2\} \frac{\sin(N\gamma/2)}{\sin(\gamma/2)} \quad (2.25c)$$

Since $\sin(Nx)/\sin(x)$ behaves like $N \operatorname{sinc}(x)$, ignoring the phase factor produces Equation 2.26:

$$AF = N \operatorname{sinc} \gamma/2 \quad (2.26)$$

Therefore, the maximum value of Equation 2.26 occurs when $\gamma = 0$, making $AF = N$.

2.4.2 Beam-forming

The combination of multiple signals with different complex weights from different receiving antenna elements forms a new radiation pattern. This technique is known as *beam-forming* and can be done in analogue components such as LOFAR with high-band antennas (HBA) or after the signal is digitised, such as in the LOFAR stations. The algorithms used to generate the technique can be classified into *coherent*, *incoherent* and *multi-pixel beam-former* methods. The application of coherent beam-forming allows a narrow beam to be formed and, therefore provides a higher gain which is very useful, for example, during pulsar observation. Coherent beam-forming increases the sensitivity in narrow FoV. Unlike coherent beam-forming, incoherent beam-forming does not affect FoV but increases the overall sensitivity. This kind of algorithm is very useful when searching for rare events where the location of occurrence is not known. The application of a multi-pixel beam-former like the “Giant Metre wave Radio Telescope” (GMRT¹) integrates the sensitivity of the other two methods by using a “recorded base-band data” [95] where there is a direct receiving of raw voltage samples from the interferometer into an array of storage disks. The technique used for observing pulsars mostly in extended sources can be made more efficiently, using the multi-pixel beam-former approach as shown in [32].

2.4.3 Types of Radio Arrays

In this subsection, we discuss the main types of antenna receiving elements that can be used for radio interferometric observations. The advantages and disadvantages are also discussed.

2.4.3.1 Phased-Array Feeds (PAFs)

Generally, a single dish has one pixel and only records the total power captured within its primary beam at any given time. We can produce an image by pointing the single beam at different directions and then project the output on a sky grid. PAF is a feed design of an antenna dish that consists of elements at reflector focus. It is mainly made up of antennas, hardware for signal processing and amplifiers. This new technology in radio astronomy is the same as having several arrays pointing at different places simultaneously. Its feed horn is electrically large and collects nearly all focused signal energy. Imaging with an array of multi-beam antennas gives a good resolution and increase in FoV. This increase in FoV comes at a cost of each receiving element requiring its own isolated analogue front-end and digital back-end, making the feed more

¹<http://gmrt.ncra.tifr.res.in/>

expensive. This is a new technology undergoing development and currently, PAFs have a higher system temperature and more limited analogue bandwidth than a feed with single pixel. Even though calibration and how to handle the big data of these new instruments are some of the challenges, their design and ongoing state of development serve as a pathfinder for the SKA [135]. Some of the PAF-based arrays are the “Aperture Tile In Focus” (APERTIF²) [80] which is an upgrade on “Westerbork Synthesis Radio Telescope” (WSRT) and “Australian Square Kilometre Array Pathfinder” (ASKAP³) [57] as displayed in Fig. 2.4.



Figure 2.4: PAFs showing the wide gain in the FoV. The third image from the left is the installation of APERTIF on WSRT. The last image from the left displays the PAFs fixed on ASKAP. *Source:* Reproduced from [43].

2.4.3.2 Transiting Arrays

Unlike a dish that can track a particular point in the sky over many hours, a transiting array has elements with limited mobility and allows the sky to drift through the primary beam of the elements. Its feed has an effective primary beam which is large compared to that of a dish. As a source enters into the beam, it starts with a small apparent flux, then gradually increases until the source peaks at the zenith. It then decreases as it moves across the beam side lobes until it finally sets at the horizon. Some of the transiting arrays are “Precision Array for Probing the Epoch of Reionization” (PAPER) [84], “Long Wavelength Array” (LWA) [35], Medicina Northern Cross and the “Murchison Widefield Array” (MWA⁴) [73] as shown in Fig. 2.5. Note that some of the transit arrays such as CHIME, Tianlai, HIRAX, and UTMOST⁵ use collecting elements. There are obvious cost advantages to building an array with no moving parts. Such arrays have wide FoV and can have the individual elements placed close together. This allows for large-scale structure experiments, such as Epoch of Reionization (EoR) and BAO studies. The disadvantages compared to dishes create a new challenge for calibration and imaging. The individual

²<https://www.astron.nl/astronomy-group/apertif/apertif>

³<http://www.atnf.csiro.au/projects/askap/index.html>

⁴<http://www.mwatelescope.org/>

⁵<https://astronomy.swin.edu.au/research/utmost/>

elements are less sensitive compared to a dish, so more elements are needed, which requires larger correlator systems. In addition, as the sky transits, the apparent flux of sources changes, so the primary beam must be well known in order to get back to the intrinsic flux of the sky. Depending on the scale of the primary beam, a transiting array has a set amount of time per day in which a section of the sky can be observed. This means that a deep integration of a region of sky is not possible without observing it for many days.



Figure 2.5: Transiting Arrays:- PAPER (top-left), LWA (bottom-left), Medicina Northern Cross (top-right) and MWA (bottom-right).

2.4.3.3 Aperture Arrays

We can convert a transiting array into a digital dish to form an *aperture array*. This makes it possible to point the digital dish in many directions of the sky simultaneously. The idea with an aperture array is that by updating the beamforming weights, the beam of the aperture array can track a region of the sky. The aperture array takes advantages from both dishes and transiting arrays. The main cost is the analogue and digital electronics to build such an array. For this reason, aperture arrays are mainly used for low-frequency science, such as LOFAR as in Fig. 2.6 and the future SKA-LOW shown in Fig. 2.7, as the Dense Aperture Array (DAA) components are cheaper. With improved technology, the price of higher frequency components will make it possible to increase the observable frequency. A second issue with aperture arrays is that the primary beam changes, depending on pointing location and frequency. As the beam is a weighted sum of all the individual elements there is limited precision to the beam shape. There is a design difference of sparse and dense aperture

arrays. When the elements of the aperture array are placed closer than $\lambda/2$ observing wavelength the array is *dense*. The array is fully sampling the wave-front and there are no beam artefacts, such as *grating lobes* (a type of side lobe) which introduces significant structure into the beam. If the elements are further apart than $\lambda/2$ then these side lobes structures appear and limit the sensitivity and FoV. For a single observing frequency, designing an aperture array is simple as all the elements are spaced at $\lambda/2$. However, for wide-band arrays, if the elements are placed at $\lambda_i/2$ for a wavelength λ_i , then for any wavelength $< \lambda_i$ the array configuration under-samples that observing wavelength and introduces large grating lobes. Therefore, a balance between observing bandwidth, cost and dense versus sparse trade-off must be made during the array design.



Figure 2.6: Aperture Array:- LOFAR.



Figure 2.7: SKA-2 Dense Aperture Arrays precursor telescope.

A more detailed discussion on radio arrays can be seen in [42].

2.5 Power gained from Radio Sources

The receivers of a radio telescope are very sensitive to the orientation state of the incoming radiation. More generally, in radio astronomy, two receivers are attached to each receiving feedhorn, with a splitter feeding horizontally

polarized radiation to one receiver and vertically polarized radiation to the other. The sum of what is obtained in each polarization is known as the *total intensity*. In each polarization, the power P_w received per unit bandwidth from an element of solid angle of the sky is defined as Equation 2.27;

$$P_w = \frac{1}{2} A_e \iint_{\Omega} B_s(\theta, \phi) P_n(\theta, \phi) d\Omega \quad (2.27)$$

where A_e = effective aperture (collecting area) of antenna [m^{-2}],
 $B_s(\theta, \phi)$ = brightness distribution of radio emission across the sky [$\text{W m}^{-2} \text{Hz}^{-1} \text{sr}^{-1}$],
 $P_n(\theta, \phi)$ = normalised power (beam) pattern of the antenna,
 $d\Omega = \sin \theta d\theta d\phi$, element of solid angle [sr].

In radio astronomy, what we are mostly interested in is the integral of the brightness over a radio source say S . The notation S defined in Equation 2.28 is the *flux density*:

$$S = \iint_{\text{source}} B_s(\theta, \phi) d\Omega \quad (2.28)$$

Consider the radio source is observed with a radio telescope with the power pattern $P_n(\theta, \phi)$, then, the observed flux density is computed by the product of the integral of the brightness distribution and the antenna beam pattern:

$$S_0 = \iint_{\text{source}} B_s(\theta, \phi) P_n(\theta, \phi) d\Omega \quad (2.29)$$

In Equation 2.29, if we have a radio point source at the phase centre of the beam, then, $P_n(\theta, \phi) \simeq 1$ and $S \simeq S_0$, but if the source is extended with simple geometry, then simple analytic function will enable S_0 to be corrected and this is discussed in the [45] technical report. The SI unit of flux density is usually expressed in $\text{W m}^{-2} \text{Hz}^{-1}$. Nevertheless, the radio emission is not very strong because it is emitted from a distant radio source, and the unit is mostly expressed as Jansky [Jy] which is named after the radio astronomer Karl Jansky. Here, $1 \text{Jy} \equiv 10^{-26} \text{W m}^{-2} \text{Hz}^{-1}$.

2.6 Basic Concepts of Radio Interferometry

Radio Interferometry is the process of using at least two radio elements to observe astronomical sources. When we synthesize the signals from the array along with the electronics we term it the interferometer. For a single telescope, the angular resolution is approximated as $\theta_R \simeq \text{wavelength of the signal}(\lambda)/\text{dish diameter}(D)$. This means for a particular λ , if we are interested in a better resolution, then we need to build a telescope with a very large diameter. This is practically

tedious and very expensive. Meanwhile, for an interferometer, it modifies D to the longest baseline $|\vec{B}|$. This separation accesses the effective diameter of the array. So, it is more cost effective and realistic to build an interferometer than a very large single dish. Therefore, a real-time interferometer for a flat-sky (that is, narrow field of view) is a set of complex visibilities defined in 2D Fourier transform as presented in Equation 2.30 :

$$\Lambda_{ab}^{vis}(u, v) = \iint A_{ab}^{beam}(\gamma_1, \gamma_2) I_{ab}^{sky}(\gamma_1, \gamma_2) \exp[-2\pi j(u\gamma_1 + v\gamma_2)] d\gamma_1 d\gamma_2 \quad (2.30)$$

where;

- (u, v) denote the coordinates of a pair of antennas a, b in the uv -plane. These coordinates are related to the baseline per unit wavelength such that $(u, v, 0) \propto \vec{B}/\lambda$, u is the east-west line of \vec{B} , and v is the north-south line of \vec{B} . Note that since we assume the visibility sampling is measured on a plane, our field of view becomes narrow and therefore, we ignore the w -term such that $w = 0$.
- (γ_1, γ_2) are the direction cosine in the image plane and so, they are related to the source position $\hat{\zeta}$, in the sky such that $(\gamma_1, \gamma_2, 0) \propto \hat{\zeta}$. Here, γ_1 is the east-west orientation of $\hat{\zeta}$, and γ_2 is the north-south orientation of $\hat{\zeta}$.
- the primary beam of two elements is described in A_{ab}^{beam} .
- $I_{ab}^{sky}(\gamma_1, \gamma_2)$ is the distribution of sky brightness.

Equation 2.30 is famously known as *van Cittert-Zernike equation* [118, 117, 91].

In physical observation, the complex visibility $\Lambda_{ab}^{vis}(u, v)$ is not measured everywhere, but only finite in the uv domain. Let denote this sampling process as $S_{ab}(u, v)$ such that we record zeros if no data is captured. As a result, the true sky $I_{ab}^{sky}(\gamma_1, \gamma_2)$, cannot be recovered directly, instead, we obtain the dirty map $I_{ab}^{dirty}(\gamma_1, \gamma_2)$, as given in Equation 2.31:

$$I_{ab}^{dirty}(\gamma_1, \gamma_2) = A_{ab}^{beam}(\gamma_1, \gamma_2) I_{ab}^{sky}(\gamma_1, \gamma_2) \otimes B_{ab}(\gamma_1, \gamma_2) \quad (2.31)$$

$B_{ab}(\gamma_1, \gamma_2)$ in Equation 2.31 is the point-spread function (PSF) describing the uv distribution of baselines and can be expressed as Equation 2.32:

$$B_{ab}(\gamma_1, \gamma_2) = \iint S_{ab}(u, v) \exp[2\pi j(u\gamma_1 + v\gamma_2)] d\gamma_1 d\gamma_2 \quad (2.32)$$

Hence, we can obtain $I_{ab}^{dirty}(\gamma_1, \gamma_2)$ by applying the convolution theorem, using the operator \otimes . Once a dirty image is made, we can deconvolve it to produce an estimate of the true sky map. The CLEAN algorithm, originally introduced by

[55] and the “Maximum Entropy Method” (MEM) [22] are the common methods of deconvolution.

Chapter 3

Radio Foregrounds and Rotation Measure Synthesis

Overview

This chapter presents a brief theoretical review of the diffuse synchrotron emission and Faraday rotation. We then discuss the simulation algorithm used to produce the foreground maps with rotation in this research.

Author's comment: Part of this work is taken from: **T. Ansah-Narh**, F. B. Abdalla, O. M. Smirnov, K. M. B. Asad and J. R. Shaw, (2018). Simulations of Systematic Direction-dependent Instrumental Effects in Intensity Mapping Experiments. Monthly Notices of the Royal Astronomical Society (MNRAS), published. It is therefore, widely recognized that some of the text and figures will match that of the article. Therefore, this comment serves as a general reference for all such text.

3.1 Galactic Foreground

The measurements of redshifted CO and 21 cm emissions are very powerful tools to understand the star formation and survey the structure of the Universe respectively. The emission emerging from different astrophysical sources, other than the signals mentioned above, results in the foreground emission whose magnitude can be the higher than fourth order of the expected signals. The EM emission from particles normally electrons accelerated by the death of a star and supernova remnant, in the presence of a magnetic field, is called the *synchrotron emission*. The synchrotron emission from the Galaxy dominates at low microwave frequencies ($\lesssim 30$ GHz), whilst that of thermal dust emission is at higher frequencies ($\gtrsim 70$ GHz). Between these two components in frequency, lies the thermal free-free and non-thermal dust emissions,

which are formed as a result of spinning dust grains [88] as shown in Fig. 3.1. The free-free emission (also known as thermal bremsstrahlung) is obtained from thermally hot electrons ($\gtrsim 10^4$ K) [109] scattering uniformly in the interstellar plasma hence, having a completely zero polarisation. In the case of the thermal dust emission, it is formed from dust grains that get warmed by the interstellar radiation field and then emit far-infrared light which eventually lead to multiple temperatures. The dust grains are composed of Polycyclic Aromatic Hydrocarbons (PAHs), silicates, and graphites.

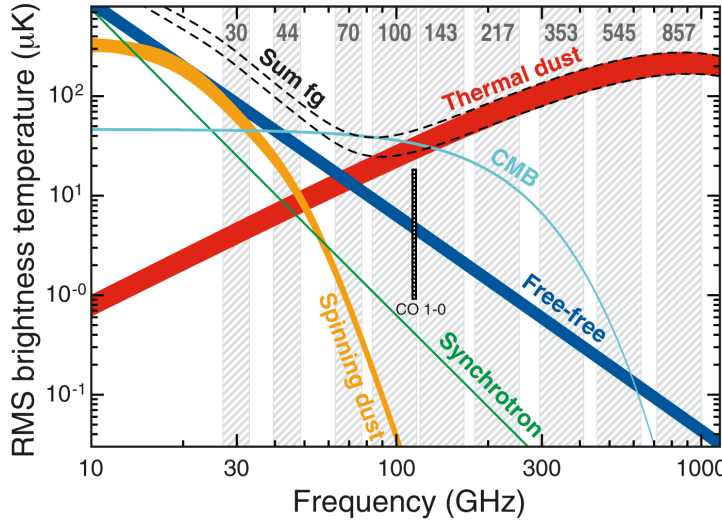


Figure 3.1: Brightness temperature distribution for the components of the Galactic foregrounds with respect to frequency. The angular resolution for the temperature of each smooth component is 1° . *Credit:* This figure is obtained from [88].

Detailed discussion of the components of the Galactic foregrounds, paying particular attention to their contributions to the polarization measurements can be found in [5, 56, 100, 128].

3.1.1 Diffuse Galactic Synchrotron Emission

In Section 3.1, we emphasized that the intensity of the synchrotron radiation relies on the strength of the magnetic field and the cosmic-ray energy. The distribution of this energy can be given as a function of a power law (also known as scaling law) such that $N_E \propto E^{-\tau}$, where $E > 10$ GeV is the energy [3] and $\tau \approx 3.0$ is the spectral index of the energy distribution (this index value is usually accepted when modelling in synchrotron and magnetic field).

The intensity of a synchrotron radiation S_{sync} with a frequency ν is defined as [75]:

$$S_{\text{sync}}(\nu) = \varepsilon_{\text{sync}}(\nu) \int_z n_e B_\perp^{(1+\tau)/2} dz \quad (3.1)$$

where Equation 3.1 is integrated with respect to the sight-line z , n_e is cosmic ray density and $B_\perp = \sqrt{B_x^2 + B_y^2}$ is the x, y components of the magnetic field of the sky.

From the power law, we can express the emissivity term $\varepsilon_{\text{sync}}(\nu)$ as:

$$\varepsilon_{\text{sync}}(\nu) = \varepsilon_0 \nu^{-(\tau-1)/2} \quad (3.2)$$

Recall Rayleigh-Jeans law at frequency ν :

$$B_\nu(T) = \frac{2\nu^2 k_B T}{c^2} \quad (3.3)$$

where c denotes the speed of light, k_B being the Boltzmann constant and T is the temperature in Kelvin. Using Equation 3.3, we can convert Equation 3.1 into a brightness temperature T_{sync} at frequency ν :

$$T_{\text{sync}}(\nu) = \frac{c^2 S_{\text{sync}}(\nu)}{2k_B \nu^2} \quad (3.4)$$

Hence, expressing T_{sync} as a power law, we get:

$$T_{\text{sync}}(\nu) = T_{\text{sync}}(\nu_0) \left(\frac{\nu}{\nu_0} \right)^{\gamma_{\text{sync}}} \quad (3.5)$$

where $\gamma_{\text{sync}} = -(\tau + 3)/2$. The spectral index γ_{sync} , changes at different frequency bands as displayed in Table 3.1.

Table 3.1: Measured Spectral Indices at Different Frequency Bands

γ_{sync}	Frequency Band (GHz)
-2.55	0.045 – 0.408
-2.71	0.408 – 2.30
-3.01	2.300 – 33.0

Fig. 3.2 is the 408 MHz full-sky survey taken from the LAMBDA-Data Products¹ [92] and originally produced by [52, 53] displaying the sky in mollview form in Galactic coordinates at a frequency where the diffuse synchrotron emission is most dominant. We can clearly observe other sources outside the Milky Way such as Cen A galaxy and the Magellanic clouds. An in-depth explanation on the concept of synchrotron emission is conferred in [71].

¹https://lambda.gsfc.nasa.gov/product/foreground/fg_2014_haslam_408_info.cfm

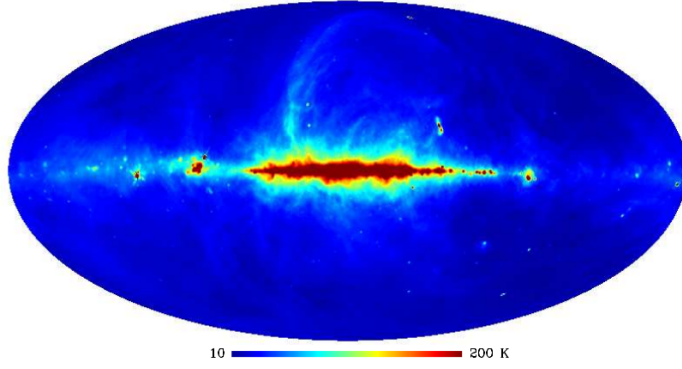


Figure 3.2: 408 MHz Full-Sky Map [52] projected in HEALPix, ring and defined in Galactic coordinates. Data and images can be retrieved from the LAMBDA website.

However, studies such as [56, 54] have shown that generally, the diffuse Galactic synchrotron emission is incompletely linearly polarised. This is due to the “spatial and energy distribution of the cosmic ray electrons, as well as the strength and orientation of the perpendicular (with respect to the line of sight) component of the Galactic magnetic field” [56]. Note that the distribution of charge particles can alter smoothly with pitch angle and this can eliminate the circular part and hence, become partially linearly polarised. Therefore, using the cosmic rays and magnetic field distributions of a galaxy, we can predict the polarisation foreground from the synchrotron emission and then separate it from observed maps. The degree of linear polarisation integrated over all electron energy and frequency is computed as $l = (\tau + 1)/(\tau + 7/3)$ [56, 71]. The polarisation factor (l) can be increased to 0.75 if the cosmic ray spectral index $\tau \approx 3$. We can express the polarised intensity in terms of Stokes parameters Q and U at frequency ν such that:

$$lI_\nu = \sqrt{Q_\nu^2 + U_\nu^2} \quad (3.6)$$

with the angle of polarisation given as:

$$\varphi_\nu = \frac{1}{2} \arctan \left(\frac{U_\nu}{Q_\nu} \right) \quad (3.7)$$

Therefore, in the Q, U plane, the modulus of the complex linear polarisation is computed as $(|Q_\nu + jU_\nu|)$. From Equation 3.1, we can integrate the polarised parameters (Q and U) along the sight-line z as [75]:

$$Q_{\text{sync}}(\nu) = l_{\text{sync}} \varepsilon_{\text{sync}}(\nu) \int_z n_e B_\perp^{(1+\tau)/2} \cos(2\alpha) \sin(\beta) dz \quad (3.8)$$

and

$$U_{\text{sync}}(\nu) = l_{\text{sync}} \varepsilon_{\text{sync}}(\nu) \int_z n_e B_\perp^{(1+\tau)/2} \sin(2\alpha) \sin(\beta) dz \quad (3.9)$$

where $\cos(2\alpha) = \frac{B_x^2 - B_y^2}{B_\perp^2}$ $0 < \cos(2\alpha) < 1$,

$$\sin(2\alpha) = -\frac{B_x^2 B_y^2}{B_\perp^2} \quad 0 < \sin(2\alpha) < 1 \text{ and } \sin(\beta) = \sqrt{1 - \frac{B_x^2}{B_\perp^2}} \quad 0 < \sin(\beta) < 1.$$

3.2 Faraday Rotation Measure Synthesis

Usually, light is not polarized when created but can be made so by transporting it through a medium which transmits electric fields oriented in a specific direction and absorbs all others. Radio emission from astronomical sources, such as galactic and extra-galactic sources and pulsars is often linearly polarized. Of course, other sources such as OH masers from galactic star formation due to Zeeman splitting are mostly circularly polarized [94]. Generally, polarization in radio astronomy is related to the presence of magnetic fields. For instance, radio emission due to synchrotron radiation is linearly polarized with the electric vectors and it is directed at right angles to the magnetic field in the line of emission onto the sky plane [12]. However, the polarization direction may alter as the radio waves propagate through the ISM. This effect is called the Faraday rotation and it allows radio astronomers to understand the magnetic field strength in the line-of-sight for both ISM and Earth's ionosphere.

The degree of polarization of Faraday rotation is quantified in terms of its rotation measure (Φ_{RM}) and it is mathematically expressed as;

$$\chi(\lambda) = \chi_0 + \Phi_{RM} \cdot \lambda^2 \quad (3.10)$$

such that,

$$\Phi_{RM} = 0.81 \int_{source}^{observer} n_e \vec{B} \cdot d\vec{l} \quad (3.11)$$

where the polarization angle measured at wavelength λ is $\chi(\lambda)$, χ_0 is the intrinsic polarization, n_e is the density electron in cm^{-3} , \mathbf{B} in μG describes the magnetic field and l in pc denotes the length of path. $\vec{B} \cdot d\vec{l}$ describe the direction of the magnetic field along the sight line.

The observed complex polarization is described by [18] as $P(\lambda^2) = pI \exp(2j\chi)$, where p is the degree of polarization. Substituting Equation 3.10 for χ in [18] equation and integrating over all possible values of the rotation measure to get;

$$P(\lambda^2) = \int_{-\infty}^{+\infty} pI \exp(2j[\chi_0 + \Phi_{RM} \cdot \lambda^2]) d\Phi_{RM} \quad (3.12a)$$

$$= \int_{-\infty}^{+\infty} F(\Phi_{RM}) \exp(2j\Phi_{RM} \cdot \lambda^2) d\Phi_{RM} \quad (3.12b)$$

where the intrinsic polarized flux is characterised by the *Faraday dispersion function* $F(\Phi_{RM})$ in terms of Faraday depth. Note how the expression in Equation 3.12b takes the form of a Fourier transform. Therefore, we can invert Equation 3.12b to obtain the intrinsic polarization in terms of observable quantities to have;

$$F(\Phi_{RM}) = \int_{-\infty}^{+\infty} P(\lambda^2) \exp(-2j\Phi_{RM} \cdot \lambda^2) d\lambda^2 \quad (3.13)$$

In the next section, we present how to simulate the polarized sky maps used in this research and account for the Faraday rotation.

3.3 Simulation

We apply the CORA software package² [106, 105] to reproduce the complete polarization sky maps at different frequencies as shown in Figs. 3.3 to 3.7. Even though the foreground simulations are produced in a scheme similar to those described in [106], we have significantly expanded the description in this work to make it more self contained.

As now described in [7], the polarization sector is simulated by generating a distribution of polarized emission in Faraday space. This is designed to make simulations sufficiently complex in the spectral direction, roughly reproduce the polarized amplitude across the sky, but does not attempt to match polarization angles anywhere. In addition, the spectral structure of the polarized signal from the galaxy occurs because the emission is from a range of Faraday depths. As suggested, the 3D structure of the galaxy, particularly the magnetic field means that emission from different regions along the line-of-sight collect varying amounts of Faraday rotation. In general, this gives complicated frequency dependent polarized structure with multiple independent Faraday components [127, see Figure 9]. Accurate mapping of this distribution is difficult, but is being attempted by projects such as GMIMS³ [126]. The most useful full-sky polarization measurements come from 1.4 GHz surveys [125, 116], the WMAP 23 GHz [13], and Planck 30 GHz maps [87]. However, because of the uncertain amount of instrumental depolarization in the former and the much higher frequencies of the latter, these are more useful to tell us about the general properties of the polarized sky (such as the high galactic latitude polarization fraction, see [64]) and less about the specific realisation on the sky. Due to these drawbacks, the level of polarization within the galactic plane produced in the simulations is appropriate for IM experiments.

²<https://github.com/radiocosmology/cora/>

³Global Magneto-Ionic Medium Survey

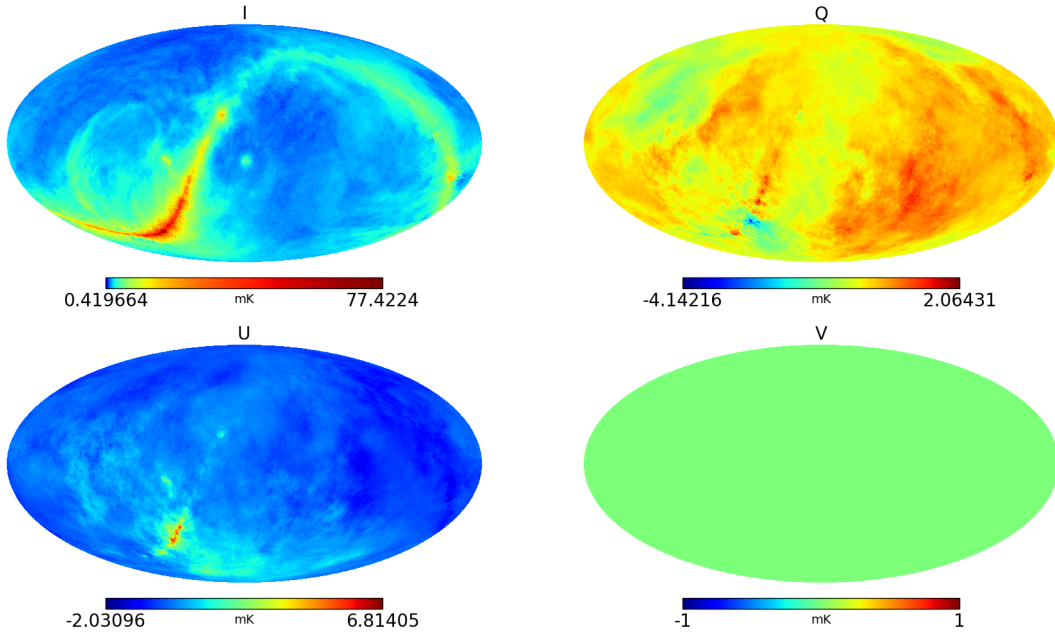


Figure 3.3: 1000 MHz full-sky simulated synchrotron maps. These synchrotron maps characterize the full-sky polarization maps for our low resolution simulated observations and are presented here in the mollweide projection form defined by equatorial coordinates in terms of Stokes parameters I, Q, U and V .

Below is the scheme used to generate the foreground simulations:

- (i) A 3D base map for the unpolarized sky is produced by extrapolating the 408 MHz [53] map to the requested set of frequencies using the spectral index of map of [75] which was produced by comparing the Haslam map with WMAP 23 GHz polarization data, assuming that both are dominated by synchrotron emission. This produces a map with power law spectral behaviour with angular fluctuations on scales $\gtrsim 1^\circ$ scales.
- (ii) Angular and spectral fluctuations are added into the 3D maps according to an angular power spectrum.

$$C_\ell(\nu, \nu') \propto \left(\frac{\ell}{\ell_0}\right)^{-2.8} \left(\frac{\nu \nu'}{\nu_0^2}\right)^{-2.8} \exp\left[-\frac{1}{2}\left(\frac{\ln \nu/\nu'}{4}\right)^2\right], \quad (3.14)$$

taken from [99]. We use a position dependent scaling on large scales to ensure the fluctuations to match their observed variance across the sky [67], and ensure that we don't add in additional fluctuations on scales constrained by the Haslam map by projecting out the dominant eigenmodes on these scales.

- (iii) To simulate the polarized sky, we use the ideas of Faraday Rotation Measure Synthesis [16] and a simple model of the distribution of emission in Faraday depth across the full sky, which we then integrate over to generate the polarized output at each desired frequency. To produce the emission in Faraday space, we use the rotation measure map of [81] to indicate the characteristic scale

of the distribution of emission in Faraday depth. We tune the amplitude and correlation properties in Faraday space to crudely reproduce the polarization fraction in the WMAP 23 GHz map and the 1.4 GHz surveys. The polarization directions are generated as a Gaussian random field at each Faraday depth. For the interested reader, more details of this are found in [106].

- (iv) Known bright point sources on the sky are included explicitly, with their polarizations Faraday rotated to the desired frequencies using the [81] map. Faint sources ($S < 10$ Jy at 151 MHz) are randomly generated.

Finally, we use the “Hierarchical Equal Area isoLatitude Pixelation” (**HEALPix**⁴) software [19, 48] to project the simulated full-sky maps into equal pixel area, using a resolution of $N_s = 512$. This makes our gridded map to uniformly distribute $12N_s^2$ pixels onto a unit sphere. The regular synchrotron maps in Figs. 3.3 to 3.7 are depicted in **HEALPix** format at different frequencies.

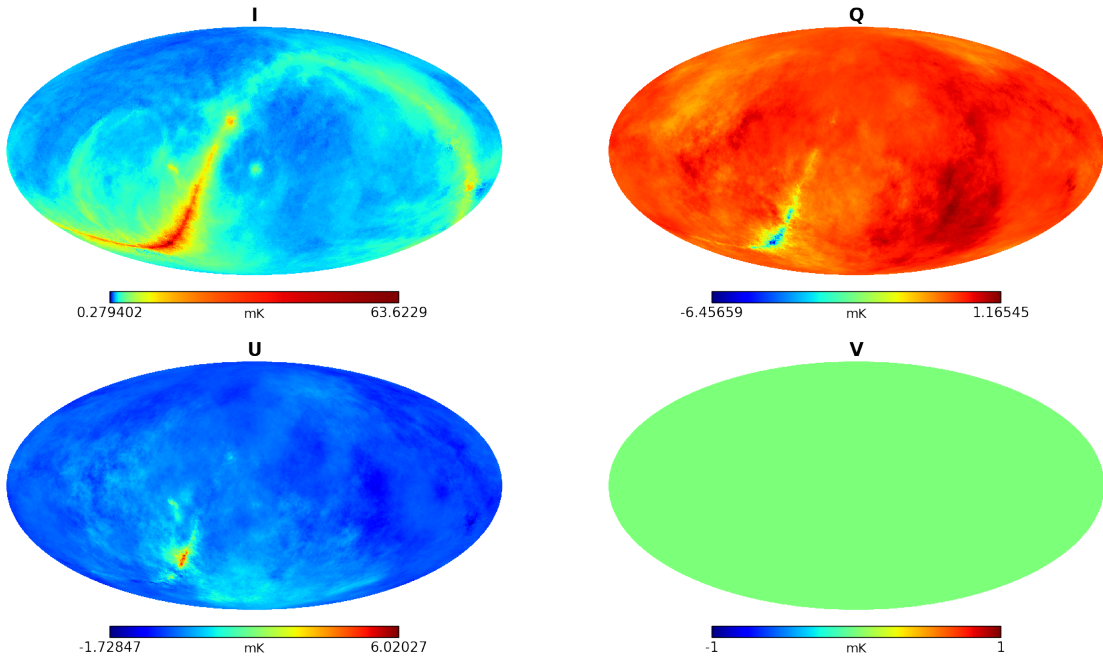


Figure 3.4: Simulated foreground maps at 950 MHz displayed in mollweide form.

⁴<http://healpix.sourceforge.net/>

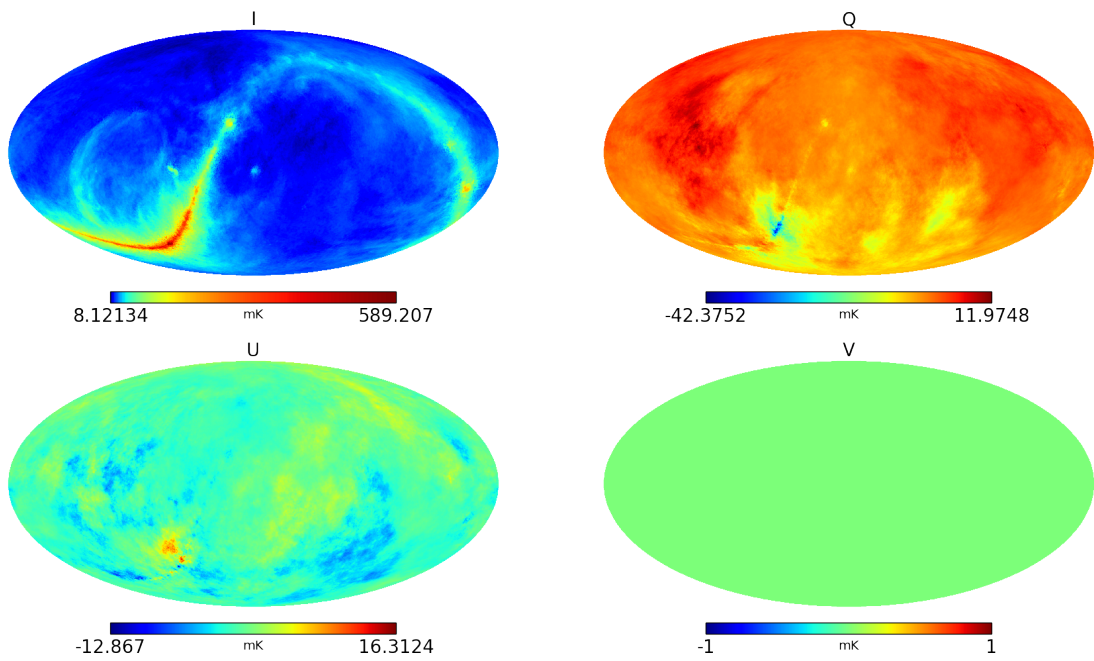


Figure 3.5: Simulated foreground maps at 450 MHz presented in mollweide form.

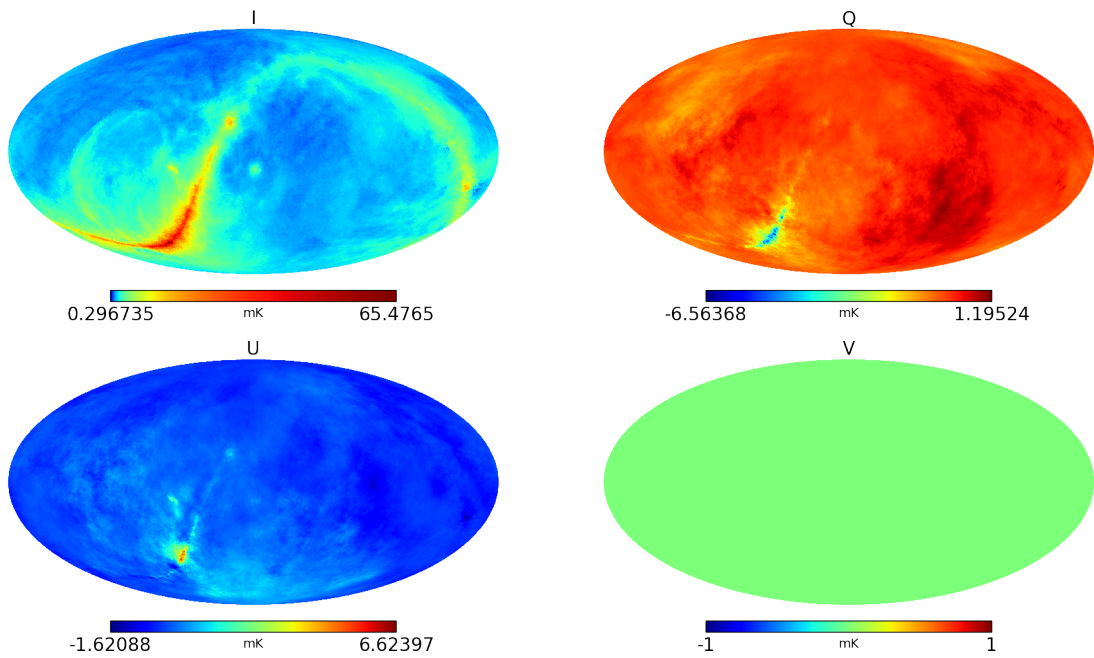


Figure 3.6: Simulated foreground maps at 990.5 MHz displayed in mollweide form.

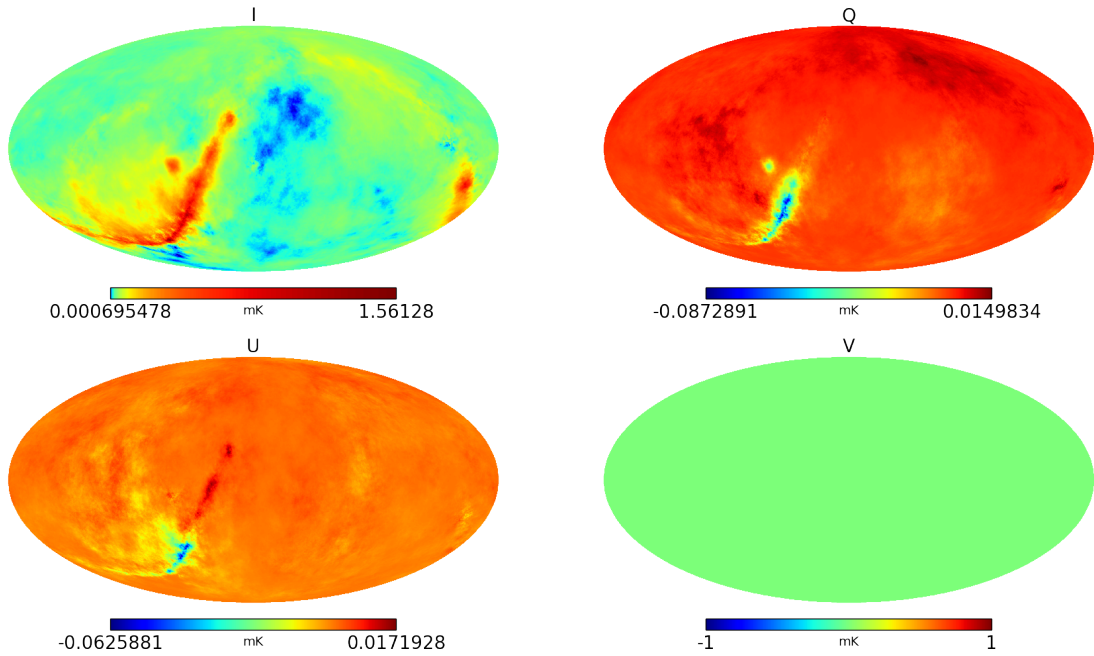


Figure 3.7: Simulated foreground maps at 13.6 GHz presented in mollweide form.

Chapter 4

Investigating Primary Beam Effects on HI Intensity Mapping

Overview

Chapter Four presents a notional primary beam simulations of KAT-7 using the OS-KAR software. These beams are corrupted and then use for intensity mapping experiments.

Author's comment: This work draws largely on: **T. Ansah-Narh**, F. B. Abdalla, O. M. Smirnov, K. M. B. Asad and J. R. Shaw, (2018). Simulations of Systematic Direction-dependent Instrumental Effects in Intensity Mapping Experiments. Monthly Notices of the Royal Astronomical Society (MNRAS), published. It is therefore, widely recognized that most of the text and all the figures and captions in Chapter 4 and Appendix 4.1 will be the same as that of the article. Hence, this note serves as a universal reference for all such text and figures.

4.1 Modelling the Primary Beam

A radio antenna usually contains a receiving element that accepts an EM wave in a particular direction. When we integrate the effective accumulating region of a radio instrument over the Sky position (ϑ, φ) , we obtain the *primary beam* (PB) of the instrument. We can make the receiving signal to be more directive by putting multiple receiving elements normally close to each other and then measure the signal. The radio signals induced in different elements of the array are then combined to form a single output of the interferometer. This combination technique is referred to as *beam-forming*. Some of the sophisticated software packages for generating the antenna beam

patterns are **GRASP**¹, **FEKO**² and the Cassegrain antenna software (**cassbeam**³)^[17]. The first two packages are EM simulators and they are mostly used to produce the voltage pattern for the ideal case. The latter package applies the technique of ray tracing to measure the complex beam patterns by tracing a ray from the feed to the point on the secondary reflector, then bounces towards the main reflector and finally reflect to the aperture plane.

The main focus of this chapter is to use the **OSKAR**⁴ [34] beam pattern simulator to simulate an array of stations and try to distort them in an appreciable way. Each station is designed as a phased array of dipoles which is an appropriate replica for the KAT-7⁵ dishes. This is technically possible to do with **GRASP** or **FEKO**, but impractically expensive for our purposes (primarily because of the many perturbed patterns required). On the other hand, a physically *precise* model of the KAT-7 PB is not actually needed, since future IM observations will not be carried out by KAT-7. KAT-7 is a notional example that is adopted for the purposes of this study. What is rather needed is a relatively cheap way to compute ideal and perturbed beams, with perturbations that are representative of those seen in actual telescopes.

Unlike the EM softwares above, the **OSKAR** simulator can be accessed publicly and more importantly, it uses an accelerated GPU (“Graphics Processing Unit”) to improve the computational performance of the digital beam-forming simulation for aperture arrays [34, 76]. In addition, it has the ability to include the following for each station beam response:

- (i) Introduce independent specification of pointing direction for each station or tile,
- (ii) Introduce apodisation weighting (this will modify the shape of the station beam),
- (iii) Introduce antenna element position and dipole orientation error and
- (iv) Introduce systematic and random element phase and gain errors.

Lastly, the simulator is also capable of simulating interferometers produced from large aperture arrays by utilising the Radio Interferometer Measurement Equation (RIME) [50, 108] to generate the simulated visibilities. In summary, this software is relatively ‘flexible’ to use for the scope of this chapter compared to the previous softwares discussed above. Read the manual to understand how to use the setup file to run this package.

Below, we show that **OSKAR** can be used to compute ‘dish-like’ PBs, by generating a geometric dipole distribution that mimics the aperture illumination function (AIF) of a dish. We stress that the resulting beam pattern is completely notional, and cannot

¹<http://www.ticra.com/products/software/grasp>

²<https://www.feko.info/product-detail/overview-of-feko>

³<https://github.com/ratt-ru/cassbeam>

⁴<http://www.oerc.ox.ac.uk/~ska/oskar2/>

⁵<http://public.ska.ac.za/kat-7/>

be treated as a physically accurate model of the KAT-7 beam. It is, however, broadly representative of the dish beam. Furthermore, perturbations with respect to this ideal notional beam can be readily generated by perturbing the dipole distribution. The OSKAR approach gives us a practical way of generating such ideal and perturbed beams. As pointed out above, this is sufficient for the purposes of our work.

4.2 KAT-7 Beam Pattern Simulation

KAT-7 was produced as a forerunner to the 64-dish MeerKAT⁶ radio telescope array and demonstrated South Africa’s ability to host the SKA [130]. The MeerKAT instrument is currently fully operational and approaching the completion of its commissioning programme [14, 41]. When KAT-7 was in operation with only seven 12 m dishes scattered over a 200 m baseline, it was considered a compact radio telescope, both in terms of resolution and sensitivity but now it is opposed by MeerKAT and the SKA which occupy much larger areas. Its L-band radio receivers had cryogenically cooled front-ends to about 70 K (-203 °C) in order to increase the system’s sensitivity. In addition, its configuration was superb for observing nearby galaxies, which emitted radio waves on a large scale.

In producing a ‘dish-like’ OSKAR beam model, we consider the dipole points to be dispersed in a 2-D mode. Note, this will ensure that we imitate the AIF of a ‘KAT-7-like’ dish. In this work, we look at two main AIF features along these lines:

- (i) Make the number of dipoles less dense towards the dish-like edge in order to obtain the feed illumination pattern.
- (ii) Introduce an aperture barrier in the dish-like model. This aperture obstruction is due to the four anchored struts and the feed firmly fixed at the centre.

In point (i), mathematically, we can express this by defining the dipole locations as $(d_x, d_y) = (\Lambda \cos \varphi, \Lambda \sin \varphi)$, where the degree of orientation φ , is uniformly distributed over the interval $[0, 2\pi]$ and Λ denotes the distribution of the dipoles across the radius of the dish. We model Λ by drawing 1-D randomly generated values from a cumulative distribution function (CDF) of a known probability density function. Here, we adopt the Super Gaussian (also known as the Generalized Normal function) distribution $h_\Lambda(r)$ [89, 31] to model Λ , thus:

$$h_\Lambda(r) = \frac{\sqrt{\beta}}{2s\Gamma(\frac{1}{\beta})} e^{-\left|\frac{r-\bar{r}}{s\sqrt{2}}\right|^\beta} \quad (4.1)$$

where s depicts the normal deviation, β denotes the peak point, and the Gamma distribution Γ , is written in standard form as $\Gamma(\alpha) = \int_0^\infty v^{\alpha-1} e^{-v} dv$. Next, we compute the CDF of Equation 4.1, using the error function $erf(\varpi)$ such that:

$$erf(\varpi) = 1 - \frac{1}{\sqrt{\pi}} \Gamma(1/2, \varpi^2) \quad (4.2)$$

⁶<http://www.ska.ac.za/gallery/meerkat/>

If we put $\beta = 2$ in Equation 4.1, the normal distribution is produced and the respective CDF becomes:

$$\int_{-\infty}^r h(r'|\bar{r}, s^2) = \frac{1}{2} \left[1 + \operatorname{erf} \left(\frac{r' - \bar{r}}{s\sqrt{2}} \right) \right] \quad (4.3)$$

Substitute Equation 4.2 into Equation 4.3 to get:

$$\Psi_\beta(r) = 1 - \frac{1}{2\sqrt{\pi}} \Gamma \left(\frac{1}{2}, \frac{r - \bar{r}}{s\sqrt{2}} \right) \quad (4.4)$$

Extending Equation 4.4 into the general form in Equation 4.1, we obtain the CDF:

$$H_\beta(r) = \begin{cases} \frac{\Gamma\left(\frac{1}{\beta}, \left\{\frac{r - \bar{r}}{s\sqrt{2}}\right\}^\beta\right)}{2\Gamma\left(\frac{1}{\beta}\right)}, & \text{if } r \leq \bar{r} \\ 1 - \frac{\Gamma\left(\frac{1}{\beta}, \left\{\frac{r - \bar{r}}{s\sqrt{2}}\right\}^\beta\right)}{2\Gamma\left(\frac{1}{\beta}\right)}, & \text{if } r > \bar{r} \end{cases} \quad (4.5)$$

Using the *inverse transform approach* and the CDF in Equation 4.5, we can generate the uniform random values u within the range $[0, 1]$, such that $A = |H_\beta^{-1}(u)|$. Eventually, we obtain the radial distribution of the dish as a “flat-top Gaussian” as presented in Fig. 4.1, left.

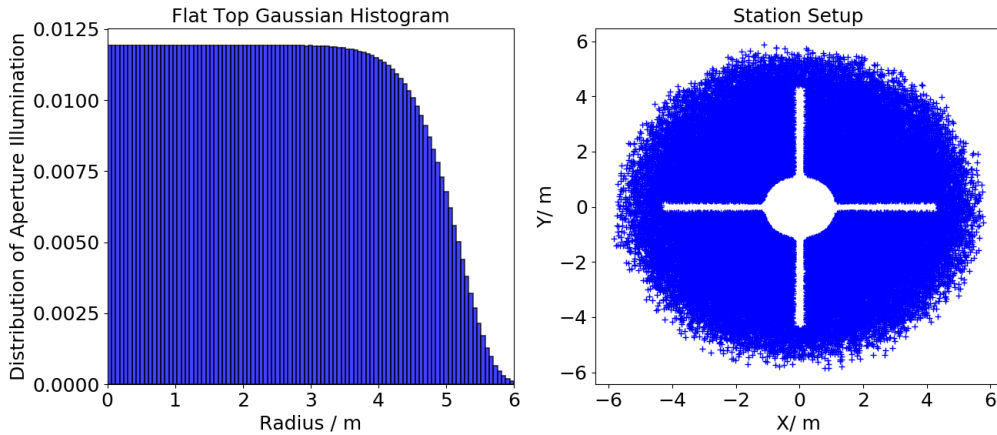


Figure 4.1: The aperture illumination of dish-like surface is modelled using 80000 dipoles. LEFT PLOT: The ‘flat-top Gaussian’ radial distribution of dipole positions, mimicking a realistic aperture illumination where the dipoles get less dense towards the edge of the dish. RIGHT PLOT: The resulting 2D dipole distribution with a mask applied to mimic aperture blockage.

The parameters of the Super Gaussian distribution, s and β control the width of the distribution and the aggressiveness of the taper. The values adopted in this work to produce the radial distribution in the figure are $s = 0.82$ and $\beta = 12.0$.

We imitate the aperture blockage in point (ii) by simply masking the 2D positions. This ultimately results in the dipole distribution shown in Fig. 4.1, right. This dipole

distribution is then fed into OSKAR as the ‘station layout’. For a given set of observational parameters (in particular, pointing at zenith), OSKAR then computes the station primary beam response⁷. The resulting *Jones matrix* elements are shown in Fig. 4.2. Note how the beam pattern is broadly similar to that expected from a prime-focus dish. In particular, the first side-lobe shows the four-fold symmetry caused by the strut blockage. The presence of the phase component in Fig. 4.2b clearly shows that the so-called ideal beam is not that perfect since we are randomly placing the dipoles in the KAT-7 dish-like form, hence, the norminal X and Y dipoles are not directly orthogonal. In effect, we get the maximum $rmse \approx 0.10\%$ perturbed inaccuracies on the dish surface as reported in Fig. 4.3.

⁷This takes ≈ 3 minutes on a Tesla K40 GPU.

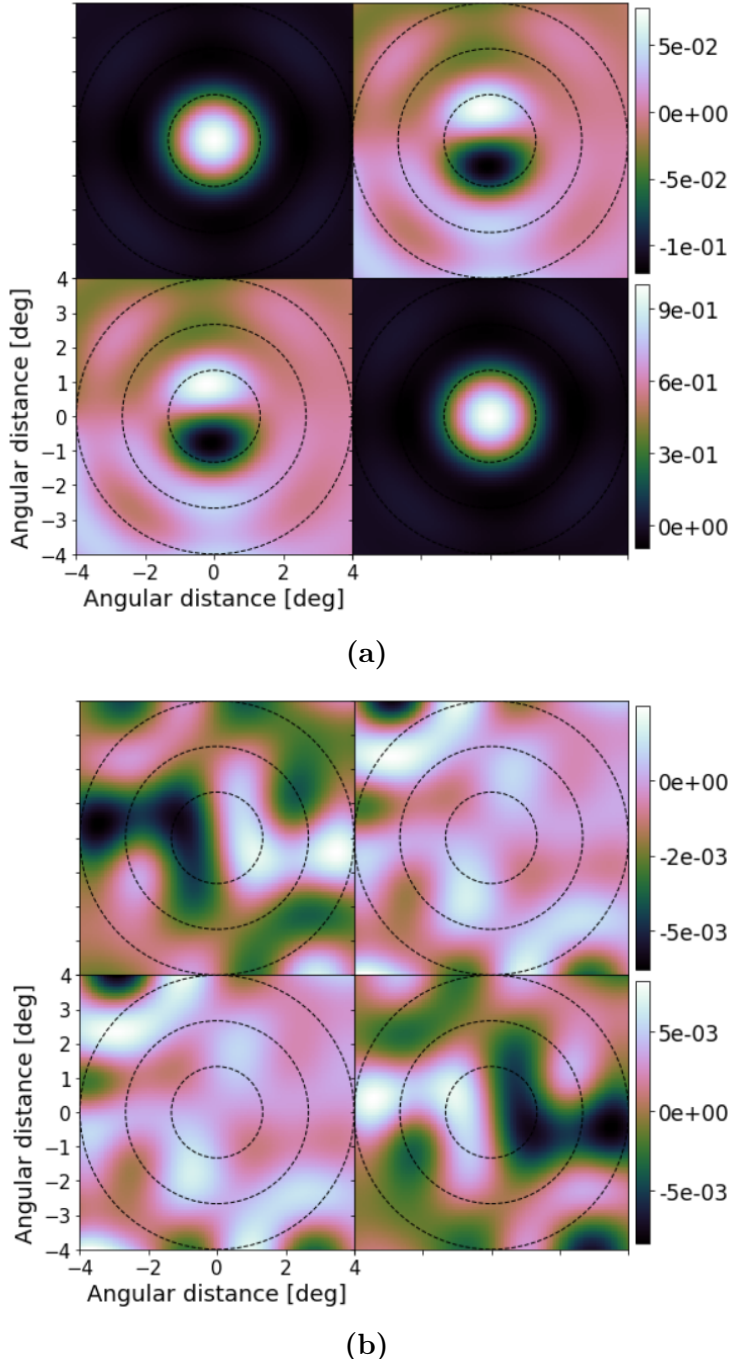


Figure 4.2: Jones matrix representation of the KAT-7-like beams produced by OSKAR and shown at 1 GHz: (a) real part (b) imaginary part. The intensity of the imaginary parts increases with fewer dipoles and becomes smaller when more dipoles are used. The four panels in (a) and (b) show XX (top-left), XY (top-right), YX (bottom-left) and YY (bottom-right). Note that the notations X and Y denote the horizontal and vertical linear polarised beams.

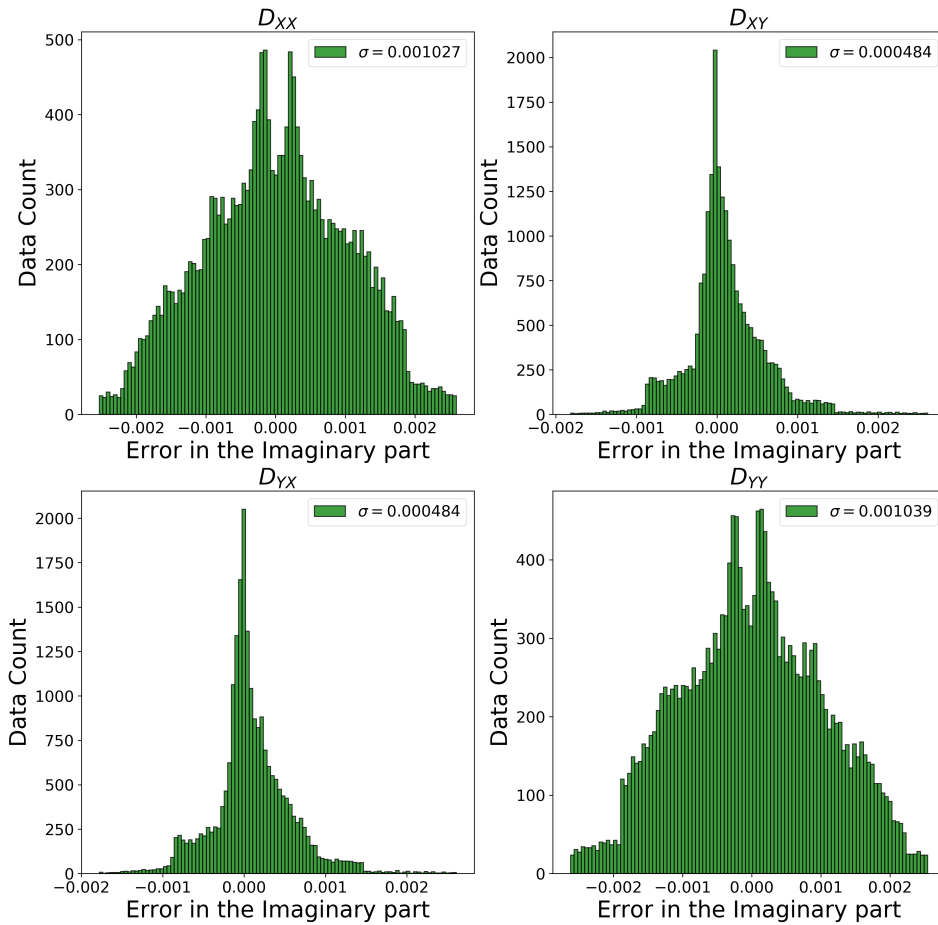


Figure 4.3: Histogram plots of the imaginary components in Fig. 4.2 showing the distribution of inaccuracies on the KAT-7 dish-like surface.

Note that the Jones [60, 59] formalism, initially designed to describe optical polarization, was used by [50] in radio interferometry and further extended to direction-dependent effects by [108]. In the next section, we adapt the derivations of the latter two works.

4.2.1 Jones and Mueller matrices

An electromagnetic plane wave propagating along axis z can be described, at any point in space and time, by two complex amplitudes, e_x and e_y . Conventionally, we arrange these into a column vector, $\mathbf{e} = [e_x, e_y]^T$. A single-dish observation aims to measure the pairwise coherencies of these amplitudes:

$$\mathbf{x} = \begin{bmatrix} \langle e_x e_x^* \rangle \\ \langle e_x e_y^* \rangle \\ \langle e_y e_x^* \rangle \\ \langle e_y e_y^* \rangle \end{bmatrix} = \langle \mathbf{e} \otimes \mathbf{e}^* \rangle, \quad (4.6)$$

where $\langle \cdot \rangle$ represents the average over a time/frequency interval, and \otimes is the outer (or Kronecker) product operator. From these measured coherencies, the Stokes parameters $IQUV$ (written as a column vector \mathbf{s}) may be derived, by definition, as [15]:

$$\mathbf{s} = \begin{bmatrix} I \\ Q \\ U \\ V \end{bmatrix} = \begin{bmatrix} \langle e_x e_x^* \rangle + \langle e_y e_y^* \rangle \\ \langle e_x e_x^* \rangle - \langle e_y e_y^* \rangle \\ \langle e_x e_y^* \rangle + \langle e_y e_x^* \rangle \\ -i(\langle e_x e_y^* \rangle - \langle e_y e_x^* \rangle) \end{bmatrix} \quad (4.7)$$

We can rewrite this in terms of a 4×4 conversion matrix \mathbf{S}^{-1} as⁸:

$$\mathbf{s} = \begin{bmatrix} 1 & 0 & 0 & 1 \\ 1 & 0 & 0 & -1 \\ 0 & 1 & 1 & 0 \\ 0 & -i & i & 0 \end{bmatrix} \mathbf{x} = \mathbf{S}^{-1} \mathbf{x}. \quad (4.8)$$

What the instrument actually measures is a set of pairwise correlations between two voltages induced by the EM field on two orthogonal mode feeds, v_a and v_b . The Jones formalism assumes that these are linearly related to the EM field (i.e. that all signal propagation effects are linear). This can be written as $\mathbf{v} = \mathbf{J}\mathbf{e}$, where \mathbf{v} is a column vector of the two voltages, and the 2×2 *Jones matrix* \mathbf{J} describes signal propagation. The *measured* coherency \mathbf{x}' can then be written as:

$$\mathbf{x}' = \langle \mathbf{v} \otimes \mathbf{v}^* \rangle = (\mathbf{J} \otimes \mathbf{J}^*) \langle \mathbf{e} \otimes \mathbf{e}^* \rangle = (\mathbf{J} \otimes \mathbf{J}^*) \mathbf{x}, \quad (4.9)$$

⁸This follows [108] in defining \mathbf{S} as the conversion matrix between Stokes vectors and coherency vectors, $\mathbf{v} = \mathbf{S}\mathbf{s}$. Conversely, \mathbf{S}^{-1} operates in the opposite direction. Note that [50] use \mathbf{T} to refer to \mathbf{S}^{-1} .

and the measured Stokes parameter vector \mathbf{s}' relates to the original Stokes vector via the so-called *Mueller matrix* \mathbf{M} :

$$\mathbf{s}' = \mathbf{M}\mathbf{s} = \mathbf{S}^{-1}(\mathbf{J} \otimes \mathbf{J}^*)\mathbf{S}\mathbf{s} \quad (4.10)$$

For the purposes of this work, we ignore all propagation effects except the primary beam.

Therefore, expanding the Jones terms in Equation 4.10, we can measure the full elements of \mathbf{M} , thus:

$$\mathbf{J} \otimes \mathbf{J}^* = \begin{pmatrix} j_{xx}j_{xx}^* & j_{xx}j_{xy}^* & j_{xy}j_{xx}^* & j_{xy}j_{xy}^* \\ j_{xx}j_{yx}^* & j_{xx}j_{yy}^* & j_{xy}j_{yx}^* & j_{xy}j_{yy}^* \\ j_{yx}j_{xx}^* & j_{yx}j_{xy}^* & j_{yy}j_{xx}^* & j_{yy}j_{xy}^* \\ j_{yx}j_{yx}^* & j_{yx}j_{yy}^* & j_{yy}j_{yx}^* & j_{yy}j_{yy}^* \end{pmatrix} \quad (4.11)$$

If we substitute Equation 4.11 into 4.10, we can then expand \mathbf{M} in terms of Jones matrix elements:

$$m_{II} = (j_{xx}j_{xx}^* + j_{xy}j_{xy}^* + j_{yx}j_{yx}^* + j_{yy}j_{yy}^*)/2 \quad (4.12a)$$

$$m_{IQ} = (j_{xx}j_{xx}^* - j_{xy}j_{xy}^* + j_{yx}j_{yx}^* - j_{yy}j_{yy}^*)/2 \quad (4.12b)$$

$$m_{IU} = (j_{xx}j_{xy}^* + j_{xy}j_{xx}^* + j_{yx}j_{yy}^* + j_{yy}j_{yx}^*)/2 \quad (4.12c)$$

$$m_{IV} = i(j_{xx}j_{xy}^* + j_{yx}j_{yy}^* - j_{xy}j_{xx}^* - j_{yy}j_{yx}^*)/2 \quad (4.12d)$$

$$m_{QI} = (j_{xx}j_{xx}^* + j_{xy}j_{xy}^* - j_{yx}j_{yx}^* - j_{yy}j_{yy}^*)/2 \quad (4.12e)$$

$$m_{QQ} = (j_{xx}j_{xx}^* - j_{xy}j_{xy}^* - j_{yx}j_{yx}^* + j_{yy}j_{yy}^*)/2 \quad (4.12f)$$

$$m_{QU} = (j_{xx}j_{xy}^* + j_{xy}j_{xx}^* - j_{yx}j_{yy}^* - j_{yy}j_{yx}^*)/2 \quad (4.12g)$$

$$m_{QV} = i(j_{xx}j_{xy}^* - j_{yx}j_{yy}^* - j_{xy}j_{xx}^* - j_{yy}j_{yx}^*)/2 \quad (4.12h)$$

$$m_{UI} = (j_{xx}j_{yx}^* + j_{yx}j_{xx}^* + j_{xy}j_{yy}^* + j_{yx}j_{xy}^*)/2 \quad (4.12i)$$

$$m_{UQ} = (j_{xx}j_{xy}^* - j_{xy}j_{xx}^* + j_{yx}j_{yy}^* + j_{yy}j_{yx}^*)/2 \quad (4.12j)$$

$$m_{UU} = (j_{xx}j_{yy}^* + j_{yy}j_{xx}^* + j_{xy}j_{yx}^* + j_{yx}j_{xy}^*)/2 \quad (4.12k)$$

$$m_{UV} = i(j_{xx}j_{yy}^* + j_{yx}j_{xy}^* - j_{yy}j_{xx}^* - j_{xy}j_{yx}^*)/2 \quad (4.12l)$$

$$m_{VI} = i(-j_{xx}j_{yx}^* + j_{yx}j_{xx}^* - j_{xy}j_{yy}^* + j_{yy}j_{xy}^*)/2 \quad (4.12m)$$

$$m_{VQ} = i(-j_{xx}j_{yx}^* + j_{yx}j_{xx}^* + j_{xy}j_{yy}^* - j_{yy}j_{xy}^*)/2 \quad (4.12n)$$

$$m_{VU} = i(-j_{xx}j_{yy}^* + j_{yy}j_{xx}^* - j_{xy}j_{yx}^* + j_{yx}j_{xy}^*)/2 \quad (4.12o)$$

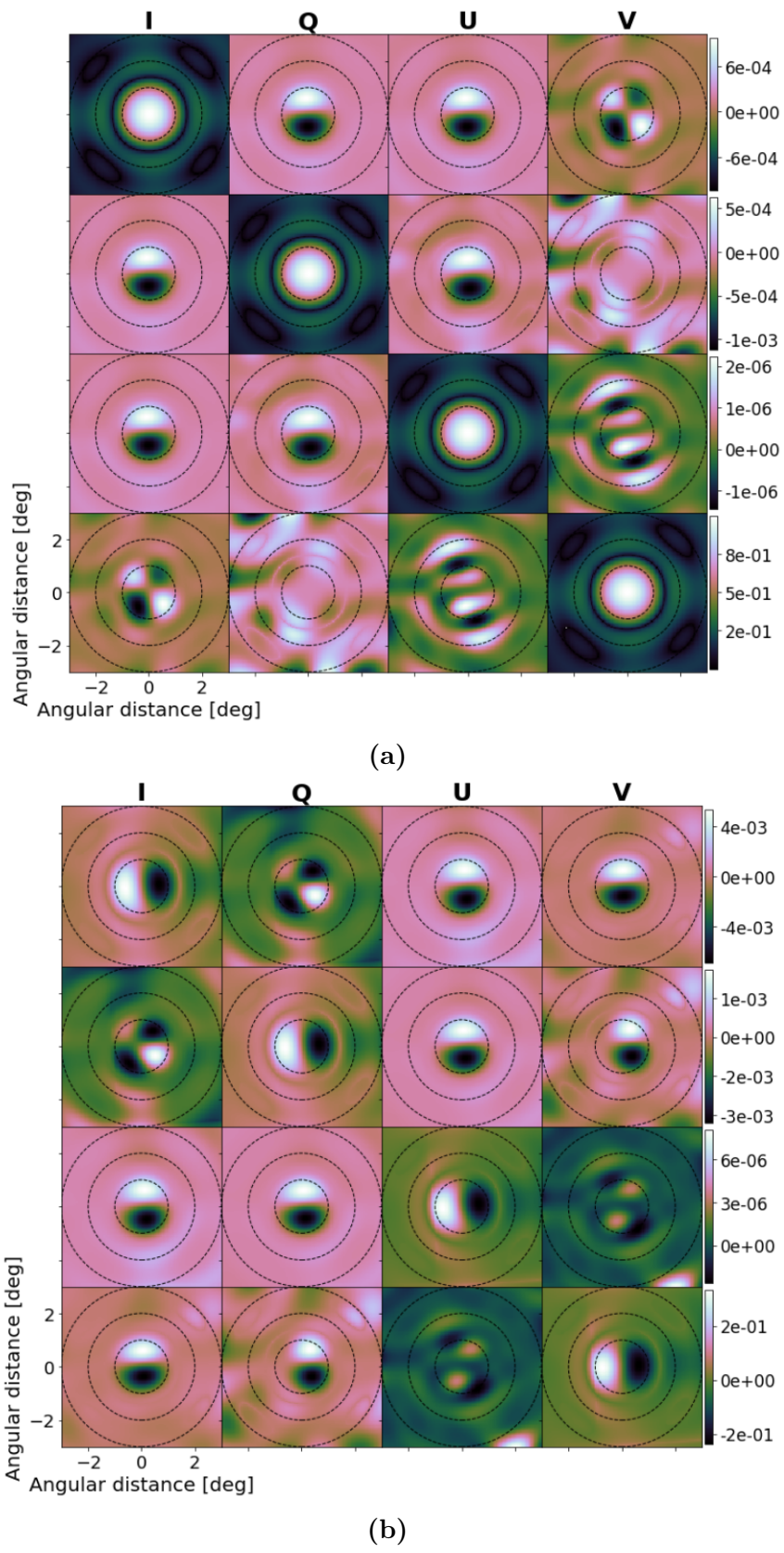
$$m_{VV} = (j_{xx}j_{yy}^* - j_{yx}j_{xy}^* + j_{yy}j_{xx}^* - j_{xy}j_{yx}^*)/2 \quad (4.12p)$$

The sixteen elements in Equations 4.12a to 4.12p are the complete PBs of a radio telescope (as shown in Fig. 4.4) produced from the complex beams (see Fig. 4.2). The DD effect of the PB will cause each element in Equation 4.12 to produce different matrices. If we substitute the elements in Equation 4.12 into Equation 4.10, we get the measured Stokes parameters in Equation 4.13:

$$\begin{pmatrix} S'_I \\ S'_Q \\ S'_U \\ S'_V \end{pmatrix} = \begin{pmatrix} m_{II} & m_{IQ} & m_{IU} & m_{IV} \\ m_{QI} & m_{QQ} & m_{QU} & m_{QV} \\ m_{UI} & m_{UQ} & m_{UU} & m_{UV} \\ m_{VI} & m_{VQ} & m_{VU} & m_{VV} \end{pmatrix} \begin{pmatrix} S_I \\ S_Q \\ S_U \\ S_V \end{pmatrix} \quad (4.13)$$

Note the physical meaning of the matrix elements. The on-diagonal terms of the Jones matrix describe the sensitivity of each feed, as a function of direction, to its matched EM field component. The off-diagonal terms describe leakage, i.e. the sensitivity of the feed to the nominally orthogonal EM field component. This leakage is due to mechanical and electronic imperfections in the antennas and feeds. The diagonal terms of the Mueller matrix describe the sensitivity of the measured Stokes $IQUV$ components to their true counterparts, as a function of direction. The off-diagonal terms describe spurious leakage between the measured Stokes components. We can schematically write this as;

$$\mathbf{M} = \begin{bmatrix} I \rightarrow I' & Q \rightarrow I' & U \rightarrow I' & V \rightarrow I' \\ I \rightarrow Q' & Q \rightarrow Q' & U \rightarrow Q' & V \rightarrow Q' \\ I \rightarrow U' & Q \rightarrow U' & U \rightarrow U' & V \rightarrow U' \\ I \rightarrow V' & Q \rightarrow V' & U \rightarrow V' & V \rightarrow V' \end{bmatrix}$$



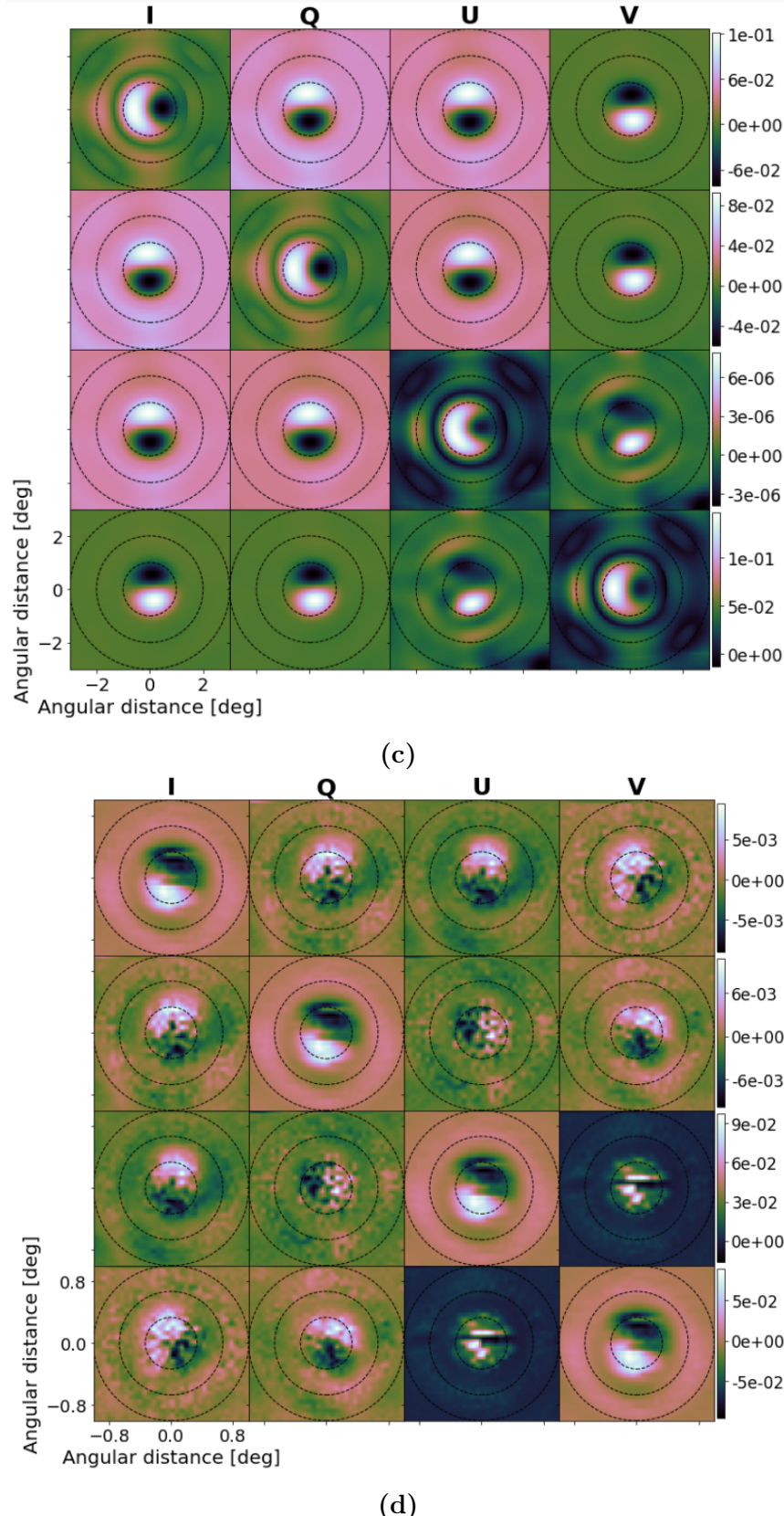


Figure 4.4: Mueller matrix representations of full polarization beams produced at 1 GHz (a) 4×4 images of KAT-7 uncorrected OSKAR beams. (b) Fractional differences between the uncorrected OSKAR beams in Fig. 4.4a and the gain and phase error beams in appendix A.1a (c) Fractional differences between uncorrected OSKAR beams in Fig. 4.4a and the dipole orientation error beams in appendix A.1b. (d) Fractional differences between VLA holography measured beams in Figs. A.2a and A.2b.

4.2.2 Primary Beam Perturbation

For the purpose of this research, we try to introduce some distortions on the simulated OSKAR beams for IM experiment. The first type is to corrupt both the gain and phase of the beam in a systematic manner. Here, we can do this with OSKAR by simulating the gain and phase of each element so that the weight of the beamformer W_B at a particular time t , for a given pointing direction (ϑ_B, φ_B) and dipole locations (v_1, v_2, v_3) is given in [7] as:

$$W_B(\mathbf{v}) = (G_B^0 + G_B^{error}) W_B^{geo}(\mathbf{v}) e^{j(\varphi_B^0 + \varphi_B^{error})} \quad (4.14)$$

The parameters $\mathbf{v} = (\vartheta_B, \varphi_B, v_1, v_2, v_3, t)$, G_B^{error} and φ_B^{error} use the Gaussian function to generate deterministic random numbers at step-time t . We then combine these parameters with G_B^0 (the gain), φ_B^0 (phase) and the geometrical kernel function W_B^{geo} , to obtain the array factor for beam evaluation. For the purpose of our “disk-like” simulation, we introduced 5° phase error and 10% gain error into the beam-forming weight to distort the beams as shown in Fig. A.1a. These types of errors represent imperfections in the parabolic reflector surface (which, in real life, result in amplitude and phase errors over the aperture). The second perturbation is to introduce positional errors per element. Note that for ideal situation, both dipoles (x, y) are orthogonal and the angular differences will be zero. However, displacing the dipoles from its nominal positions ($\sim 1^\circ$) will definitely produce an angular difference of being greater than zero, hence, creating a systematic error in the feed angle and the effect of this is presented in Fig. A.1b. Here, what we do is to indicate the Euler angles of the feeds of the nominal x and y dipoles in each station directory. These angles depict the differences from zero, since in the ideal case both dipoles are expected to be orthogonal and in the plane of the station platform. Figs. 4.4b and 4.4c show the beam errors produced by computing the differences between the true modelled beams in Fig. 4.4a and the two distorted beams in Figs. A.1a and A.1b respectively. The on-diagonal components of these beam errors represent the residual leakages and the off-diagonals show the residual systematic leakages. The maximum residual leakages produced in Figs. 4.4b and 4.4c are $\simeq 20\%$ and 10% respectively.

Another thing that we considered in this work is to apply the JVLA holography beams to measure the degree of beam perturbation. The numerical scheme used to generate the JVLA beams in Figs. A.2a and A.2b is described in the EVLA Memo [85] which involves the use of Fourier transform to determine the far-field beam pattern of an antenna. Fig. 4.4d is the residual error of the JVLA beams, producing $\simeq 10\%$ leakage. Therefore, the systematic leakage in the holography beams indicates that the simulated perturbations introduced in the OSKAR beams are actually practical.

Now that we are abreast with the model of the instrument, we continue to show how we apply these beams to the simulated full-sky maps discussed in Chapter 3.

4.3 Convolution of Foreground Maps

Mathematically, convolution is an operator that interpolates two expressions Υ_α and Υ_β to produce a third function χ that is typically viewed as a modification of one of the original functions. Consider $C_v(\varsigma)$ to be the convolution of $\Psi_\alpha(\varsigma)$ with $\Psi_\beta(\varsigma)$, then its Fourier pair $\chi(\nu)$, is the product of $\Upsilon_\alpha(\nu)$ and $\Upsilon_\beta(\nu)$ which define the Fourier pairs of $\Psi_\alpha(\varsigma)$ and $\Psi_\beta(\varsigma)$ respectively. Thus,

$$\Psi_\alpha(\varsigma) \odot \Psi_\beta(\varsigma) \rightleftharpoons \Upsilon_\alpha(\nu) \cdot \Upsilon_\beta(\nu) \quad (4.15)$$

where the symbol \odot denotes the convolution operator. By definition,

$$\begin{aligned} C_v(\varsigma) &= \Psi_\alpha(\varsigma) \odot \Psi_\beta(\varsigma) \\ &= \int_{-\infty}^{\infty} \Psi_\alpha(\varsigma') \Psi_\beta(\varsigma - \varsigma') d\varsigma \end{aligned} \quad (4.16)$$

Taking the Fourier transform of both sides in Equation 4.16, we get:

$$\begin{aligned} \chi(\nu) &= \int_{-\infty}^{\infty} C_v(\varsigma) e^{-2\pi j \nu \varsigma} d\varsigma \\ &= \int_{-\infty}^{\infty} \int_{-\infty}^{\infty} \Psi_\alpha(\varsigma') \Psi_\beta(\varsigma - \varsigma') e^{-2\pi j \nu \varsigma} d\varsigma' d\varsigma \end{aligned} \quad (4.17)$$

Let $y = \varsigma - \varsigma' \Rightarrow dy = d\varsigma'$

$$\chi(\nu) = \int_{-\infty}^{\infty} \int_{-\infty}^{\infty} \Psi_\alpha(\varsigma') \Psi_\beta(y) e^{-2\pi j \nu (\varsigma' + y)} d\varsigma' dy \quad (4.18)$$

Equation 4.18 can therefore be separated to give:

$$\begin{aligned} \chi(\nu) &= \int_{-\infty}^{\infty} \Psi_\alpha(\varsigma') e^{-2\pi j \nu \varsigma'} d\varsigma' \cdot \int_{-\infty}^{\infty} \Psi_\beta(y) e^{-2\pi j \nu y} dy \\ &= \Upsilon_\alpha(\nu) \cdot \Upsilon_\beta(\nu) \end{aligned} \quad (4.19)$$

Expressing the general definition in Equation 4.19 into 2D discrete form, we have:

$$\begin{aligned} \chi(\nu_\alpha, \nu_\beta) &= \Psi_\alpha(\nu_\alpha, \nu_\beta) \odot \Psi_\beta(\nu_\alpha, \nu_\beta) \\ &= \sum_{m=-\infty}^{\infty} \sum_{n=-\infty}^{\infty} \Psi_\alpha(m - \nu_\alpha, n - \nu_\beta) \Psi_\beta(m, n) \end{aligned} \quad (4.20)$$

In Equation 4.20, the values $\chi(\nu_\alpha, \nu_\beta)$ of the discrete function χ for any particular (ν_α, ν_β) follows by multiplying each value $\Psi_\beta(m, n)$ of the discrete function Ψ_β with a kernel function $\Psi_\alpha(m - \nu_\alpha, n - \nu_\beta)$ between a particular (ν_α, ν_β) and varying (m, n) where, $(-\infty < m, n < +\infty)$. Thus, each value $\chi(\nu_\alpha, \nu_\beta)$ of the function χ is a weighted mean of the values $\Psi_\beta(m, n)$ with weights $\Psi_\alpha(m - \nu_\alpha, n - \nu_\beta)$ defined by the function Ψ_α . In this chapter, we apply similar approach to simulate the foreground of the sky. To perform an IM experiment, the radio telescope(s) is pointed at different patches of the sky so that the instrument can measure the overall intensity emerging

from patches from the autocorrelation of the radio signal, as a function of frequency. In order to emulate this observation technique in our IM simulation, the discrete convolution in Equation 4.21 is used to measure the intensities of the full sky synchrotron maps in Fig. 3.3. Let (θ, ϕ) denote the celestial coordinates of the foregrounds of the sky, such that \mathbf{B} are the fully polarised beams and \mathbf{f}_{sky} are the foregrounds of the sky. We can then model the convolved foregrounds to be:

$$\begin{aligned}\mathbf{F}^{\text{conv}}(\theta, \phi) &= \mathbf{B}(\theta, \phi) \odot \mathbf{f}_{\text{sky}}(\theta, \phi) \\ &= \sum_{(\theta', \phi') = \lfloor (\theta, \phi) \rfloor} \mathbf{B}(\theta' - \theta, \phi' - \phi) \cdot \mathbf{f}_{\text{sky}}(\theta', \phi')\end{aligned}\quad (4.21)$$

where $(\theta', \phi') \leq npix$ and the symbol $\lfloor \cdot \rfloor$ denotes the nearest pixels. The measured foreground pixel values $\mathbf{F}^{\text{conv}}(\theta, \phi)$ of the discrete function \mathbf{F}^{conv} for any particular (θ, ϕ) follows by multiplying each foreground pixel value $\mathbf{f}_{\text{sky}}(\theta, \phi)$ of the discrete function \mathbf{f}_{sky} with a beam $\mathbf{B}(\theta' - \theta, \phi' - \phi)$ between a particular (θ', ϕ') and varying (θ, ϕ) . Thus, each pixel value $\mathbf{F}^{\text{conv}}(\theta, \phi)$ of the function \mathbf{F}^{conv} is a weighted mean of the pixel values $\mathbf{f}_{\text{sky}}(\theta, \phi)$ with weights $\mathbf{B}(\theta' - \theta, \phi' - \phi)$ defined by the function \mathbf{B} .

The convolution technique in Equation 4.21 is implemented in this work using the `HEALPix` query disc function (Python package). This function is applied on the `HEALPix` map (the full-sky map) with $N_{\text{side}} = 512$ to query all the nearby pixels that fall within the primary beamwidth for every pointing. These query pixels are then convolved with the corresponding pixel values in the beam. So for each pointing, we get different query pixels even though there can be overlapping pixels like the rings shown in Fig. 5.9a, as you point the beam to the next direction. To measure the exact intensity of the foreground, the convolved `HEALPix` map is normalised by the power beam (Stokes I). For instance, in Equation 4.21, if we let \mathbf{B} to be the complete beams in Fig. 4.4a and then replace \mathbf{f}_{sky} with Fig. 3.3, we generate \mathbf{F}^{conv} as shown in Fig. 4.5. We repeat the procedure, using the beams in Figs. A.1a and A.1b to obtain perturbed maps. Similarly, doing same for the JVLA beams in Figs. A.2a and A.2b, we produce their corresponding measured sky maps. In Fig. 4.5, we can observe that the spatial representation of the inclining maps from left to right are retained as that of the initial foreground images displayed in Fig. 3.3. This happens when we convolve the sky maps with the gain terms (i.e. m_{II}, m_{QQ}, m_{UU}).

In performing IM, we are mostly curious about the absolute intensity of the foreground. This can be done by transforming the spatial representation of the convolved sky maps into spherical harmonics in order to estimate the power spectrum in a scale of moments (l). The next section presents the angular power spectrum described in [7].

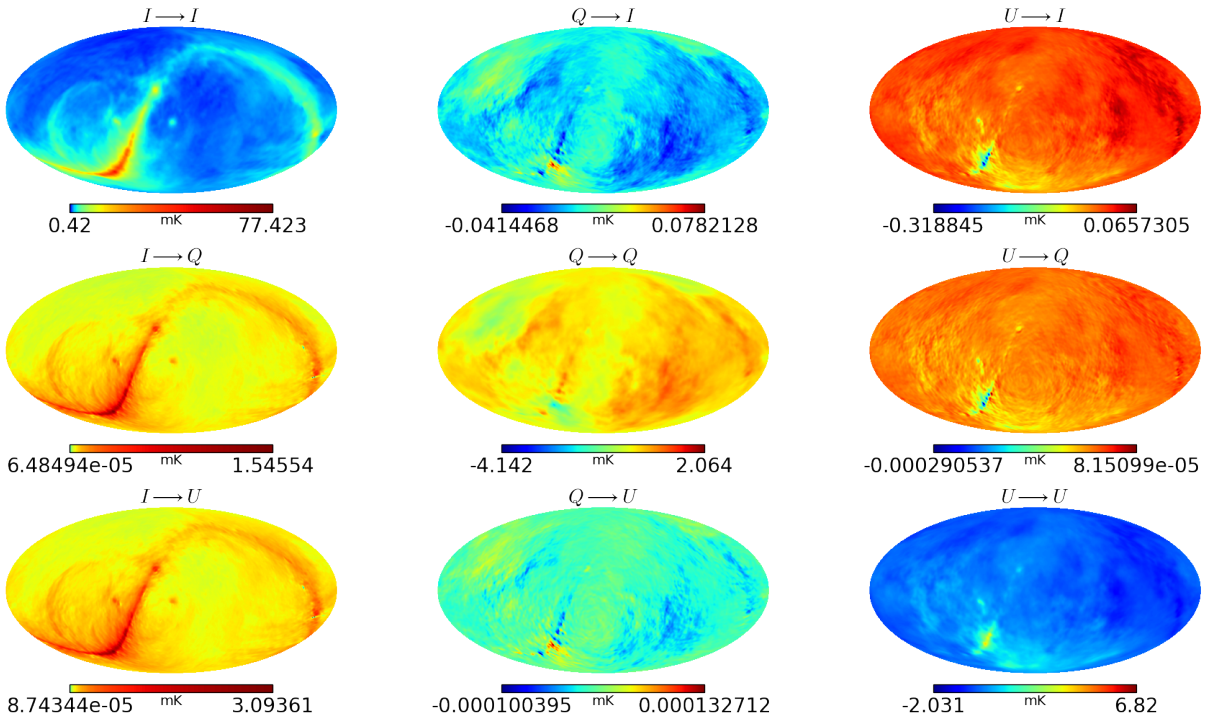


Figure 4.5: Convolved full-sky polarization maps using the non-distorted OS-KAR beams. For example, we used the m_{II} beam in Fig. 4.4a to convolve Stokes I in Fig. 3.3 and produce the convolved map $I \rightarrow I$, then we used m_{QI} beam to convolve Stokes Q to obtain the convolved map $Q \rightarrow I$, also, using the m_{UI} beam to convolve Stokes U we produced the convolved map $U \rightarrow I$. The other convolved maps are produced in the same manner using their respective beams.

4.3.1 Angular Power Spectrum

In CMB studies [1, 65, 129, 110, 96, 121], it is a common practice to characterise the distribution of flux in a sphere with the angular power spectrum. The same approach is employed in this project to describe the diffuse foreground intensity over spherical harmonics $Y_{l,m}$.

Consider the foreground of the sky is emitted by our own galaxy or the distribution galaxies emitting 21 cm with an intensity equivalent to $T(\hat{\sigma})$. We can measure the total source emission temperature $T(\hat{\sigma})$, in each sky pixel and represent the distribution as an expansion in 2D spherical harmonics:

$$T(\hat{\sigma}) = \sum_{l=0}^{\infty} \sum_{m=-l}^l a_{lm} Y_{lm}(\hat{\sigma}) \quad (4.22)$$

where $\hat{\sigma} \equiv (\psi, \xi)$ is the unit vector in some direction in the sky and $Y_{lm}(\hat{\sigma})$ are the spherical harmonic functions evaluated in the direction $\hat{\sigma}$, such that they form a complete orthonormal set on the unit sphere and can be expressed as:

$$Y_{lm}(\psi, \xi) = (-1)^m \sqrt{\frac{2l+1}{4\pi} \frac{(l-m)!}{(l+m)!}} P_l^m(\cos \psi) e^{im\xi} \quad (4.23)$$

In Equation 4.23, the indices $l = 0, \dots, \infty$ and $-l \leq m \geq l$ with P_l^m denoting the Legendre polynomials. l is known as the multipole which denotes a given angular scale γ in the sky, where $\gamma \simeq 180^\circ/l$. The coefficients a_{lm} in Equation 4.22,

$$a_{lm} = \int_{\psi=-\pi/2}^{\pi/2} \int_{\xi=0}^{2\pi} T_{lm}(\hat{\sigma}) Y_{lm}^*(\hat{\sigma}) d\xi d\psi \quad (4.24)$$

are related to what we normally do in the Fourier space.

Consider any two pixels, then the correlation function of the temperatures is expressed as;

$$C_{cr}(\Theta) = \langle T(\hat{\sigma}_i) T(\hat{\sigma}_j) \rangle, \quad \Theta = \sigma_i \cdot \sigma_j \quad (4.25)$$

where the brackets $\langle \rangle$, denote averaging over $2l+1$ values of m . Equation 4.25 strictly relies on the separation angle between two sources as discussed in [104, p. 78] and, therefore can be rewritten in terms of Legendre polynomials:

$$C_{cr}(\Theta) = \sum_{l=0}^{\infty} \frac{2l+1}{4\pi} C_l P_l(\cos \Theta) \quad (4.26)$$

From Equation 4.26, we can estimate the statistical distribution of the angular power spectrum \hat{C}_l of the entire sky in terms of a_{lm} :

$$\hat{C}_l = \frac{1}{2l+1} \sum_m |a_{lm}|^2, \quad -l < m < l \quad (4.27)$$

In this work, we used *anafast* in HEALPix library to compute the auto-power spectrum \hat{C}_l of foregrounds of the sky in Section 4.3 by executing an approximate,

discrete point-set quadrature on a sphere sampled at the HEALPix pixel centres. Spherical harmonic transforms are then computed using recurrence relations for Legendre polynomials on co-latitude ψ and Fast Fourier Transforms on longitude ξ .

4.4 Results and Analysis

The top three rows in Fig. 4.6 depict the total convolved full-sky images in Stokes parameters I, Q and U . If we convolve the initial sky maps in Fig. 3.3 with the correct modelled beams in Fig. 4.4a and then put their respective Stokes terms together, we obtain the images in the first row. We repeat the steps to produce the images in the second and third rows, but this time around, we use the false modelled beams in Fig. A.1. Note the similarities between these measured maps, if we compute the differences between the maps in the first and second rows and also, the first and third rows, we obtain the corresponding error maps in rows 4 and 5 respectively. Obviously, these simulated maps in Fig. 4.6 are not the same and this is even confirmed by the systematic differences presented in Fig. A.3, between the true convolved maps in Fig. 4.5 and the corrupted maps due to errors introduced in the gain and phase of the PBs. We then repeat the same approach using the JVLA measured beams displayed in Fig. A.2 to obtain the systematic error terms in Fig. A.4 and the overall measured full-sky maps reported in Fig. A.5. The main concept about applying the beams measured by holography on the initial complete maps in Fig. 3.3, is to examine the perturbation introduced in the angular power spectrum if we assume a simulated beam, whilst convolving with a measured beam.

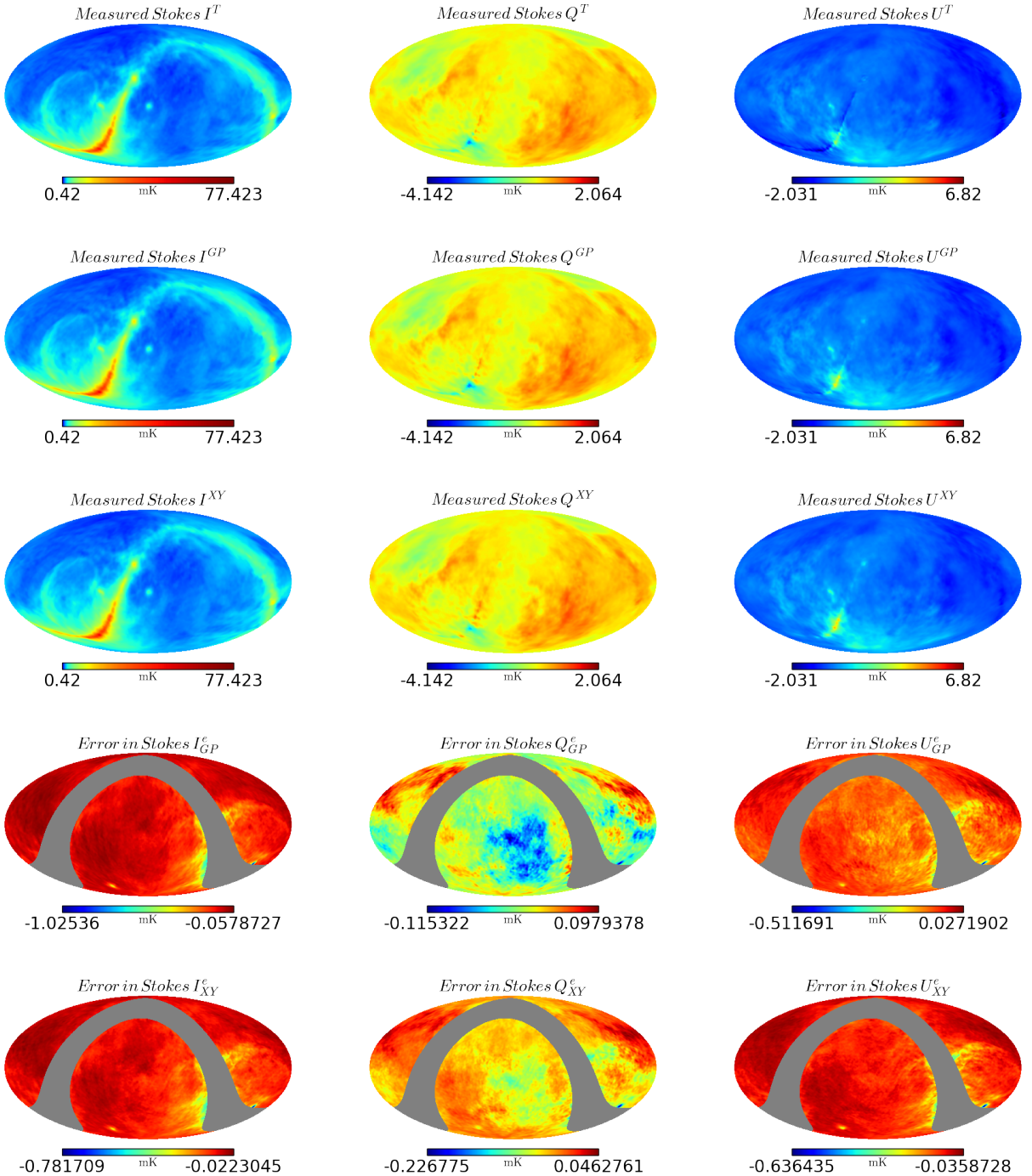


Figure 4.6: The 1st row maps depict the measured foregrounds of Stokes I , Q and U for using the non-distorted fully polarised beams in Fig. 4.4a whilst the 2nd and 3rd rows represent the corrupted measured foregrounds due to gain and phase and dipole orientation errors introduced into the beams respectively. The next two maps are the corresponding errors in I , Q and U .

The auto-power spectra presented in Fig. 4.7 estimate the density of the measured foregrounds at different multipole moments. The first three rows in column 1 show the respective power spectra plots of Stokes I , Q , U when we convolve the polarised foreground with true and gain and phase error beams produced from OSKAR. The next three rows in column 2 represent the power spectra plots of Stokes I , Q , U respectively when we convolve the polarised foreground with true and dipole position error beams also produced from OSKAR. The last rows in the third column depict the respective power spectra plots of Stokes I , Q , U when we convolve the polarised foreground with two station beams of the JVLA. Note how the beam power in each plot of both OSKAR and the holographic measured beams is normalised to 1. It is computed by finding the quotient of the power spectrum of the convolved sky map and the original sky map. In addition, note also in all cases, the PB effect of the convolved power spectrum. The OSKAR beam power plots in Stokes I , Q and U , converge at a multipole moment of $l = 60$. This value relates to an angular scale of 3.0° on the sky whilst the power spectra of the VLA beams converge just at a multipole moment of $l = 90$, giving an angular scale of 2.0° on the sky. The change in the value of multipole moments is because of different dish sizes which also results in producing different beamwidths. Furthermore, the angular scales computed are equivalent to the beam sizes used to convolve the original maps in Fig. 3.3. Note, even though we used two different aperture sizes for the simulation, the effect of these two PBs on the convolved power spectra of Stokes I , Q and U remains unaltered. This shows that in IM experiment, where we measure the collective emission from many sources, smaller and relatively cheaper instruments can be used. In this study, the measured values for the convolved power spectra of Stokes I , Q and U in both cases are 10 mK^2 , 0.1 mK^2 and 0.1 mK^2 respectively. Observe carefully how these values in Fig. 4.7 actually predicted the foreground's temperature of the true sky. Hence, the power spectrum of the corresponding errors in I , Q and U due to perturbation of the beams are $\approx 0.01 \text{ mK}^2$, 10^{-4} mK^2 and 10^{-5} mK^2 respectively.

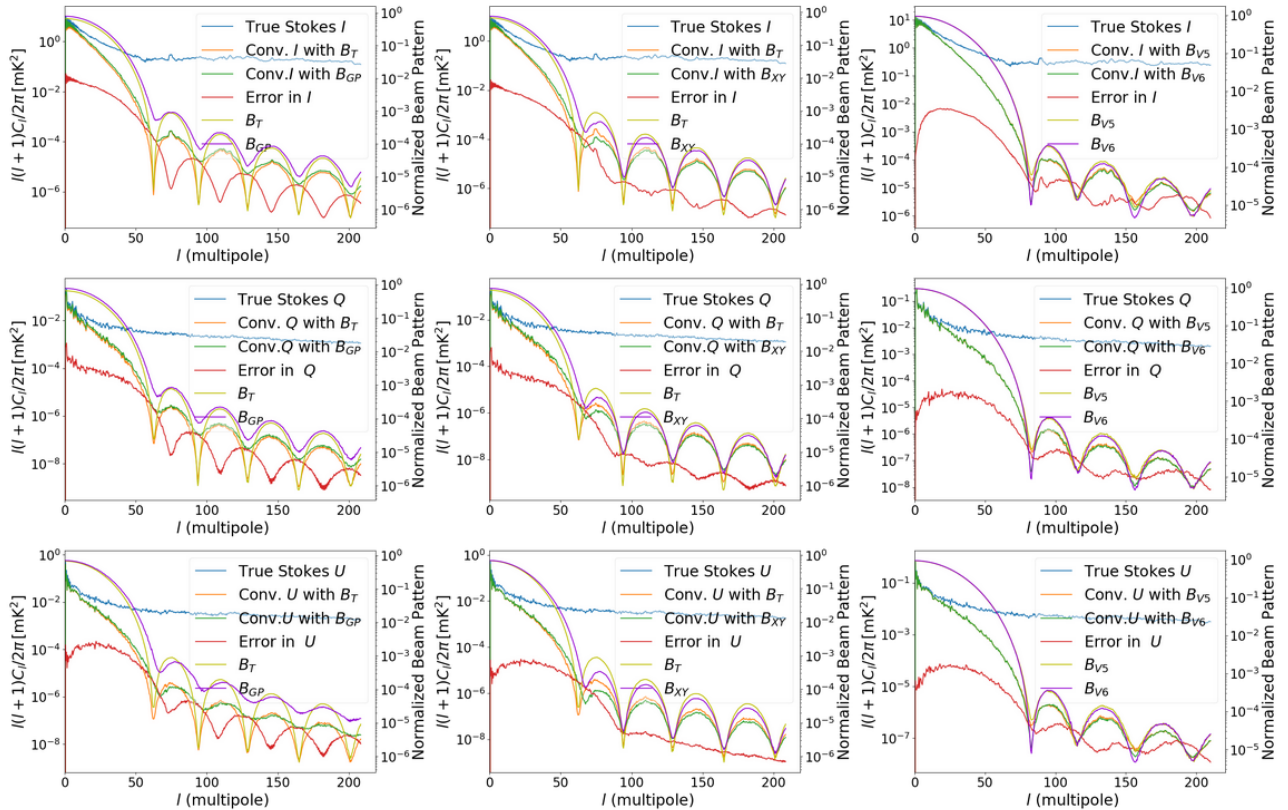


Figure 4.7: Convolved angular power spectra estimation of foreground maps. First row: Shows Stokes I spectra plots for using simulated beams and holography measured beams. Second row: Displays Stokes Q spectra plots for using simulated beams and holography measured beams. Third row: Displays Stokes U spectra plots for using simulated beams and holography measured beams.

The spectra plots in Fig. 4.8 depict the systematic effects of beam errors in Stokes I , Q and U . These residual plots are measured as a result of the respective differences between the perturbed and true measured full-sky maps. From the plots we can clearly observe that the systematic effects of beam errors between the simulated modelled beams and the holographic measurements differ by 2 or 3 orders of magnitude with respect to the multipole moment (l). This is due to the uncertainties introduced in the power spectrum estimation for considering a notional beam over a measured beam.

Table 4.1 shows the corresponding inaccuracies in the power spectrum estimation of Stokes I , Q and U . It is computed as the standard deviations of the sampling distributions of the residual maps. Here, the residuals are determined as a result of the respective differences between the distorted and non-distorted convolved full-sky maps as reported in Fig. A.3. This is repeated for the systematic error maps (of using the JVLA holography beams) in Fig. A.4. For instance, the standard errors introduced in $Q \rightarrow I$ are ≈ 0.015 (due to gain and phase errors) and 0.014 (due to the main dish surface orientation errors). Also, that of $U \rightarrow I$ are ≈ 0.005 and 0.0045 accordingly.

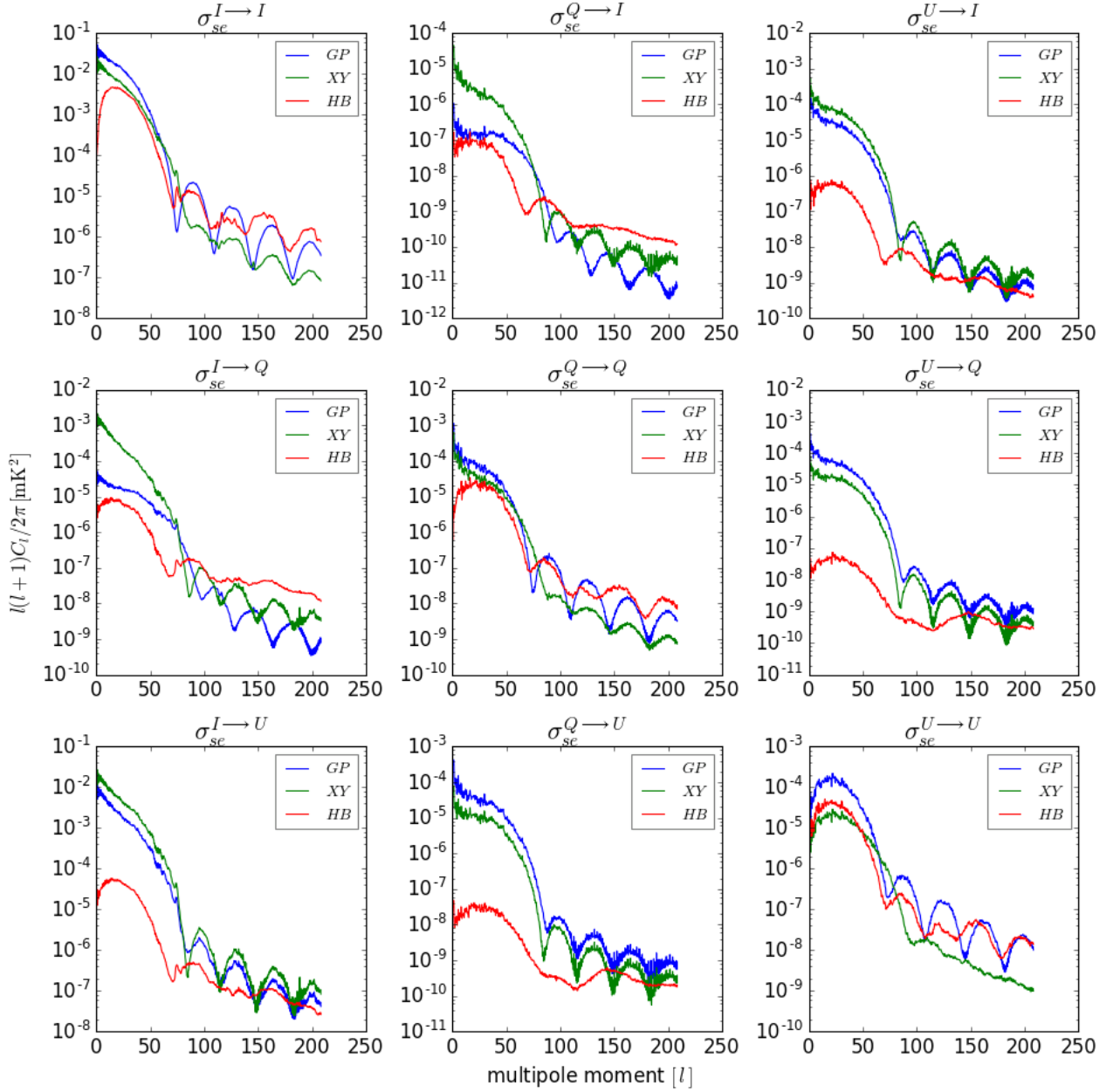


Figure 4.8: These are the spectra plots of the systematic errors as shown in Fig. A.3. The notations *GP* and *XY* in the legends denote the residuals for gain-phase and surface orientation errors in the simulated modelled beams, that of *HB* depicts the errors in the holography beams. These errors are then used to estimate the imperfections in the simulation by computing the expected value of the standard deviations of the sampling distributions of the residual maps to produce Table 4.1.

Table 4.1: Error introduced in the power spectrum estimation

<i>I</i>		<i>Q</i>		<i>U</i>		<i>TOTAL</i>	
<i>GP</i>	<i>XY</i>	<i>GP</i>	<i>XY</i>	<i>GP</i>	<i>XY</i>	<i>GP</i>	<i>XY</i>
<i>I</i>	0.0640	0.0640	0.0151	0.0137	0.0050	0.0045	0.0841 0.0822
<i>Q</i>	0.0010	0.0008	0.0221	0.0224	0.0007	0.0055	0.0238 0.0287
<i>U</i>	0.0007	0.0007	0.0194	0.0341	0.0354	0.0362	0.0555 0.0710

In IM experiments, the HI signal is measured in Stokes I , so we are particularly interested in the total intensity and the leakages from polarization into Stokes I (that is, $|Q + iU| \rightarrow I$). Fig. 4.9 shows how the $|Q + iU| \rightarrow I$ and the error in Stokes I map affect the HI signal. Here, a spherical power spectrum of the simulated model of 21 cm brightness temperature at $z \approx 0.67$ produced from the CRIME⁹ fast simulation software and described by [4] is generated and then compared with the spectra plots of the Galactic foregrounds. The HI signal power in the right side of the plot is higher than the $|Q + iU| \rightarrow I$ at a multipole moment of $l = 100$ which is about 4 orders of magnitude greater at lower scales. This occurs when we do not correct the beam errors (i.e., gain, phase and orientation) in Stokes I at all. The fractional leakage of $|Q + iU|/I$ is computed to give $\approx 1.0\%$ for the intrinsic case (i.e., $|Q + iU|_T$) where a true model of the beam is known. The spectra plots reported in the other plot, try to correct the columns that feeds into Stokes I (i.e., $Q \rightarrow I$, $U \rightarrow I$ and $I \rightarrow I$) by assuming the corresponding beams (i.e., m_{QI} , m_{UI} and m_{II}) are not known to the extent to which they have been assumed in this paper. In this case, the power spectrum of the HI signal can be observed at a multipole moment of $l = 25$. We conclude that if the knowledge of the beam is of a similar quality than the one assumed in this paper, then we will be able to recover the cosmological HI signal without great problems and without further calibration on scales larger than $l = 100$. However, this work suggests that if polarization calibration is performed correctly then results can be improved and we can recover scales above $l = 25$.

⁹<http://intensitymapping.physics.ox.ac.uk/CRIME.html>

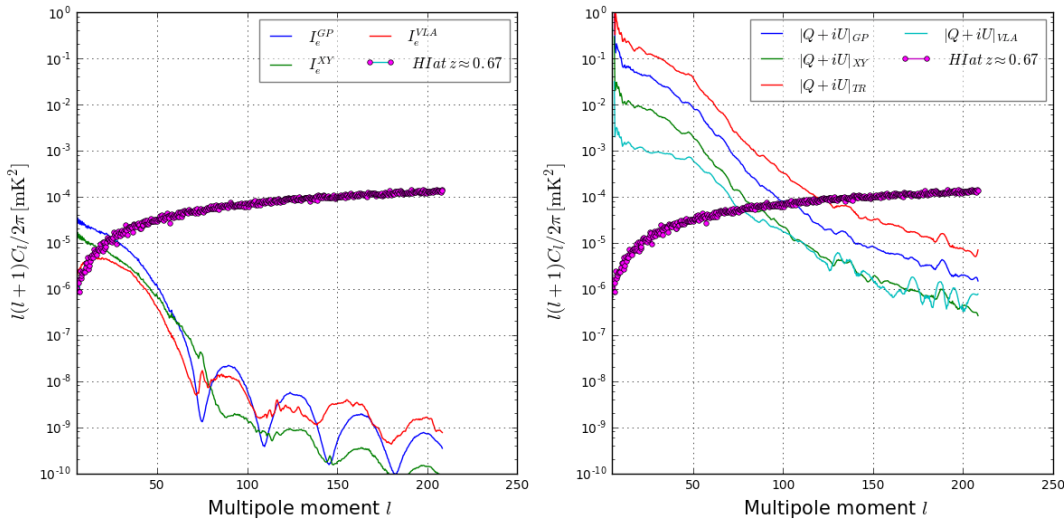


Figure 4.9: The spectra plots compare the effect of recovering the cosmological 21 cm signal by calibrating for the beam errors in Stokes I to when there is no beam correction at all. The solid circular spectrum is the simulated 21 cm brightness temperature described by [4] at a $z \approx 0.67$. LEFT SIDE PLOT: Here, we show how to estimate the 21 cm signal when we correct the errors in Stokes I . RIGHT SIDE PLOT: We quantify the amount of leakages into Stokes I when we do not perform any beam correction. The spectrum ($|Q + iU|_T$), is the intrinsic leakage in I when we adopt true modelled beams as shown in Fig. 4.4a. The other plots ($|Q + iU|_{GP}, |Q + iU|_{XY}, |Q + iU|_{VLA}$) are the leakages in I when we use perturbed modelled beams (i.e., gain, phase and main dish surface orientation errors) and holography measured beams respectively.

4.5 Conclusions

The study introduces an application of the OSKAR software as a relatively cheap technique to produce realistic PBs and perturbations (using gain, phase, and main dish surface orientation errors) for IM experiments. These fully polarized modelled beams are then used to simulate the full-sky polarization maps by the method of convolution in order to compute the intensities of the diffuse Galactic foregrounds and determine the amount of signal that has seeped from linear polarization into total intensity. The simulation is repeated using the holography-measured beams and then compared with the modelled beams in order to estimate the error introduced in the power spectrum when modelled beams are used. The following are the key findings of the research:

- We use 80000 dipoles to model the distribution of the dish-like surface of the antenna. This produces ≈ 0.10 per cent perturbed inaccuracies on the dish surface due to the random placement of the dipoles, which are not exactly phased up. The value of the perturbed inaccuracies will increase if the number of dipoles is $\ll 80000$.
- The perturbed inaccuracies due to the imperfections in the nominal orientation of the dipoles introduce fractional errors of 0.08% for Stokes I , 0.03% for Q and 0.07% for U in the convolved power spectrum estimation. Note that these occur when we assume to use modelled beams whilst we convolve the foregrounds with measured beams.
- Furthermore, if we construct a model of a beam and then carry out polarization rotation and calibration of the phase in order to correct the beam in Stokes I , then the power of the HI signal can be estimated at a multipole moment of $l = 25$. But, if we don't do any correction at all for the beam, then the power spectrum of the HI signal is measured at a multipole moment of $l = 100$. This makes the latter multipole moment be ≈ 4 orders of magnitude higher than when we correct the error in the beam.
- Finally, if a true model of the beam is assumed, then the intrinsic fractional leakage of $|Q + iU|_T \rightarrow I$ is ≈ 1.0 percent.

To recap, we have shown that the `oskar` package can simulate the beam patterns and as well as distortions of the dish. The model we adopted to do this, is to create a dense set of dipole orientations that imitate the aperture illumination patterns of the dish, with full blockage from the quad leg structure and other supporting frame. The convolution technique has shown to be a good mathematical model to use for measuring the intensity of the foreground. Hence, for a full polarization model of the beams, we can actually measure the fractional leakages we are interested in. For the next chapter, we extend this simulation technique to investigate HI intensity mapping with MeerKAT L-band beams.

Chapter 5

MeerKAT L-Band Primary Beams: Effects of HI Intensity Mapping

Overview

This chapter introduces us to the Zernike model and how it can be used to reconstruct a realistic beam model using the strongest coefficients (selected number of Zernike coefficients) with corresponding basis patterns. An intensity mapping experiment is performed with these primary beams to evaluate the angular power spectrum of 21 cm signal.

Author's comment: The primary beam model used in this chapter is part of the work in: K. M. B. Asad, J. N. Girard, M. de Villiers, **T. Ansah-Narh**, K. Iheanetu, O. Smirnov, M. G. Santos, and others, Primary Beam Effects of Radio Astronomy Antennas – II. Modelling the MeerKAT L-band Beam using Holography. The Monthly Notices of the Royal Astronomical Society (MNRAS), accepted. We therefore confirm that part of the wording in this chapter will “match” that of the paper. Hence, this note serves as a universal reference for all such text.

5.1 Introduction

The completely operational MeerKAT instrument is situated in Karoo (a desert area) of South Africa and, is made up of 64 ‘offset Gregorian’ interferometer. The measurement across the main dish is 13.5 m, that of the secondary reflector is 3.8 m and, has a maximum separation of 8 km. Almost 70% of the receptors are found in the core area of 1 km in width. The central location of the interferometer is at latitude $-30^{\circ}42'47.41''$ and longitude $21^{\circ}26'38.00''$. There are four feeds on each receptor with the L-band having a frequency range of 0.9 – 1.67 GHz. It also has digitisers supported on the feed indexer. The offset design of MeerKAT provides a better aperture efficiency, a symmetric beam pattern with a decrease in the side-lobes and an increase

in the antenna gain. The relatively small diameter of the MeerKAT antennas coupled with the large number of antennas and large total collecting makes it a powerful wide-field imaging instrument, with a combination of large field-of-view, wide-bandwidth, high sensitivity and outstanding sampling of the Fourier transform of the sky with 2016 instantaneous baseline samples.

Fig. 5.1 displays the station layout of the MeerKAT elements with the left panel showing the representation of the outermost layout and that of the right panel showing the innermost layout. Refer to [58, 74, 93, 101, 114] for further reading on the design of MeerKAT and its capabilities for science research.

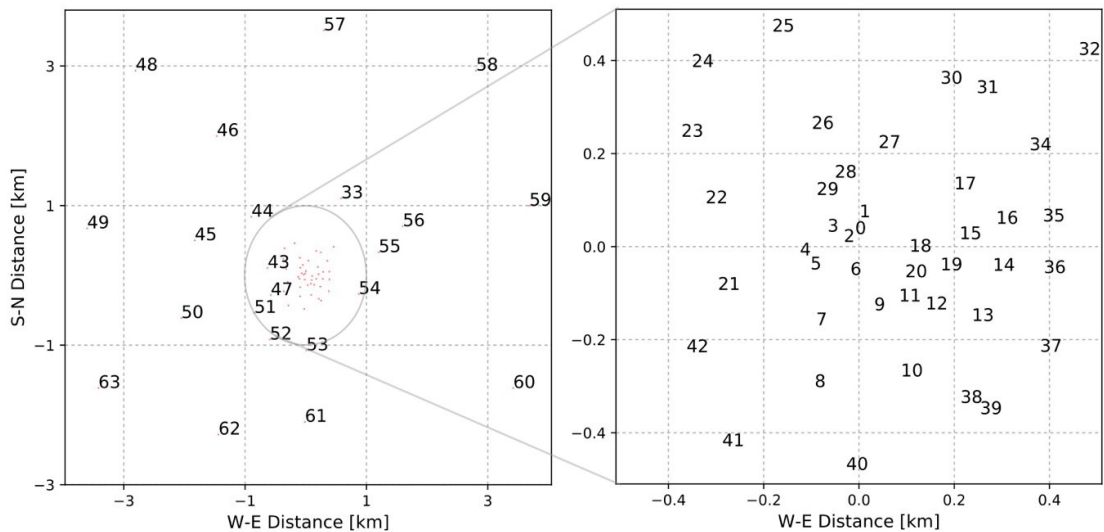


Figure 5.1: The distribution of the 64 antennas of MeerKAT, each identified by an integer ranging from 0 to 63. Note that the actual names of the antennas are given as M000, M001, M002 and so on. Left: The distribution outside the 1 km core. Right: The distribution inside the 1 km core is loosely delimited by a hexagonal boundary. The West-East and South-North distances are shown relative to the arbitrary centre located at $-30^{\circ}42'47.41''$ South, $21^{\circ}26'38.00''$ East.

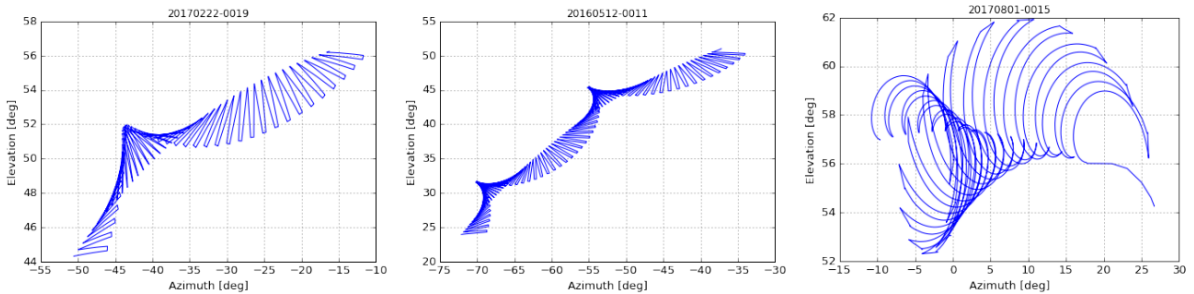


Figure 5.2: The raster scanning patterns of three of the astro-holographic observations of MeerKAT. The title indicates the observation ID. More information about the observations can be found in Table 1 and inside the text.

One major technique used in radio interferometry in order to measure the complex beam pattern of an antenna, is the holography. Generally, to produce a holography

beam model, one radio telescope points constantly at a cosmic radio source whilst another telescope drifts across the source, usually in a raster scan form. We then obtain the complex beam pattern in terms of amplitude and phase by correlating the respective output powers with the reference antenna pointing at the same source.

The main target source observed in this work is 3C 273 at a frequency of 1.365 GHz. In addition, Fig. 5.2 shows the patterns of the various raster scans used in this study. The 2017-02-22 observation was performed using three scanning antennas (M000, M012, M017) and one tracking antenna (M011). The scanning and tracking were performed from an elevation angle of $44^\circ \sim 57^\circ$, as seen in the figure, but we can also see that the beam is well-sampled within only a circular region of around $\sim 6^\circ$ diameter, centred at an elevation of 51.08° . The centre elevation is obtained from the average of the tracked elevations. The holographic measurement of this radio interferometer is discussed extensively in [134]. Here, the observation is done not directly using the traditional raster scan approach as presented in [36] but instead, a complex scanning pattern like the one displayed in Fig. 5.2. This method is efficient because it cuts out the need for slew scans in the traditional way, and hence reduces the tracking period. However, the complex beams produced from this scheme are perturbed with undesirable radio frequency interference (RFI). The source of this disturbing noise can be resolving satellites and other physical radio emissions. Therefore, it is necessary to introduce a mathematical model to reconstruct these holography measured beams which is the main objective of this research, in order to denoise the data and achieve a high accuracy. In the original paper, we demonstrated three different numerical techniques namely; modified-Principal Component Analysis (PCA), Spherical Harmonics (SH) and Zernike Moment (ZM) to model the measured beams. For the purpose of this study, we focus on ZM only. Here, we want to further explore how the IM techniques discussed in Chapter 4 scale to MeerKAT telescopes. Thus, instead of using OSKAR to simulate perturbed fully polarized beams, we fit Zernike polynomials to MeerKAT holography measured beams using a particular number of Zernike coefficients with corresponding basis functions and then perturb the beams with the fit again, using different number of coefficients. We then simulate these reconstructed beams with the foregrounds to determine the leakage terms.

The mathematical function of ZMs was originally developed to tackle wavefronts in optics. Now, the model has been adopted in many applications of image analysis such as image reconstruction [79], image classification [29, 61], and image retrieval [112]. The orthogonal property of ZMs can depict an image with arbitrary number of polynomials using the highest coefficients [115].

Next we present the mathematical model of ZM.

5.2 Methodology

5.2.1 Mathematical Basis of Zernike Polynomials

Consider a wavefront denoted by $\Phi_w(\rho, \theta)$, in polar coordinates (ρ, θ) , to be a linear combination of Zernike polynomials over a circular unit, then this phenomenon can mathematically be expressed as:

$$\Phi_w(\rho, \theta) = \sum_{\beta, \alpha}^M C_\beta^\alpha Z_\beta^\alpha(\rho, \theta) \quad (5.1)$$

The *basis of ZM* $Z_\beta^\alpha(\rho, \theta)$, in Equation 5.1 is defined as [39]:

$$Z_\beta^\alpha(\rho, \theta) = \begin{cases} \Lambda_\beta^\alpha R_\beta^{|\alpha|}(\rho) \cos(\rho\alpha\theta), & \alpha \geq 0 \\ -\Lambda_\beta^\alpha R_\beta^{|\alpha|}(\rho) \sin(\rho\alpha\theta), & \alpha < 0 \end{cases} \quad (5.2)$$

The *radial polynomial* $R_\beta^{|\alpha|}(\rho)$ and the *normalisation factor* Λ_β^α in Equation 5.2 are respectively denoted as:

$$R_\beta^{|\alpha|}(\rho) = \sum_{s=0}^{\frac{\beta-|\alpha|}{2}} \frac{(-1)^s (\beta-s)! \rho^{\beta-2s}}{s! \left[\frac{\beta+|\alpha|}{2} - s \right]! \left[\frac{\beta-|\alpha|}{2} - s \right]!}, \quad \Lambda_\beta^\alpha = \sqrt{\frac{2\beta+1}{1+\delta_{\alpha,0}}}$$

where $\delta_{\alpha,0}$ is the Kronecker delta function such that $\delta_{0,0} = 1$ and $\delta_{\alpha,0} = 0$ when $\alpha \neq 0$. The index $\beta \geq 0$: $\beta = 0, 1, 2, \dots$ and for a specific β , the index α takes the values $\alpha = -\beta, -\beta + 2, -\beta + 4, \dots, \beta$.

The polynomials $Z_\beta^\alpha(\rho, \theta)$ are a set of complete orthogonal over a unit circle and this is conveniently represented in Equation 5.2 as the products of angular functions and radial polynomials. The orthogonality of this function makes the coefficients not to be dependent on one another [28, 131] and hence, these coefficients are normally expressed in double (β, α) or single (j) modes. The β mode characterises the order of aberration and mode α represents the azimuthal frequency of the sinusoidal. The radius parameter, denoted ρ , is continuous over the range of $(0, 1)$ and this means the azimuthal component is continuous over the range of θ , such that $0 \leq \theta \leq 2\pi$. Fig. 5.3 displays 8 of such radial responses, where it can clearly be observed that the polynomials converge as they approach the edge of the unit disc. This also confirms that the Zernike polynomials of all orders are confined to the interval $(-1, 1)$ as shown in Fig. 5.4.

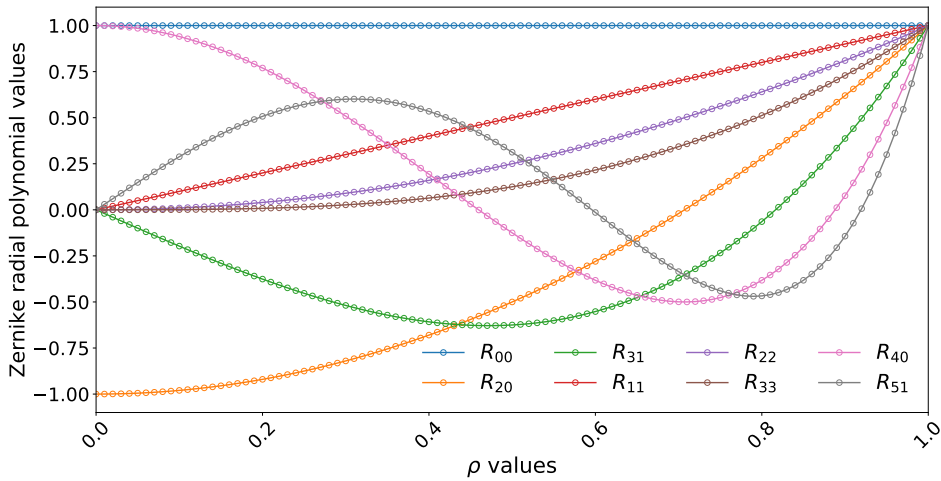


Figure 5.3: Expansion of eight orthogonal radial polynomial $R^{|\alpha|}(\rho)$ plots. Here, the value of unity can be obtained at the outer edge, since $R_\beta^{|\alpha|}(1) = 1$.

The surface plots in Fig. 5.4 depict the Zernike pyramid formed by the first 6 levels. In the central column, the modes are invariant by rotation (i.e. $\alpha = 0$) and hence, the column can be seen as a symmetry around the axis. On each level (i.e. same β value), the Zernike modes of opposite azimuthal frequency value have the same overall shape, but a different orientation. These pairs are required to enable any mode to be freely moved around 360° , by selectively adjusting the weight of each mode to obtain the desired orientation. Note, for further discussions on ZM, we can refer to these articles [21, 69, 78, 131].

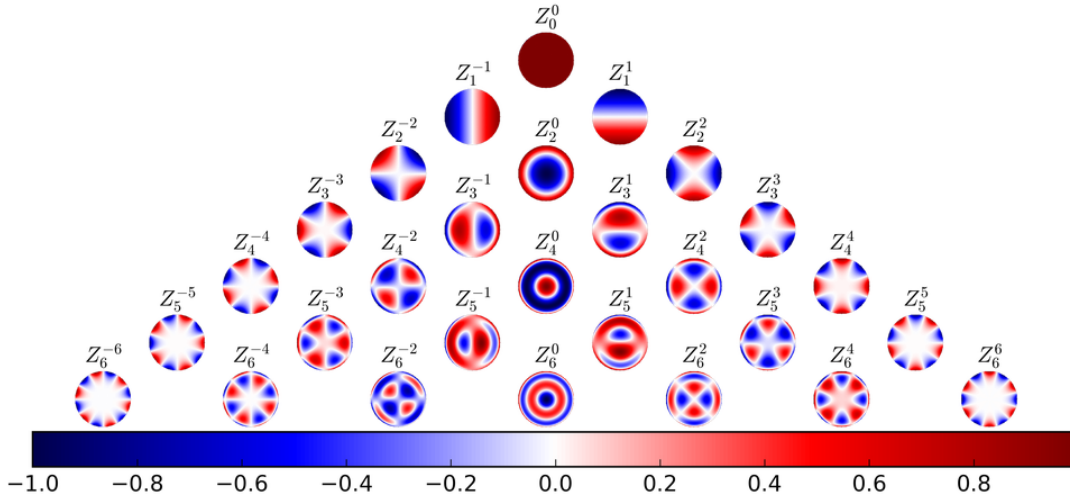


Figure 5.4: Representation of basis patterns of Zernike moments $Z_\beta^\alpha(\rho, \theta)$ of order 6, plotted on a unit circle.

5.2.2 Numerical Computation of Zernike Coefficients

In Equation 5.1, the vector variable C_β^α (Zernike coefficient) is the only unknown factor that needs to be computed. Let L denote the pixel positions of the measured beam Φ_w , such that $\Phi_w^\tau(\rho_\tau, \theta_\tau) |_{\tau=1,2,3,\dots,L}$, where (ρ_τ, θ_τ) is the corresponding pixel coordinate usually in polar form. We then estimate the parameter C_β^α by rewriting Equation 5.1 in a simple form as expressed in Equation 5.3 and then try to solve the least square problem using the matrix inversion approach.

$$\mathbf{Z}_{P \times L} \mathbf{C}_{P \times 1} = \Phi_{L \times 1} \quad (5.3)$$

where Φ is the $L \times 1$ data array¹ that consists of the MeerKAT beams, \mathbf{C} is the unknown coefficients of $P \times 1$ array and \mathbf{Z} is the $P \times L$ matrix of polynomials that provides the physical features of Φ . Expanding Equation 5.3 we get;

$$\begin{pmatrix} Z_1(\rho_1, \theta_1) & Z_2(\rho_1, \theta_1) & \cdots & Z_P(\rho_1, \theta_1) \\ Z_1(\rho_2, \theta_2) & Z_2(\rho_2, \theta_2) & \cdots & Z_P(\rho_2, \theta_2) \\ \vdots & \vdots & \ddots & \vdots \\ Z_1(\rho_L, \theta_L) & Z_2(\rho_L, \theta_L) & \cdots & Z_P(\rho_L, \theta_L) \end{pmatrix} \begin{pmatrix} c_1 \\ c_2 \\ \vdots \\ c_L \end{pmatrix} = \begin{pmatrix} \Phi(\rho_1, \theta_1) \\ \Phi(\rho_2, \theta_2) \\ \vdots \\ \Phi(\rho_L, \theta_L) \end{pmatrix} \quad (5.4)$$

The resultant equation can be written in the form:

$$\mathbf{Z}^T \mathbf{Z} \mathbf{C} = \mathbf{Z}^T \Phi \quad (5.5)$$

such that, the desired Zernike coefficients can be obtained by direct inversion;

$$\mathbf{C} = (\mathbf{Z}^T \mathbf{Z})^{-1} \mathbf{Z}^T \Phi \quad (5.6)$$

¹The package `numpy.ravel` will return a neighbouring flattened array.

Therefore, given the basis patterns of Zernike polynomials and the corresponding coefficients, we can use these to reconstruct a particular wavefront. In this study, the MeerKAT holography primary beams are used to represent the wavefront and then fit Zernike polynomials to reconstruct the measured beams.

5.2.3 Spatial Representation

Note here that we represent the MeerKAT beams in the Jones matrix form as \mathbf{XX}^2 , \mathbf{XY}^3 , \mathbf{YX}^4 , \mathbf{YY}^5 . Therefore, these notations have the same meaning through out this chapter.

In this work, we select the strongest coefficient values to denoise the MeerKAT beams at 990 MHz. The selection is done base on the modal number with a reduced value of root mean square deviation (RMSD: $[1/N \sum_{k=1}^N \| \mathbf{D}_k^a - \mathbf{D}_k^e \|^2]^1/2$ where N is the beam size, \mathbf{D}_k^e is the Zernike fitted beam and \mathbf{D}_k^a is the original beam) as reported in Fig. 5.5. The RMSD plots of XX and YY in Fig. 5.5 (blue and red) show that, we can use 20 strongest angular frequencies (m-modes) with $RSMD \approx 0.001$ to model the gain part of the original holography beams, since increasing the number of m-modes will not significantly improve the reconstructed model. The same explanation goes to the cross term plots (yellow and green), where we choose the 5 strongest modes with $RSMD \approx 0.001$ and the respective coefficients to reconstruct.

The principal idea to adopt the Zernike scheme in this study is to decrease the number of feature parameters (i.e. Zernike basis functions) required to depict the spatial morphology since generally, Zernike coefficients are highly sparse. If we use a smaller number of coefficients, there's the possibility that the modelled image will not be well-fitted. In addition, if the number of coefficients is very high, there's the likelihood of over-fitting the modelled image. In this research, we cautiously choose the strongest number of coefficients by truncating the coefficients up to a given threshold parameter based on the RMSD value.

²Horizontal linearly unpolarized beam

³Horizontal linearly polarized beam

⁴Vertical linearly polarized beam

⁵Vertical linearly unpolarized beam

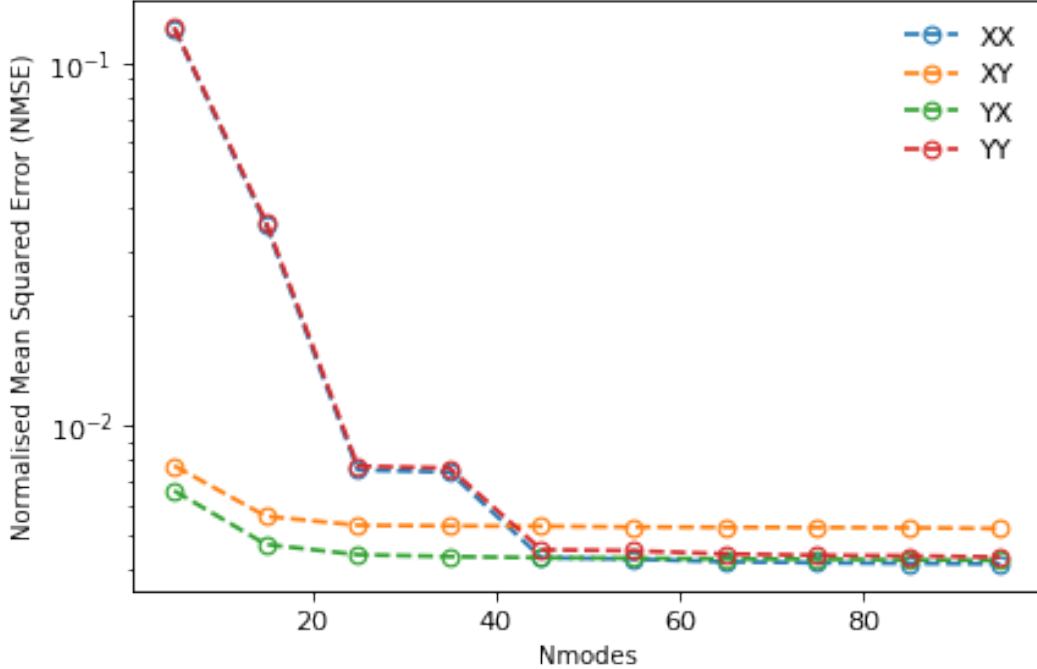


Figure 5.5: The expected value of the squared error loss between the holography beam and the predicted beam model with respect to increase in the number of Zernike modes. (XX, YY) and (XY,YX) are the linear polarization for the gain and cross terms of the Jones beams respectively.

We use this idea to reconstruct a 2D image from a Zernike fit. Here, all we need to have are the coefficients and the respective basis functions. Fig. 5.6 shows a reconstructed MeerKAT beam model at a frequency of 990 MHz for antenna M017. Note how the Zernike modelled beams (middle plots) have de-noised the original beams. To test the goodness of fit of this model, we vary the number of Zernike coefficients and compare their residuals. The 1st 2 plots in Fig. 5.7 are the radial profile plots when we use the 5 strongest coefficients for all the Jones terms and the 10 strongest coefficients for all the Jones terms respectively. Note how the standard errors of these plots are higher than the 3rd plots which occur when we use the coefficients of 20 and 5 for the gain and cross terms respectively. This is confirmed when we also look at the distribution of the histogram plots in Fig. 5.8. Using > 5 strongest coefficients to model the cross terms and < 20 strongest coefficients to model the gain terms will result in the perturbation of the beams.

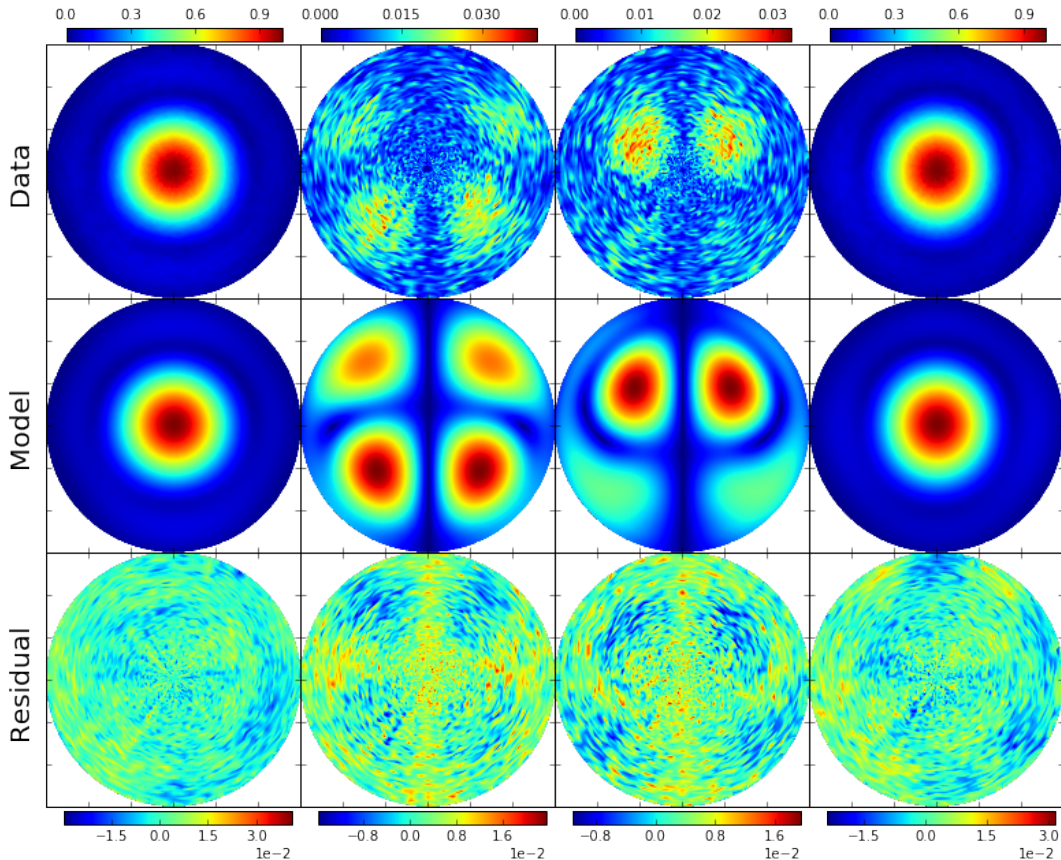


Figure 5.6: Zernike reconstructed MeerKAT beam model at 990 MHz, using 20 and 5 strongest coefficients to model the gain and cross components respectively. The first and fourth columns are the amplitude beams of XX and YY respectively whilst the beams in the second and third columns are XY and YX correspondingly.

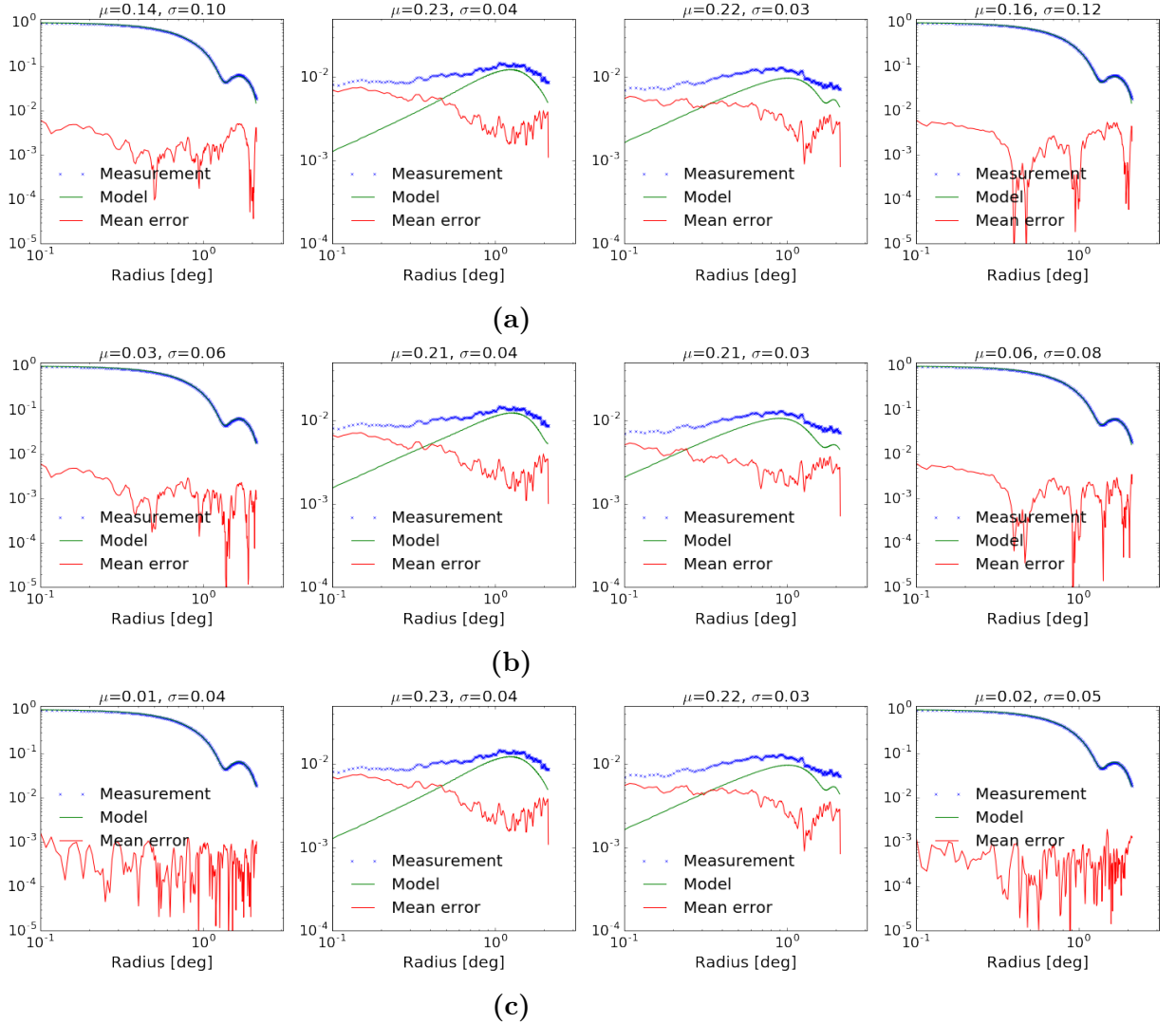


Figure 5.7: Radial profile of Fig. 5.6. (a) Using 5 strongest Zernike coefficients for the Jones components. (b) Using 10 strongest Zernike coefficients for the Jones components. (c) Using 20 strongest Zernike coefficients for the gain components and 10 strongest Zernike coefficients for the cross components.

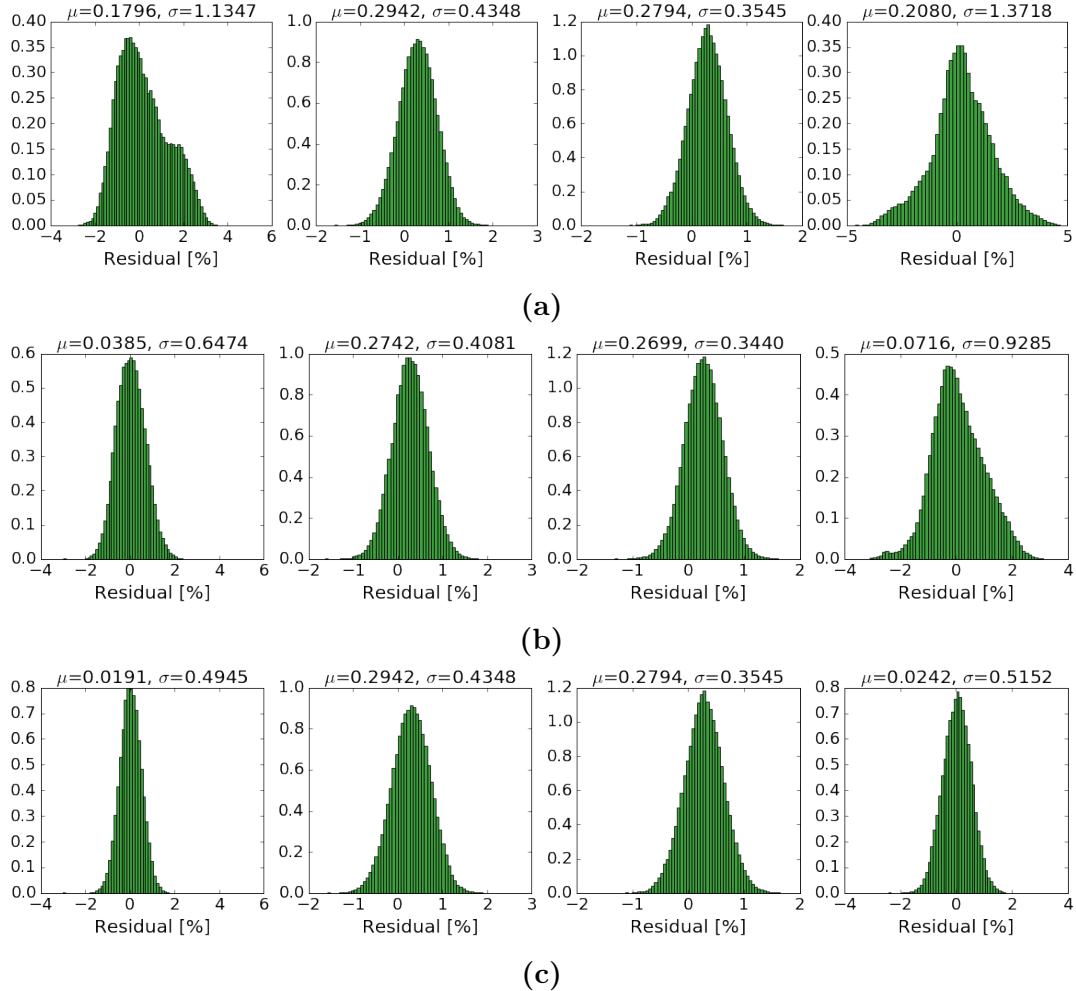


Figure 5.8: Histogram plots showing the residual distribution. (a) Plots obtained from using 10 strongest Zernike coefficients for the Jones components. (b) Plots obtained from using 10 strongest Zernike coefficients for the Jones components. (c) Plots obtained from using 20 strongest Zernike coefficients for the gain components and 10 strongest Zernike coefficients for the cross components.

Next, we discuss how we reconstructed missing channels of the holography beams, using the DCT ‘Discrete Cosine Transform’ approach.

5.2.4 Spectral Representation

Most of the MeerKAT beams in the L-band are highly corrupted by RFI. The extremely damaged channels are within the following ranges;

$[(920, 960), (1125, 1305), (1463, 1492), (1520, 1630)]$ MHz. We discard the measurements in these patches, and reconstruct the coefficients therein by interpolation from the surrounding unaffected channels. The spectral interpolation and compression are done simultaneously using Discrete Cosine Transform (DCT) for the amplitudes $A(\nu) = |C(\nu)|$ of the complex coefficients, and a three-parameter sine wave for the sines and cosines of the corresponding phases $\phi(\nu) = \tan^{-1}[\text{Im}(C)/\text{Re}(C)]$. We found the amplitude and phase to be the more natural parameters to model in case of linear

polarization feeds, such as that of MeerKAT, as opposed to circular polarization feeds, e.g. that of VLA, where modelling the real and imaginary parts of the coefficients, in frequency, seemed to be more appropriate.

In this work, we compute the amplitude of the coefficients by packing the damaged parts mentioned above with temporary values which is linearly interpolated from the uncorrupted nearby channels. We can easily do this by using the ‘`numpy.interp`’ Python package.

The interpolated amplitudes $A(\nu)$ are then decomposed using DCT (of Type II) as

$$A_k = \frac{2}{\sqrt{wN_\nu}} \sum_{n=0}^{N_\nu-1} A_n(\nu) \cos \left[\frac{\pi k(2n+1)}{2N_\nu} \right] \quad (5.7)$$

for $0 \leq k < N_\nu$ where $w = 4$ when $k = 0$ and $w = 2$ otherwise. Subsequently, we select the strongest N^d DCT coefficients and put the rest to zero resulting in the sorted coefficients A' which, in turn, are used to reconstruct a smooth spectral model of the amplitudes by Inverse DCT (same as DCT of Type III) as

$$\hat{A}_n(\nu) = \frac{A'_0}{N_\nu} + \sqrt{\frac{2}{N_\nu}} + \sum_{n=0}^{N_\nu-1} A'_k \cos \left[\frac{\pi n}{N_\nu} (n + 1/2) \right] \quad (5.8)$$

for $0 \leq n < N_\nu$.

The spectral profile in Fig. 5.9 displays the amplitude of the Zernike coefficients where the dense dotted points are the fitted beams with missing channels whilst the thin dotted lines are the interpolated beams obtained from $\hat{A}_n(\nu)$ in Equation 5.8. The bad channels (missing gaps) in the plots are represented as light-gray vertical dashes. Here, we show in the descending order the strongest coefficients and the corresponding activated basis patterns that are unique in the reconstruction of all the channels (from [856, 1700] MHz). The plots in Fig. 5.9a represent the amplitude component of the horizontal linearly unpolarized beam (XX) of the Jones elements (usually referred to as the gain term) whilst Fig. 5.9b represent the cross term (XY) of the Jones elements. The thick-gray dashes in Fig. 5.9a are fiducial markings used to distinguish the activated basis functions whose coefficients are above $\sim 10\%$. In our case, these are Z_2^0, Z_4^0 and Z_6^0 , and can be located at the principal axis of Fig. 5.4. Their official names in [69] are defocus (Z_2^0), 1st spherical (Z_4^0) and 2nd spherical (Z_6^0). Note that these basis functions are activated because we can observe from the plots that the ripple effect in the MeerKAT beams (XX) looks more stable across all frequencies, but this is not always the case for all antennas as we shall witness this change effect in SKA1-mid beams in the next chapter. On the other hand, the strongest basis patterns used in Fig. 5.9b are $Z_4^{-2}, Z_7^{-1}, Z_6^{-2}, Z_2^{-2}, Z_8^{-2}$ and Z_5^{-1} which are mostly composed of Zernike functions such as astigmatism ($Z_4^{-2}, Z_6^{-2}, Z_2^{-2}, Z_8^{-2}$) and coma (Z_7^{-1}, Z_5^{-1}). These patterns are well defined for the representation of the solid cloverleaf patterns in the cross terms (XY) of MeerKAT beams. Note that the basis patterns in Fig. 5.9 are the same for the other components in the Jones matrix,

thus, the component YY can be modelled with other patterns in Fig. 5.9a and YX uses the Zernike functions in Fig. 5.9b. The MSE plots in Fig. 5.5 confirm this too.

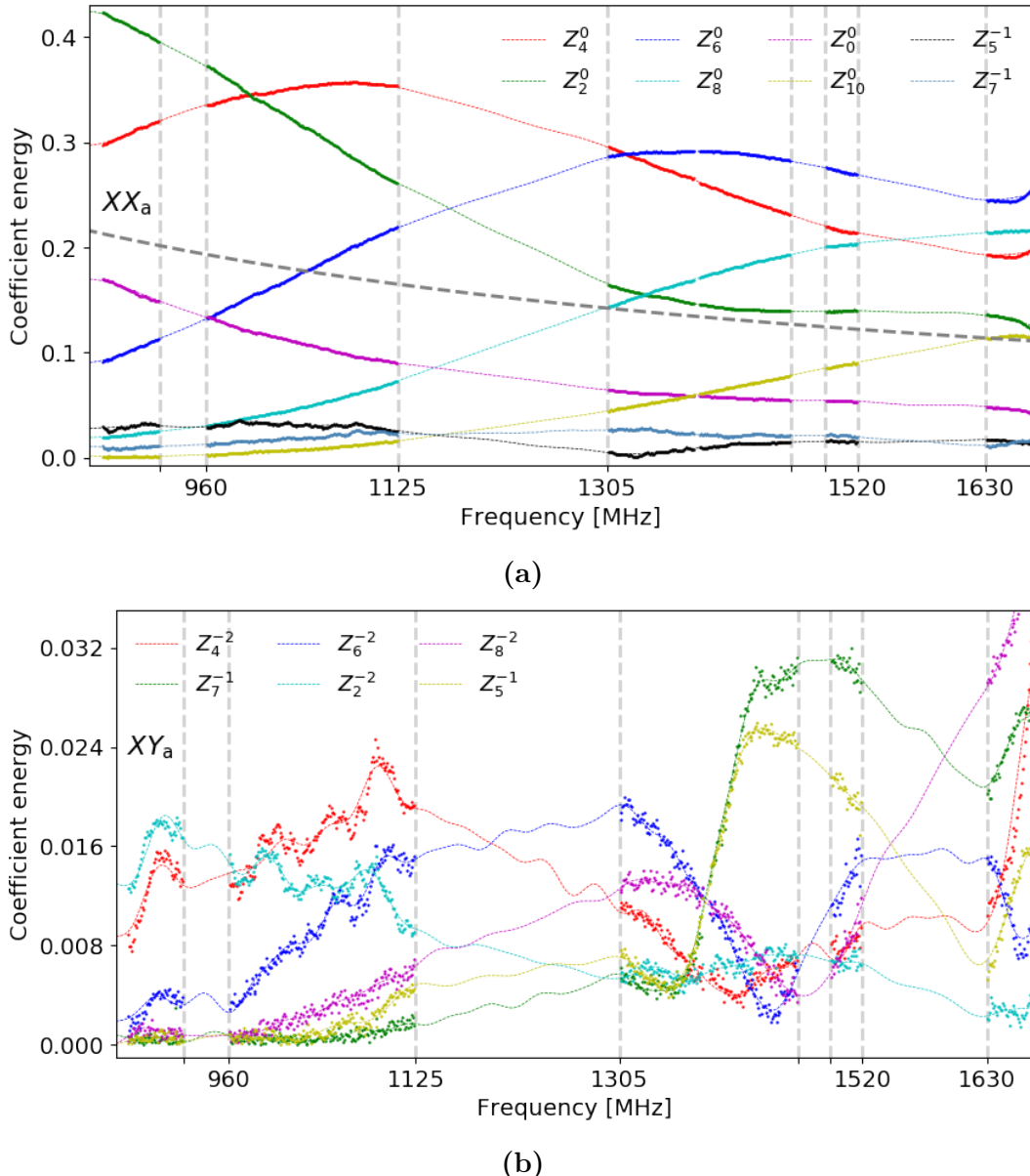


Figure 5.9: Spectral representation of the amplitude of MeerKAT primary beams for L band. The light-gray vertical dashes are the missing gaps due to high RFI whilst the thin dotted lines are the DCT plots used to correct the bad channels for the respective Jones terms [XX (top) and XY (down)].

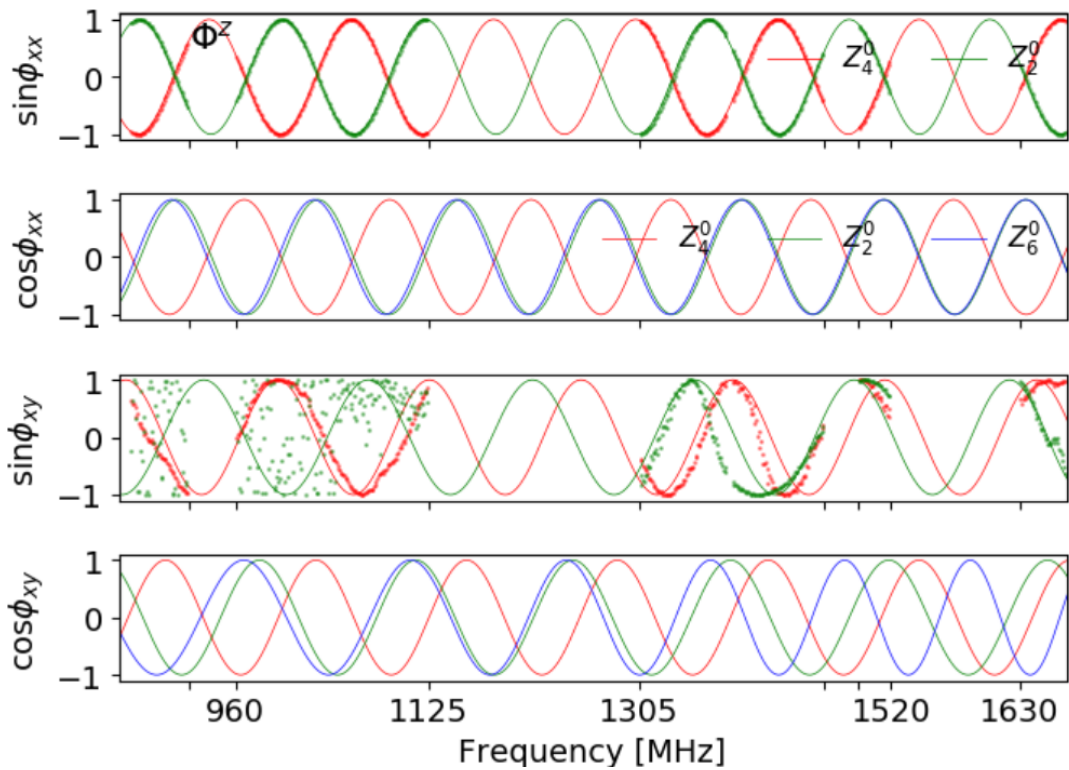


Figure 5.10: Spectral representation of the phase of MeerKAT primary beams for L band. The thick dotted lines are the Zernike plots with missing frequency channels due to high RFI whilst the solid lines are the Sine and Cosine plots used to correct the bad channels for the phase terms of XX and XY.

In addition, we apply the sine wave with parameters α, β and γ to model the beam phase:

$$\zeta(v) = \sin(2\pi\frac{\nu}{\alpha} + \beta \cos 2\pi\frac{\nu}{\gamma}) \quad (5.9)$$

Therefore, using the ‘`lmfit.minimize`’ Python package with the Nelder-Mead method, we can then fit $\zeta(v)$ to $\sin \phi(\nu)$ and $\cos \phi(\nu)$ to obtain the plots in Fig. 5.10. Here, the missing channels are reconstructed by taking the Sine and Cosine of the imaginary and real parts of the Jones terms accordingly. Note how the Sine and Cosine functions actually predicted the Zernike coefficients for the phase beams of XX. Nevertheless, we obtained some deviations for the imaginary part of the cross term (XY) even though the real part actually predicted the missing gaps correctly.

We now discuss the results obtained when we simulate the foregrounds with the above modelled beams to compute the polarization leakage when performing an IM experiment.

5.3 Results and Discussion

The convolved maps presented in Fig. 5.11 are a repetition of the simulation we discussed in Section 4.3. Here the reconstructed MeerKAT primary beams are transformed from the Jones terms into complete Mueller beams. These Mueller beams are then used to convolve the foregrounds maps in Fig. 3.6. The 1st row is the true measured maps when the modelled beams used are constructed with 20 and 10 strongest coefficients for the gain and cross terms respectively. The next 2 rows are the perturbed measured maps when we fully model the beams with 5 and 10 Zernike coefficients in a respective manner. The remaining rows are the residual maps between the true and the perturbed measured maps. Note carefully how these scaled measured maps (both true and perturbed) are very similar but the actual differences are shown in the error maps.

The spectra plots displayed in Fig. 5.12 show how the HI signal power is estimated when we correct the errors in the reconstructed beams and vice versa. If the errors in the reconstructed beams are corrected in Stokes I as shown in the left plot, then the HI signal power is estimated at a multipole moment of $l \simeq 25$ and if the error is not corrected at all in Stokes I but the intrinsic polarization leakage ($|Q + iU|_z$) in I is known, then the HI signal power is estimated at a multipole moment of $l \simeq 100$. This multipole moment is about 4 orders of magnitude greater than the foreground at lower scales. However, if the intrinsic $|Q + iU|_z \rightarrow I$ is corrected, then the HI signal power is evaluated at a multipole moment of $l \simeq 50$. This multipole moment is about 2 orders of magnitude greater than the foreground at lower scales.

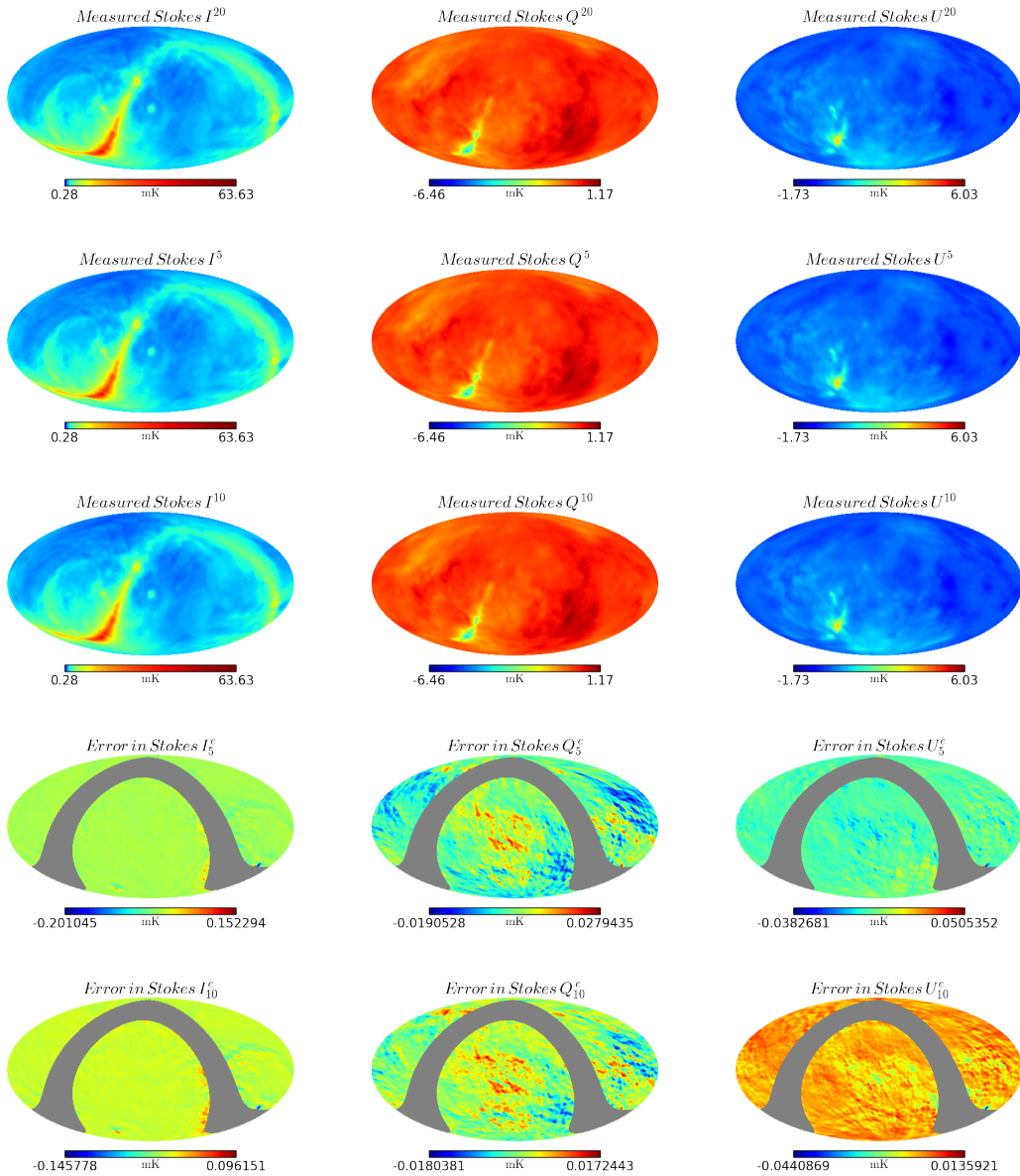


Figure 5.11: Measured Stokes I, Q and U convolved with reconstructed MeerKAT beam models with corresponding error maps. 1st row: These are maps convolved with Zernike beams with 20 highest coefficients. 2nd row: These are maps convolved with Zernike beams with 5 highest coefficients. 3rd row: These are maps convolved with Zernike beams with 10 highest coefficients. The 4th and 5th rows are the corresponding residual maps between the 1st and 2nd rows and between the 1st and 3rd rows.

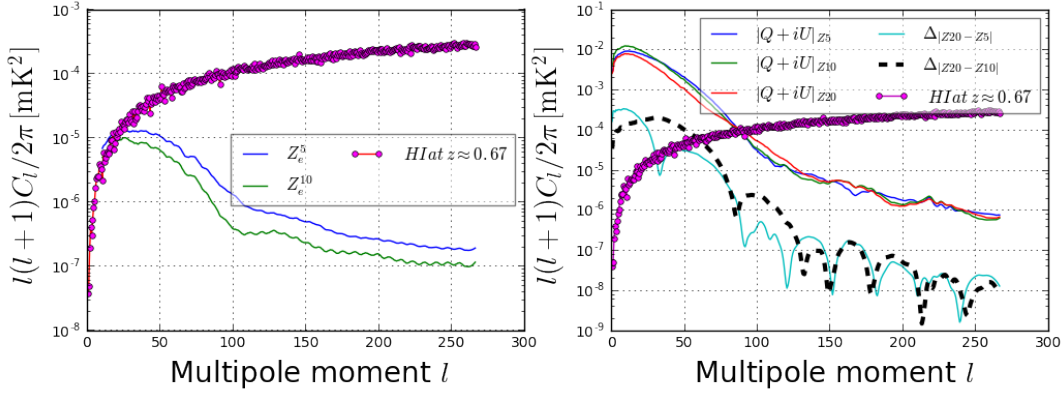


Figure 5.12: The distribution of angular power plots displaying the errors due to perturbed Zernike fits in Stokes I map (left plots) and the intrinsic leakage in I (right plots) affect the 21 cm signal (solid circular spectrum plot).

5.4 Conclusion

In this chapter, we have clearly shown that the Zernike decomposition is a very well-fitted model for IM experiments. The model was able to reconstruct the MeerKAT L-band holography measured beams. The reconstruction of the true modelled beam was done by using the strongest Zernike coefficients and the corresponding basis functions. In order to distort the true modelled beams, the study used more and less strong Zernike coefficients with the respective basis functions to perturb the modelled beams. In addition, to measure the HI signal power spectrum, the study performed an IM experiment by convolving these modelled beams with the foregrounds of the sky. The following are the key outcomes in this research:

- The true modelled beams were reconstructed with 20 strongest Zernike coefficients for the gain terms of the Jones matrix (XX and YY) and 5 strongest coefficients for the cross terms of the Jones matrix (XY and YX). The maximum standard error obtained from the reconstruction is $\simeq 0.05$.
- The corrupted modelled beams were generated with 5 strongest coefficients for all the Jones matrix terms (XX, XY, YX and YY). The second distortion was done with 10 strongest coefficients for all the Jones matrix terms (XX, XY, YX and YY). The maximum standard errors obtained are 0.12 (for using 10 strongest coefficients) and 0.08 (for using 10 strongest coefficients).
- The astigmatism and coma Zernike functions turn out to have the strongest coefficients to model the cloverleaf nature for the cross terms (XY, YX) of MeerKAT beams whilst the piston and spherical basis functions prove to be the best model for the gain terms (XX, YY).
- The HI signal power is measured at a multipole moment of $l \simeq 25$ if we correct the beam errors in Stokes I and at a multipole moment of $l \simeq 100$ if we do not correct the beam errors in I .

In summary, the primary beam is critical in IM experiments and therefore, the plots in Fig. 5.5 have shown that we can decompose the beams with an arbitrary number of Zernike polynomials but then we must select the highest coefficients up to a given threshold parameter based on the RMSD value. Hence, with a good Zernike model of the primary beams, we can actually measure the amount of foregrounds that have leaked from intensity into polarization.

Chapter 6

SKA1-mid Multiband Primary Beams: Effects of HI and CO Intensity Mapping Experiments

Overview

This Chapter introduces us to the SKA1-mid instrument and describes how we generate the beam patterns of Bands 1, 2 and 5 using the GRASP software package. Zernike models of these beams for the various bands are produced and used to investigate the effects of CO and HI intensity mapping.

6.1 Introduction

SKA1-mid is currently being assembled in South Africa and forms part of the three interferometric array of the SKA [103, 68, 120]. The instrument is designed to have 197 parabolic dishes (with 64 MeerKAT dishes inclusive) and a maximum baseline of 150 km. The feed design of the dishes will be a single-pixel with a total number of 254 [120] and it will have the ability to capture signals within five different bands between 0.35 GHz to 13.8 GHz. The design topology of this instrument is to have ~ 1 km diameter of dense inner elements and a randomly dispersed offset dishes in a spiral shape as shown in Fig. 6.1. Refer to [102] to understand the technical details in Fig. 6.1.

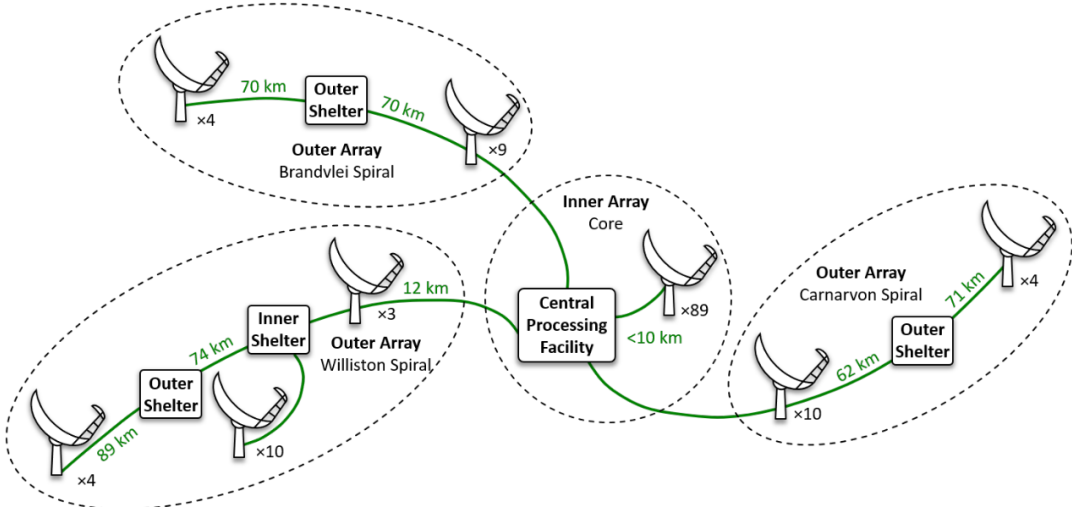


Figure 6.1: “Layout of the planned SKA1-MID telescope showing the locations of the antennas in the core and in the three spiral arms” (Fig. 6.1 and the caption are obtained from [102]).

“This telescope will primarily address observations of radio pulsars and observations of the 21 cm hyperfine line of neutral hydrogen from the local Universe, to moderate redshifts, as well as high sensitivity observations of continuum emitting objects. It will also be well suited for conducting observations of various spectral lines in addition to the 21-cm hydrogen line (e.g. OH-lines), many classes of radio transients, magnetized plasmas both in the Galaxy and intergalactic space, and potentially protoplanetary disks” [33].

Although this instrument is not exclusively designed for IM experiments, it will be good to investigate its potential for this technique, especially for Bands 1, 2 and 5 receivers which fall within the permitted budget of SKA1-mid. For further details on the description and classification of SKA1 system refer to [25, 33].

Here, we investigate the IM of CO line (for high redshift) in addition to HI at low redshift, particularly focusing on the observational effects of primary beam distortion of the SKA1-mid for Band 1 (i.e. 350 – 1050 MHz), Band 2 (i.e. 950 – 1760 MHz), Band 5a (i.e. 4.5 – 8.4 GHz) and Band 5b (i.e. 8.4 – 13.6 GHz). CO is a powerful tool to detect atomic gas and star formation in immediate galaxies and also, the most dominant molecular species after H₂.

Next, we describe how we use the EM simulator to produce the primarily beams of SKA1-mid.

6.2 GRASP Beam Measurement

GRASP software is a commercial package used to design and analyse single and dual reflector telescopes as well as multi-reflector and multi-feed antennas. This section concentrates on the physical geometry and EM methods applied for the SKA1-mid analysis. A complete description of the package with mathematical expressions of the

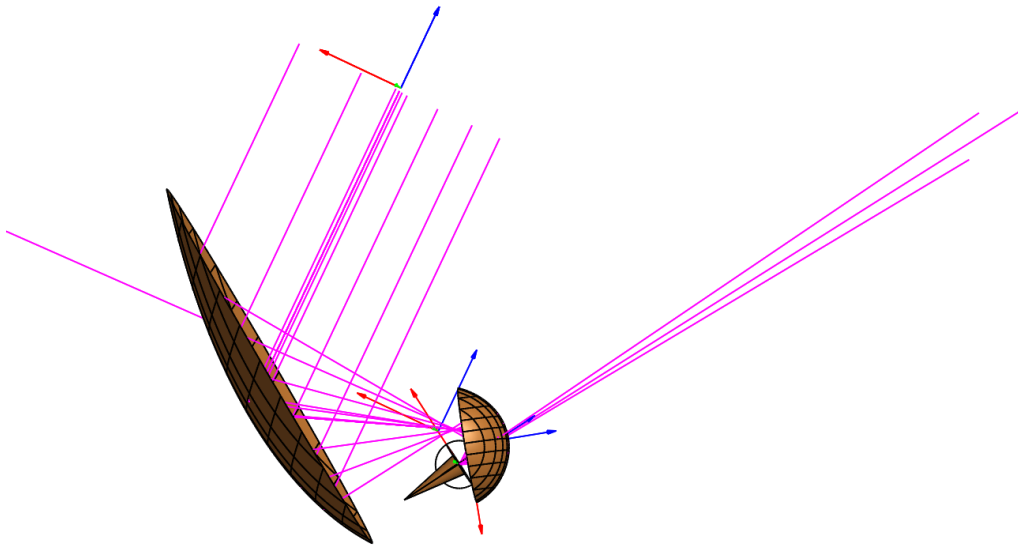


Figure 6.2: A geometrical dual reflector model of SKA1-mid oriented in the xz -direction and generating highly contoured beam.

geometries and EM models as well as output data capabilities is given in the GRASP Technical Description, which may be retrieved from the Help Menu.

6.2.1 Model Specification

Here, we setup the actual geometry of the instrument.

6.2.1.1 Reflector Antenna Models

Fig. 6.2 illustrates the dual reflector design of SKA1-mid. It includes an offset paraboloidal main reflector and a sub-reflector, with the principal focus hosting the receiver. Note how the receiving rays bounce off from the main dish to the secondary reflector and then finally go into the feed. This can be achieved by manually defining the following parameters:

- focal length of the reflector;
- angle between the axis of the primary reflector and the sub-reflector;
- focal distance for the sub-reflector;
- eccentricity for the sub-reflector;
- angle between the axis of the secondary reflector and the feed;
- aperture diameter of the main reflector;

- the wavelength of the operating frequency.

6.2.1.2 Feed Models

The feed system used in this chapter is an aperture illumination of the antenna system and this is possible in a receiver situation. A general way to represent the illumination from a feed is through tabulated data from its beam pattern, which may come from measurements or calculations. The beam pattern of the feed used in the analysis is the measured far-field pattern, which consists of received fields in θ, ϕ – plane (θ, ϕ define the field point on a sphere).

6.3 Modelling EM Beams

The GRASP software used to produce the EM beams considers the basis of physical optics (PO) together with the physical theory of diffraction (PTD). The simulations are made for Bands 1, 2 and 5. For the purpose of this work, we present a 2D grid for the simulated beams at 450 MHz, 990.5 MHz and 4.6 GHz as shown in the first rows of Figs. 6.4, 6.5 and 6.6 independently. These beams are presented in the Jones matrix (XX^1 , XY^2 , YX^3 , YY^4) and we can clearly observe from the gain components (XX and YY) that at lower frequencies particularly, for Band 1, we have a wider field-of-view (with less or no side-lobes) as compared to higher frequencies (with more side-lobes) as that of Band 5. Generally, in all parabolic reflectors, observing at higher frequencies produce narrower beam widths and therefore, it is just obvious that the Band 5 beam widths are much narrower than the lower bands (1 and 2). Nevertheless, such a beam width entails specifically, accurate dish surface regularity along with strong pointing accuracy. Understanding this primary beam effect is very significant in IM experiment since the technique involves multiple pointing in the sky in order to estimate the total intensity.

With the aim of investigating IM experiment with the SKA1-mid, we try to model the simulated beams, using Zernike polynomials (ZP) discussed in Chapter 5. After that, we introduce errors in the physical geometry of the instrument and finally, use these beams to simulate the foreground examined in Chapter 3.

6.3.1 Fitting 2D Zernike Polynomials on EM Beams

The mathematical basis of ZP is discussed extensively in Chapter 5. In this section, we repeat the same approach, using the appropriate radial order to reconstruct the beams to display both the spatial and spectral representations of the EM beams.

¹Horizontal linearly unpolarized beam

²Horizontal linearly polarized beam

³Vertical linearly polarized beam

⁴Vertical linearly unpolarized beam

6.3.1.1 Spatial Representation

The reproduction of the EM beams for channels 450 MHz, 990.5 MHz and 13.6 GHz, depend on the upper limit of Zernike modes (angular frequencies) to use. This maximum number defines the strongest modes necessary for extracting features from the simulated beams. Fig. 6.3 shows the mean square error (MSE) plots needed to choose the maximum number of modes⁵. For instance, to reconstruct the unpolarized components (XX and YY) of the beams at 450 MHz, we choose an upper limit of 56 modes as shown in Fig. 6.3a (blue plot). The same number of modes is selected (refer to Fig. 6.3b (blue plot)) if we want the basis functions to model the cross terms (XY and YX). Note that these 56 modes of ZP are obtained from an n-order (radial index) of 10. Similarly, taking the beams at the next two channels (990.5 MHz and 13.6 GHz), we select 100 modes (orange plot) and 150 modes (green plot) in Fig. 6.3a to model the diagonal parts. After that, we select the same number of modes (100 and 150) in Fig. 6.3b to describe the cross terms. These MSE plots, clearly show that if we increase the number of modes other than what we have chosen, there would not be any significant variation in the reconstructed beams.

Next, the corresponding coefficients can be computed, using Equation 5.6. Now, having the strongest coefficients (C_k) and the strongest basis functions (η_k), we reconstruct the simulated beams (R_Φ) as:

$$R_\Phi = \sum_{k=0}^{N^m} C_k \eta_k \quad (6.1)$$

⁵Nmodes is computed as $n + 1 + \sum range(n + 1)$, n is the radial order.

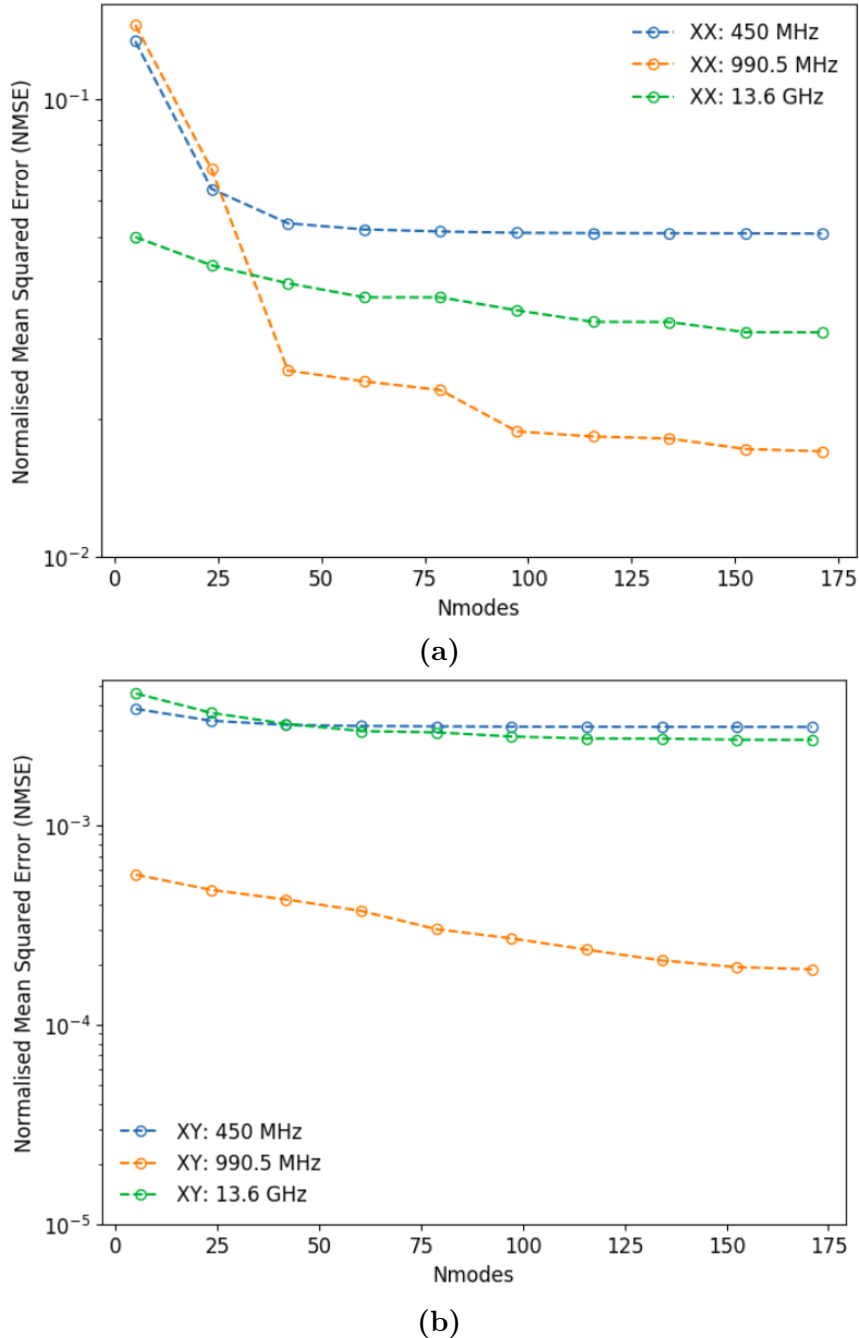


Figure 6.3: Representation of MSE for using the number of ZP at 450 MHz (blue), 990.5 MHz (orange) and 13.6 GHz (green). Panel (a) shows the gain term (XX) for each channel band whilst Panel (b) displays the cross term (XY).

The second rows in Figs. 6.4, 6.5 and 6.6 show the Zernike beam models of \mathbf{R}_Φ for Bands 1, 2 and 5 respectively. These restored images clearly show that the Jones elements XX and YY can be represented using almost the same modes due to the similarities of the power coefficients in both cases. Similar explanations go for the off-diagonal elements. Moreover, the high number of modes used in the Band 5 channel is due to the increase in the number of sidelobes. Note that an increase in the number of modes brings about a high radial order which is very important to model high sidelobes like in the case of Band 5. Nevertheless, at lower frequencies, less or no side-lobes will be present within the same region, and hence, lower orders will dominate the model like in the case of Band 1 and to some extend the lower channels of Band 2.

After the reconstruction, the residual value obtained in the gain terms is $\approx 1\%$ (for Bands 1, 2 and 5) and the cross terms, we have $\approx 0.01\%$ (for Bands 1, 2 and 5), showing that the proposed mathematical model in this case ZP, is good to consider when modelling beam patterns.

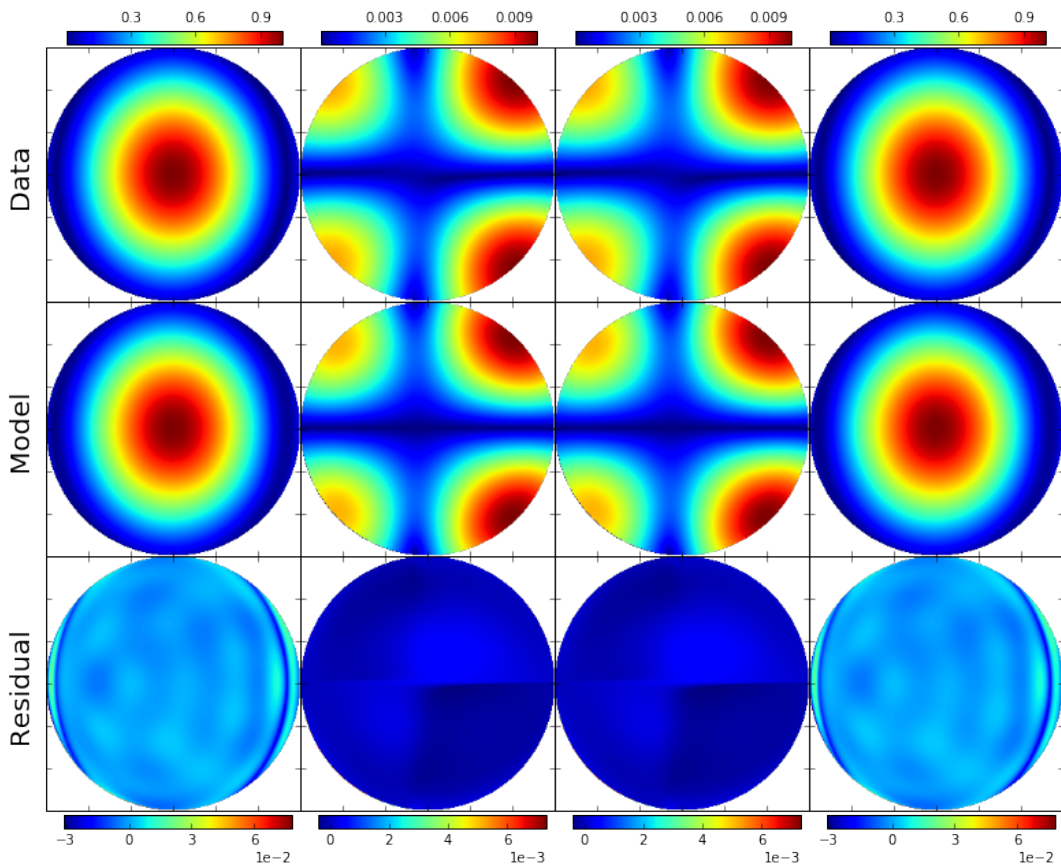


Figure 6.4: Top Row: Simulated EM model of SKA1-mid beam (in amplitude form) with a diameter of 6° at 450 MHz in a normalised unit. Middle Row: The restored model of the first row, using Zernike fit. Last Row: The respective beam errors between the top two rows. Here, columns one and four are the amplitude beams of XX and YY respectively whilst the beams in the second and third columns are XY and YX correspondingly.

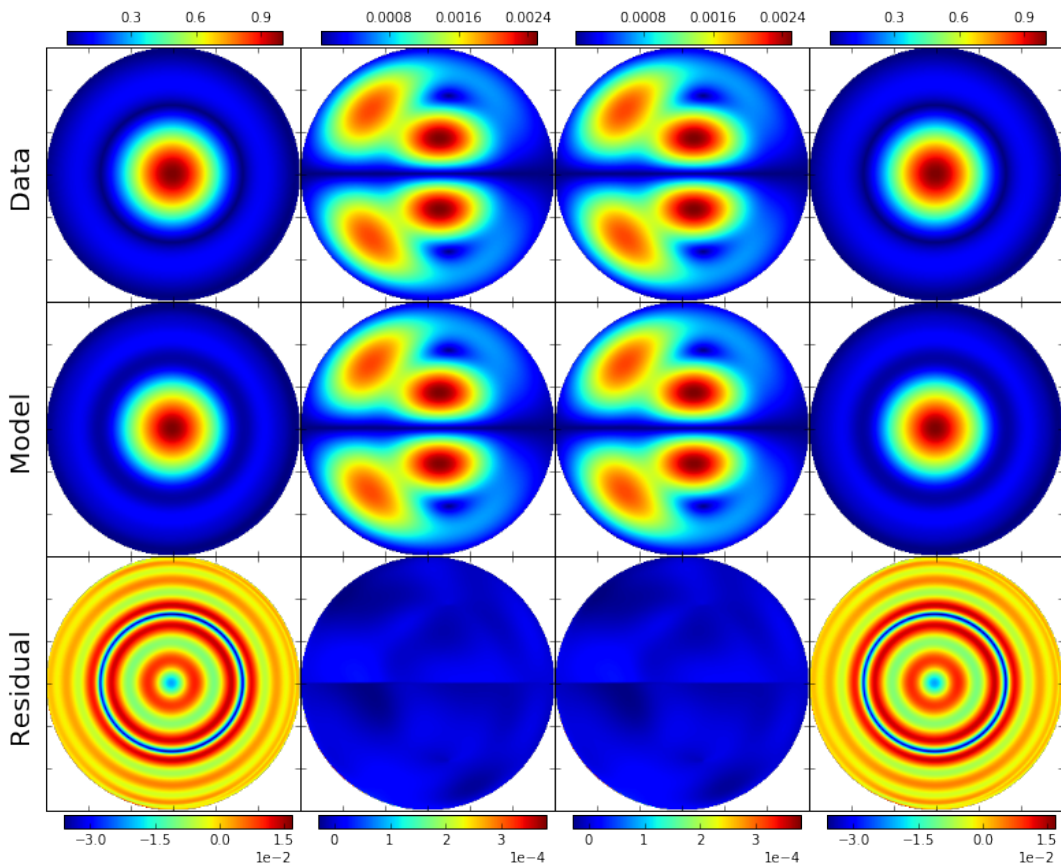


Figure 6.5: Top Row: Simulated EM model of SKA1-mid beam (in amplitude form) with a diameter of 6° at 990.5 MHz in a normalised unit. Middle Row: The restored model of the first row, using Zernike fit. Last Row: The corresponding beam errors between the 1st two rows. Here, columns one and four are the amplitude beams of XX and YY respectively whilst the beams in the second and third columns are XY and YX correspondingly.

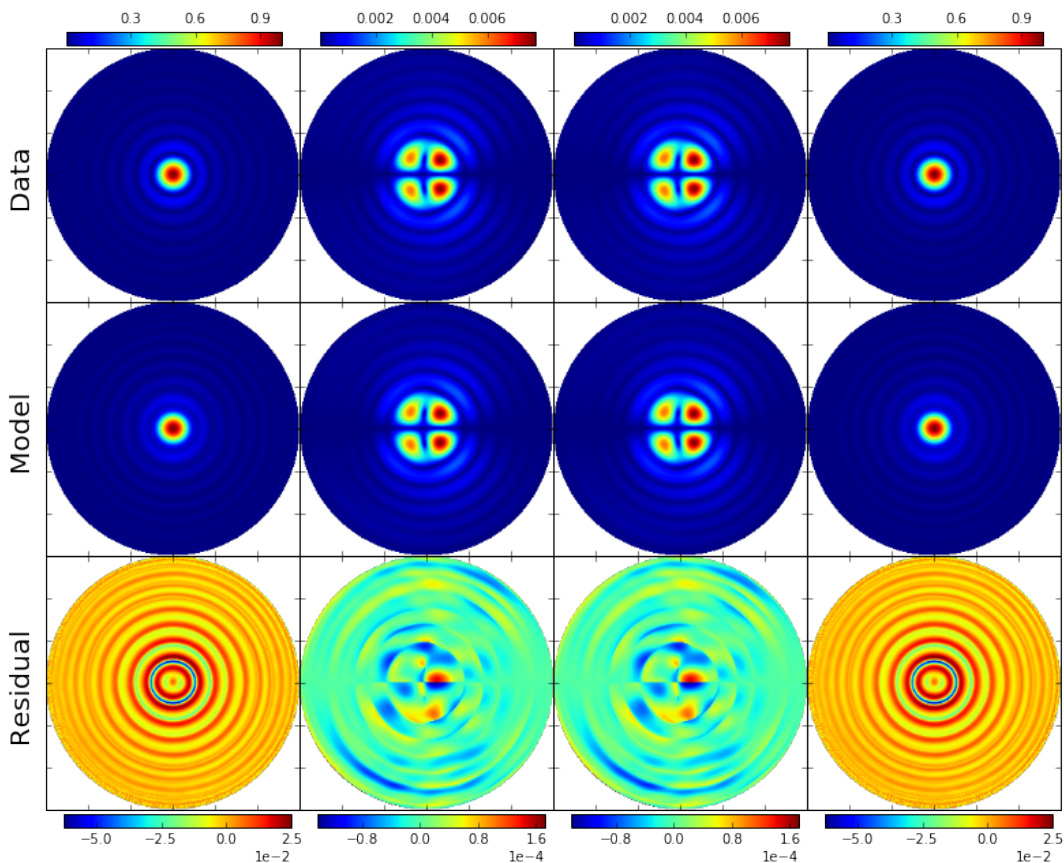


Figure 6.6: Top Row: Simulated EM model of SKA1-mid beam (in amplitude form) with a diameter of 4° at 13.6 GHz in a normalised unit. Middle Row: The restored model of the first row, using Zernike fit. Last Row: The corresponding beam errors between the 1st and 2nd rows. Here, columns one and four are the amplitude beams of XX and YY respectively whilst the beams in the second and third columns are XY and YX correspondingly.

6.3.1.2 Spectral Representation

Here, instead of fitting the Zernike model on a specific channel like we did in Section 6.3.1.1, the technique is applied on all the frequencies for all the bands in order to understand the beam behaviour across the frequencies and more importantly, interpolate for any missing channels and reconstruct the beams within Bands 1, 2 and 5. This can easily be done by generating the Zernike coefficients for these bands. This section presents spectra plots showing the strongest coefficients that is common in full polarization components (XX, XY, YX and YY) of all the channels for all the bands. The spectra plots displayed from Fig. 6.7 to 6.10 show that at lower wavelengths the ripple effect is much less than the higher ones, since the ripple must be in the order of wavelength. These plots are produced from the highest 6 Zernike coefficients for Bands 1, 2 and 5. The Z_j indexes in the legends are the Zernike basis functions in single modes.

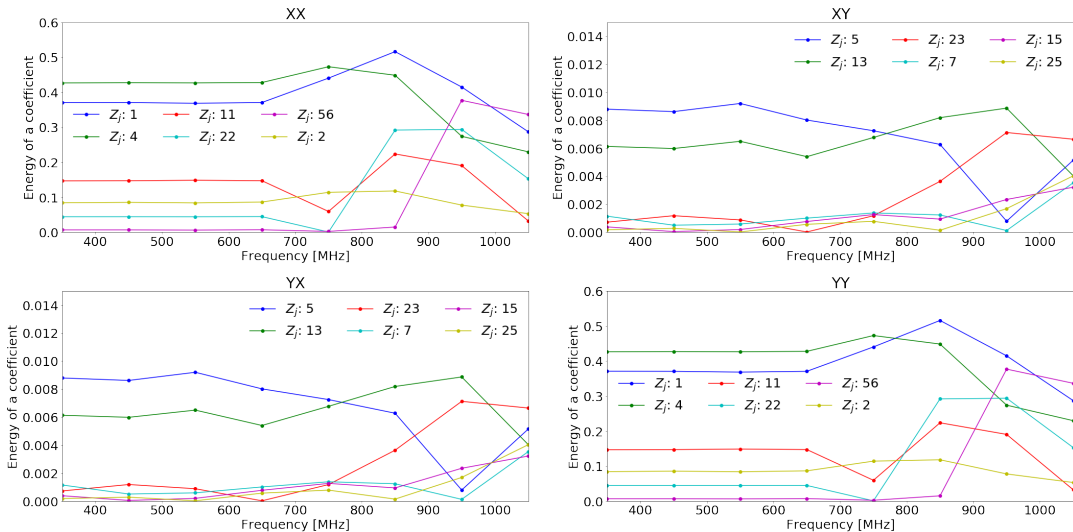


Figure 6.7: Spectral profile showing the various energy levels of Zernike coefficients for Band 1 (350 – 1050 MHz). The Zernike indexes (in the legends) are the activated basis functions that are frequent in all the channels.

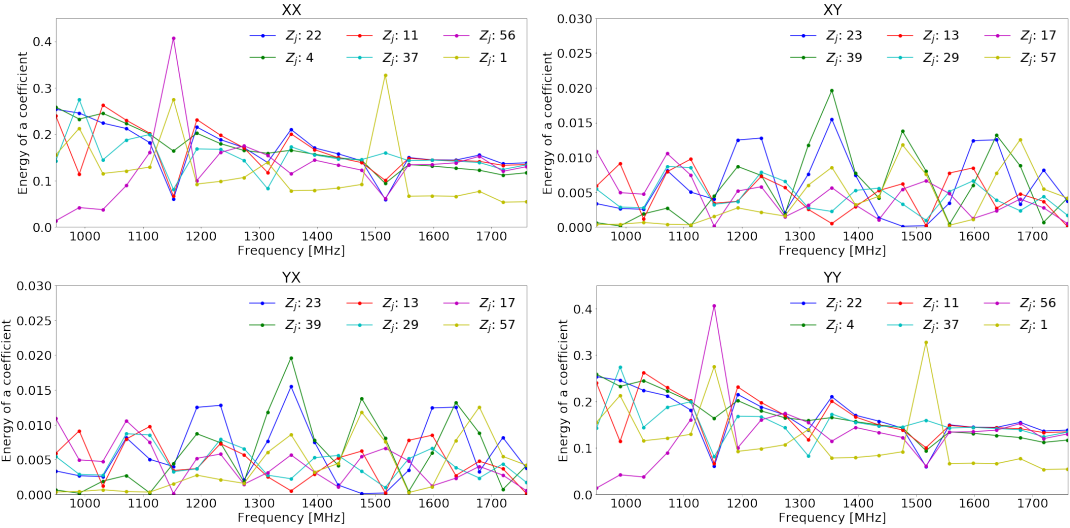


Figure 6.8: Spectral profile showing the various energy levels of Zernike coefficients for Band 2 (950 – 1760 MHz). The Zernike indexes (in the legends) are the activated basis functions that are frequent in all the channels.

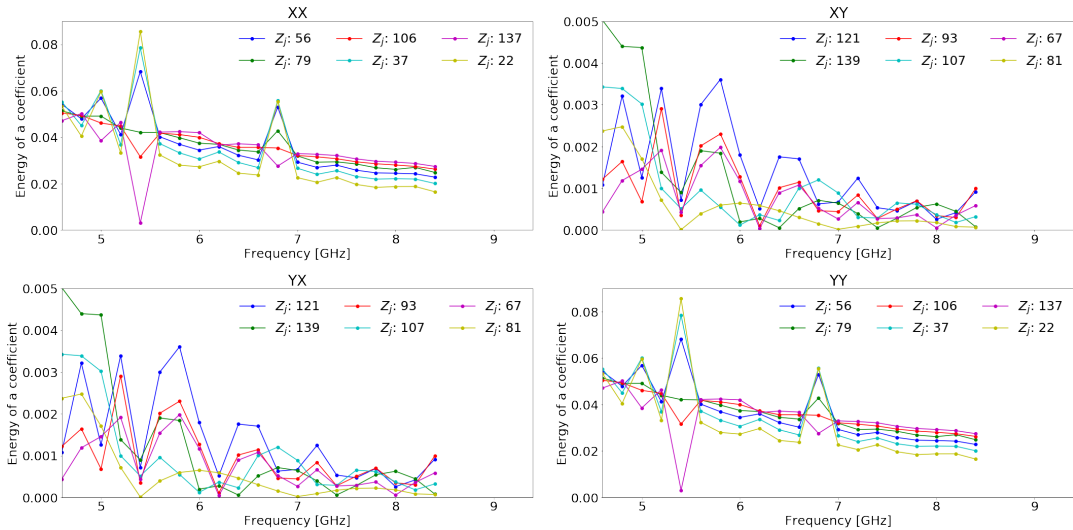


Figure 6.9: Spectral profile showing the various energy levels of Zernike coefficients for Band 5a (4.6 – 8.4 GHz). The Zernike indexes (in the legends) are the activated basis functions that are frequent in all the channels.

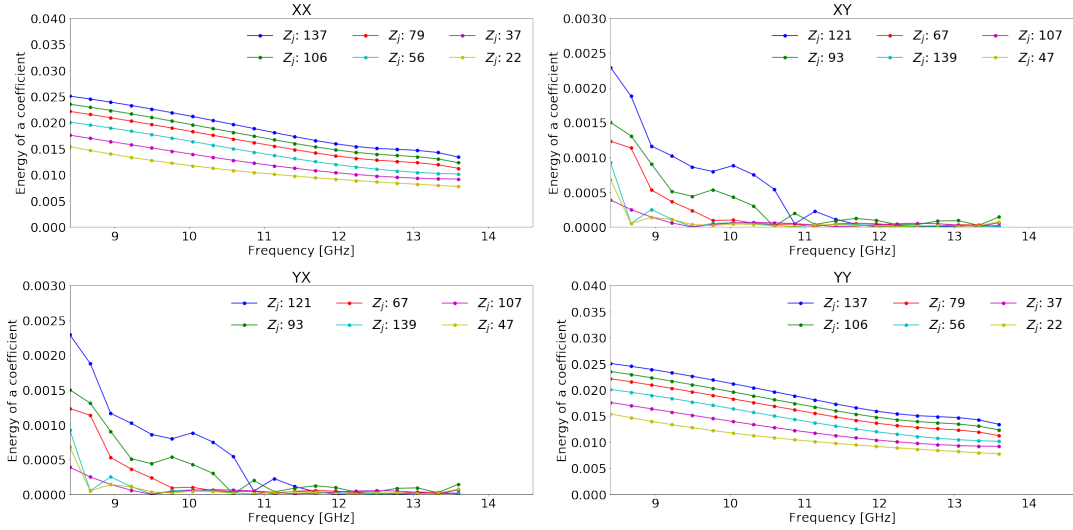


Figure 6.10: Spectral profile showing the various energy levels of Zernike coefficients for Band 5b (8.4 – 13.6 GHz). The Zernike indexes (in the legends) are the activated basis functions that are frequent in all the channels.

This is equivalent to the double index Z_n^m such that $n = \text{ceil}(-3/2 + \sqrt{[9+8j]/2})$ and $m = 2j - n^2 - 2n$. For instance, in Band 1 (350 - 1050 MHz), $Z_1 \mapsto Z_1^{-1}, Z_2 \mapsto Z_1^1, Z_4 \mapsto Z_2^0, Z_{11} \mapsto Z_4^{-2}, Z_{22} \mapsto Z_6^{-4}, Z_{56} \mapsto Z_{10}^{-8}$. We follow the same scheme to compute the double indexes for the other bands.

The next section presents how the GRASP beams are corrupted.

6.3.2 Model Beam Perturbation

Reflector imperfections can be considered by introducing thermal and mechanical distortions, gaps between reflector panels, supporting struts and scatterer material properties. In this work, we displace the receiver from its focus to alter the aperture illumination pattern of the dish. This introduces a regular phase perturbations across the aperture and also, a reduction in the signal gain. We can do this by adding regular phase error ($\sim 2^\circ$) in the beam-forming weight when generating the beams. The effect of this beam distortion at 450 MHz, 990.5 MHz, and 13.6 GHz is represented in Figs. 6.11, 6.12 and 6.13 respectively. Here, we note that there is a maximum error of $\approx 1\%$ in the residual plots (third row) of Figs. 6.11 and 6.12) and $\approx 10\%$ error in Fig. 6.13. The high sensitivity of errors in the Band 5b beams (refer to the perturbed images in Fig. 6.13) confirms a reduction in the antenna directivity which is very crucial in IM experiments.

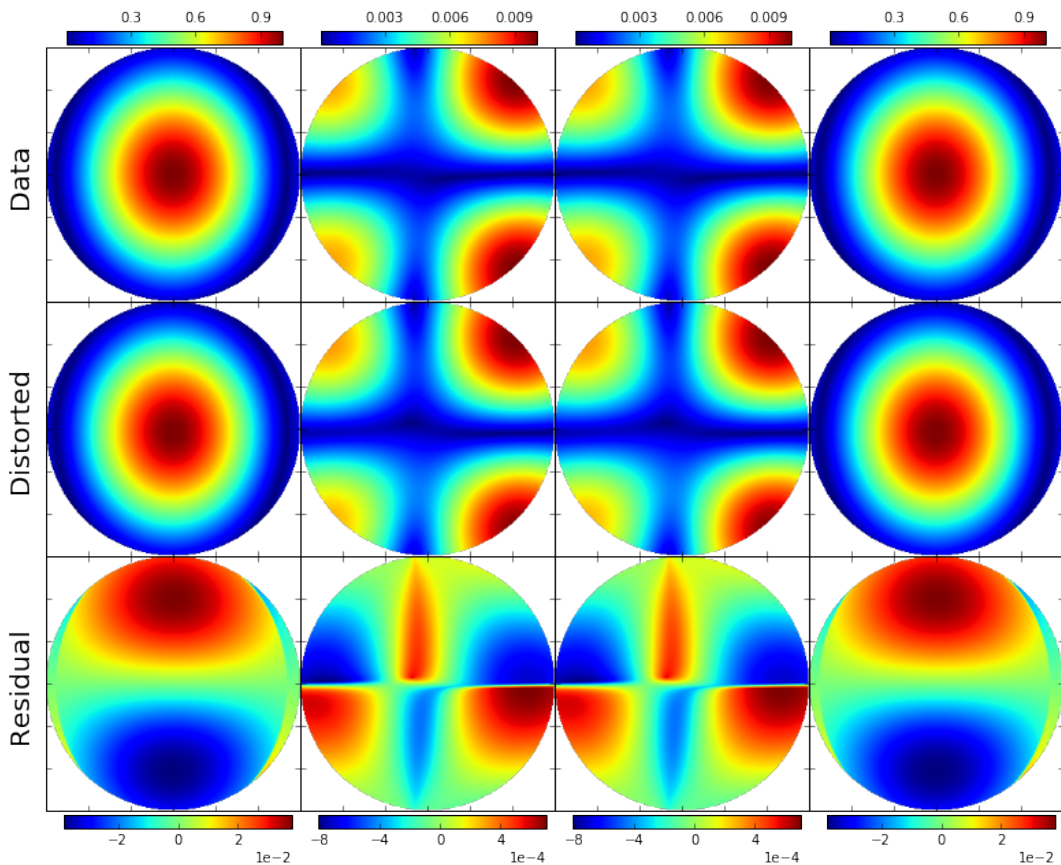


Figure 6.11: Perturbed beams for Band 1 at 450 MHz. The data part (row 1) represents the original EM beams and the second row shows the corrupted EM beams due to systematic phase errors. The last row reports the differences between the respective beams in the top beams. Note, the first and fourth columns are the amplitude beams of XX and YY respectively whilst the beams in the second and third columns are XY and YX correspondingly.

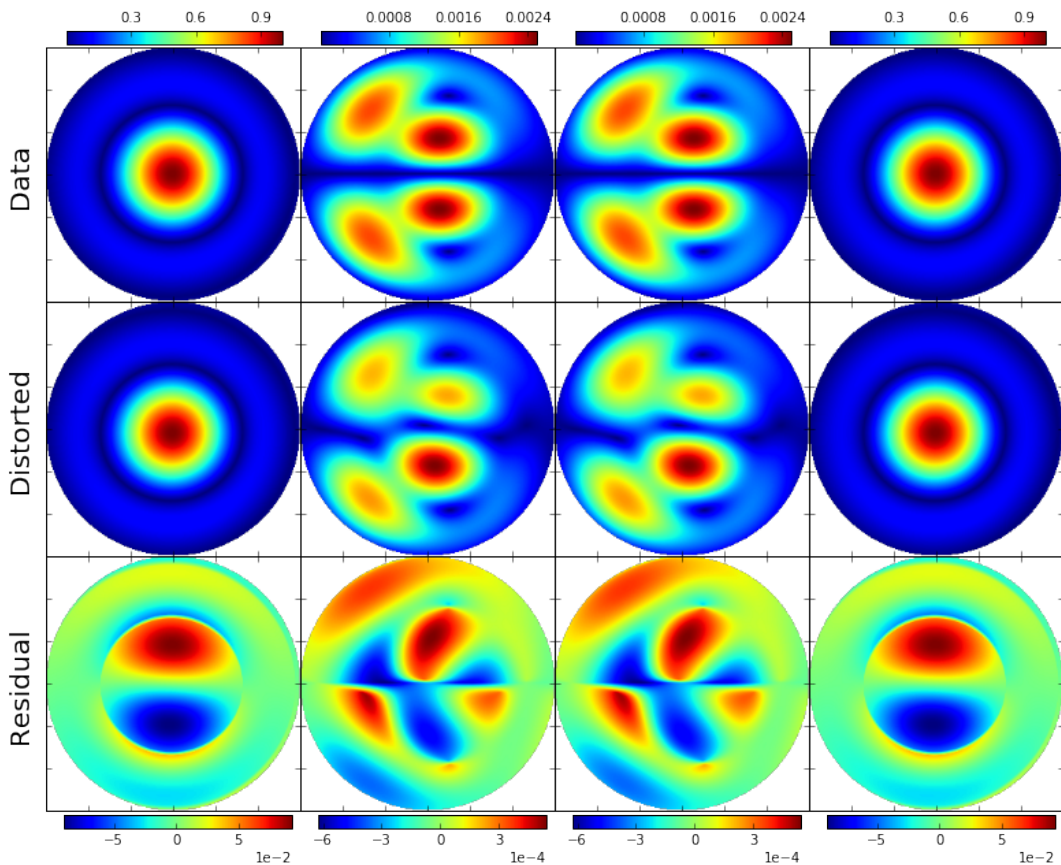


Figure 6.12: Perturbed beams for Band 2 at 990.5 MHz. The data part (row 1) represents the original EM beams and the second row shows the corrupted EM beams due to systematic phase errors. The last row reports the differences between the respective beams in the top beams. Note, the first and fourth columns are the amplitude beams of XX and YY respectively whilst the beams in the second and third columns are XY and YX correspondingly.

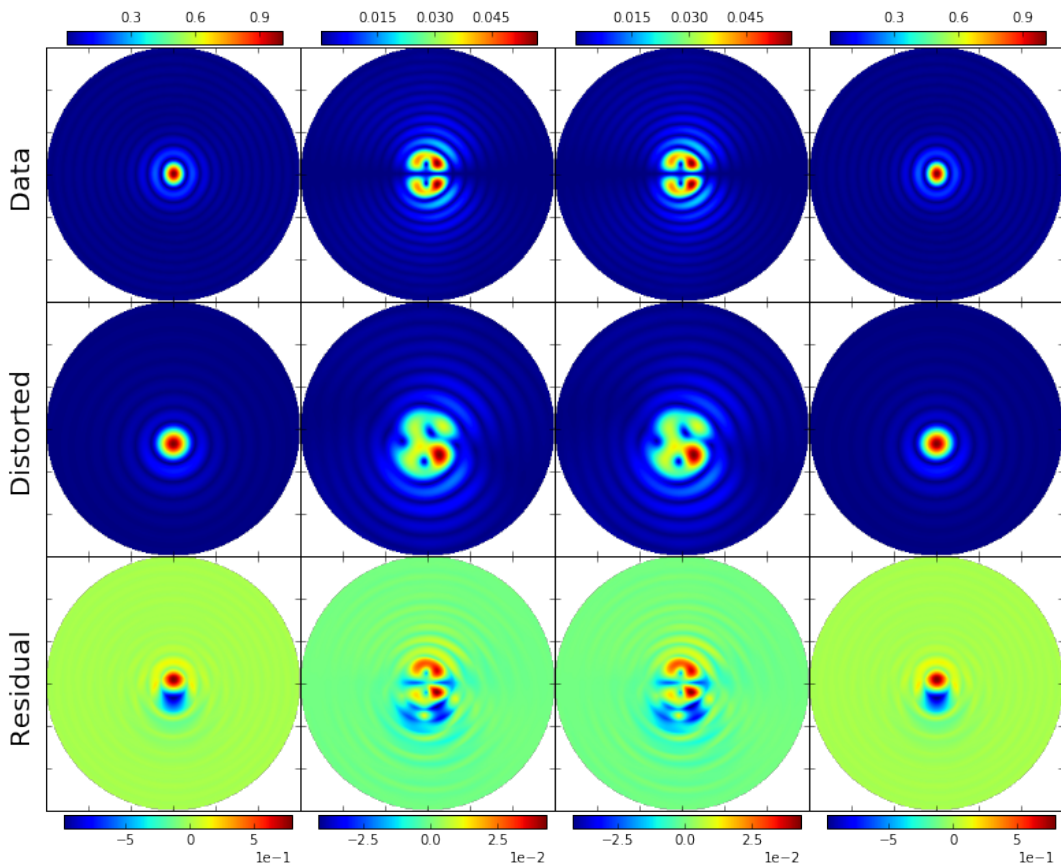


Figure 6.13: Perturbed beams for Band 5 at 13.6 GHz. The data part (row 1) represents the original EM beams and the second row shows the corrupted EM beams due to systematic phase errors. The last row reports the differences between the respective beams in the top beams. Note, the first and fourth columns are the amplitude beams of XX and YY respectively whilst the beams in the second and third columns are XY and YX correspondingly.

6.3.3 Intrinsic Cross-Polarisation (IXR)

Since the design of SKA1-mid is to operate in full polarization, it is therefore necessary to take measure of the performance of polarimetric. A common technique to do this is to use the intrinsic cross-polarization ratio (IXR) introduced in [24]. “IXR is essentially the Jones matrix condition expressed as a cross-polarization ratio, and as such it is a measure of how numerically stable the true polarization can be recovered from measured antenna voltages” [23].

In this work, we are interested in Stokes polarimeters and so, the IXR is computed by converting the Jones matrix into Mueller matrix. Chapter 4 discusses how the Mueller matrix is gleaned from the Jones formalism.

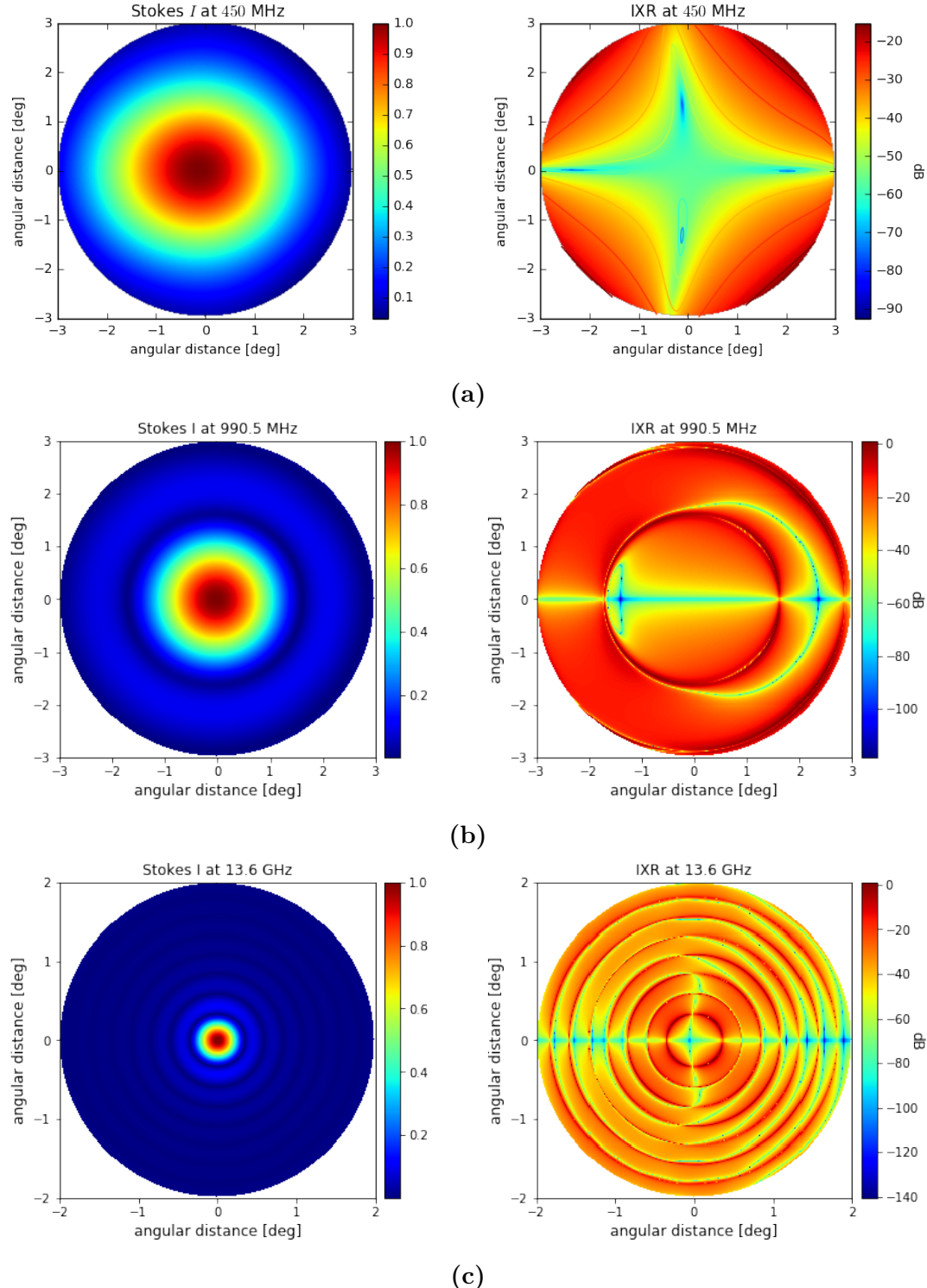


Figure 6.14: Representation of IXR_{mu} (right panels) with the corresponding Stokes I beams (left panels) at 450 MHz, 990.5 MHz and 13.6 GHz. Stokes I is computed in Jones terms as $(j_{xx}j_{xx}^* + j_{xy}j_{xy}^* + j_{yx}j_{yx}^* + j_{yy}j_{yy}^*)/2$.

Mathematically, we can present the IXR in Mueller form as:

$$IXR_{\text{mu}} = 10\log_{10} \left(\frac{\sqrt{M_{IQ}^2 + M_{IU}^2 + M_{IV}^2}}{|M_{II}|} \right) \quad (6.2)$$

The $I\chi R_{\text{mu}}$ relates to the ideal rate of polarization leakage (I into QUV and in reverse) of the beam. Fig. 6.14 shows the IXRs (the right plots) and the corresponding Stokes I beams (the left plots) for the various bands. The expected IXR for SKA1-mid is maximized at -20 dB in the direction of the phase centre. Here, the negative dB units shown in the colour bar plots denote an increase in the seepage away from the observation phase centre. In addition, the rings in the IXR plots correspond to the beam nulls where the signals can not be detected. Note how the ring spacing scales with frequency.

Now that we are well-informed about the SKA1-mid primary beams, we apply these with the foreground simulation discussed in Chapter 3 to estimate the spectral lines in this chapter. Next, we discuss the CO spectrum at $z \sim 3$.

6.4 The CO Power Spectrum

“In order to derive the power spectrum to be observed in typical CO intensity mapping experiments, one also needs to model the clustering of the CO sources. In analogy with the methods for other species, e.g., neutral hydrogen intensity mapping, this can be done by weighting the dark matter halo bias by the CO luminosity-halo mass relation” [83].

Here, the intensity of the CO signal S_{P}^{CO} is expressed as a wavenumber k_w at every z :

$$S_{\text{P}}^{\text{CO}}(k_w, z) = \langle T_{\text{b}}^{\text{CO}} \rangle(z)^2 [d_{\text{b}}^{\text{CO}}(z)^2 S_{\text{lin}}(k_w, z) + S_{\text{shot}}(z)] \quad (6.3)$$

where T_{b}^{CO} is the CO brightness temperature, d_{b}^{CO} is the CO halo bias source, S_{lin} is the power spectrum of linear matter, and S_{shot} is the addition of shot noise to the power spectrum.

Modelling the system in Equation 6.3 as a linear relation and projecting the CO intensity distribution into spherical form, we obtain a reduce function over the halo mass as given in Equation 6.4:

$$C_l = \langle T_{\text{b}}^{\text{CO}} \rangle(z)^2 \int S_{\text{lin}}(k_w, z) W_l(k_w) dk_w \quad (6.4)$$

The kernel function $W_l(k_w)$ in Equation 6.4 is defined in spherical Bessel expression as:

$$W_l(k_w) = \frac{2}{\pi} \left[\int_0^\infty j_l(u) f(u/k_w) du \right]^2 \quad (6.5)$$

where $f(u/k_w)$ is the weight describing the distribution of the source.

At large l , we can approximate the spherical Bessel function in Equation 6.5 such that $j_l(x) \approx \sqrt{\frac{\pi}{2l}} \delta(x - l)$ to get:

$$W_l(k) \approx \frac{1}{l} f(l/k_w)^2 \quad (6.6)$$

Therefore, as l becomes large, the kernel function changes along the k_w -axis. Replace

Equation 6.6 into 6.4 obtain the angular spectrum:

$$C_l \approx \langle T_b^{\text{CO}} \rangle(z)^2 \frac{1}{l} \int S_{\text{lin}}(k_w, z) f(l/k_w)^2 dk_w \quad (6.7)$$

Therefore, at $z \sim 3$, the signal is expected to be at most $1.5 \mu\text{K}$ at the halo bias level of $b(z) = 0.2$ [46]. Using this normalisation constant, we can translate Equation 6.7 into an integral over radial co-ordinate:

$$C_l \approx 2.25 \times 10^{-6} \int S_{\text{lin}}(k_w, z) f(l/k_w)^2 dk_w \quad [\text{mK}^2] \quad (6.8)$$

Due to the variations in gravitational energy and mass density, we consider the spatial spectrum to have a power law such that $S_{\text{lin}}(k_w, z) \propto k_w^n$ and therefore, we can evaluate the angular spectrum as $C_l \propto l^{-n}$. For $n = 1$ gives $C_l \propto \frac{1}{l(l+1)}$ at low l .

In this work, we adopt the **CAMB**⁶ software package to compute the C_l of CO signal at $z = 3$. This package is able to set cosmological parameters in terms of physical densities and parameters used in [2].

6.5 Results and Analysis

Repeating the full-sky simulation discussed in Chapter 4, we perform IM experiments by convolving the foregrounds in Figs. 3.5, 3.6, and 3.7 with the simulated GRASP beams (original EM beams), Zernike reconstructed beams and the distorted modelled beams for each band (at 450 MHz, 990.5 MHz and 13.6 GHz). Note here that these voltage beams must first be converted into their Mueller forms before applying them to the polarized sky maps. Fig. 6.15 shows the systematic error maps⁷ for Band 1 (at 450 MHz) when we compute the differences between the convolved foregrounds using the fully polarized GRASP beams (in Mueller form) that are obtained from the beams in Fig. 6.4 (Data row) and the distorted beams in Fig. 6.11 (Distorted row). Fig 6.16 also shows the the differences between the measured foregrounds using the same GRASP beams in Fig. 6.4 (Data row) and Zernike beams in Fig. 6.4 (Model row). Similar explanations can be given to the error maps in Figs. 6.17, 6.18 and Figs. 6.19, 6.20 for using Bands 2 (at 990.5 MHz) and 5 (at 13.6 GHz) fully polarized primary beams accordingly.

⁶<http://camb.readthedocs.io/en/latest/>

⁷The grey parts of the error plots are masked galaxies.

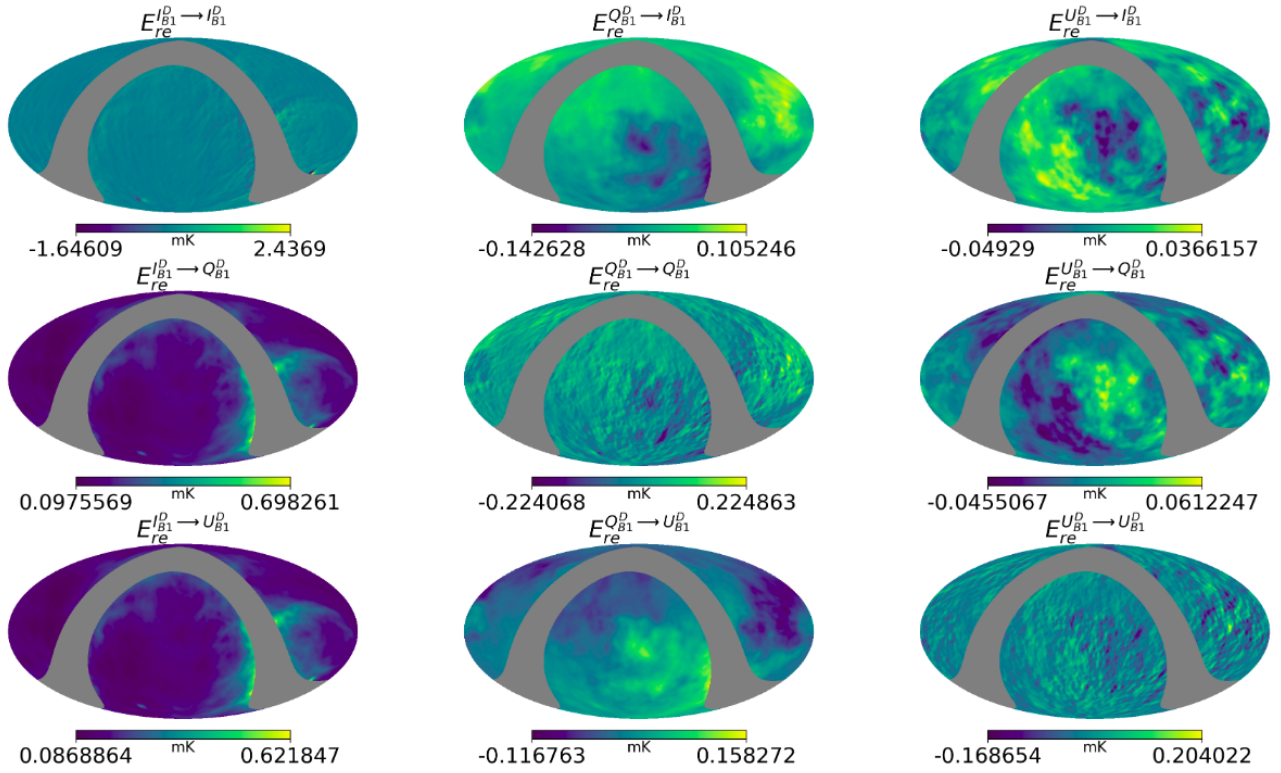


Figure 6.15: Systematic errors of the measured maps in Stokes I, Q, U, due to feed displacement at 450 MHz.

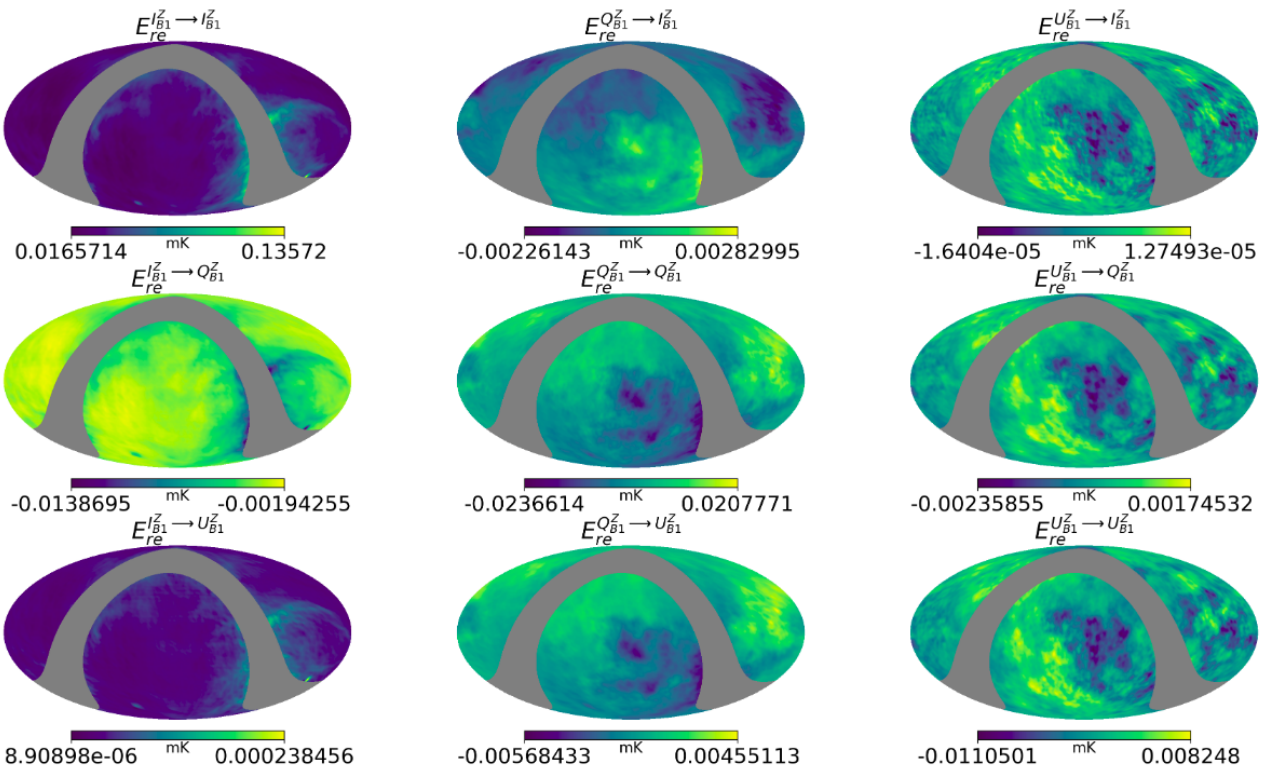


Figure 6.16: Systematic errors of measured maps using Zernike model beams at 450 MHz.

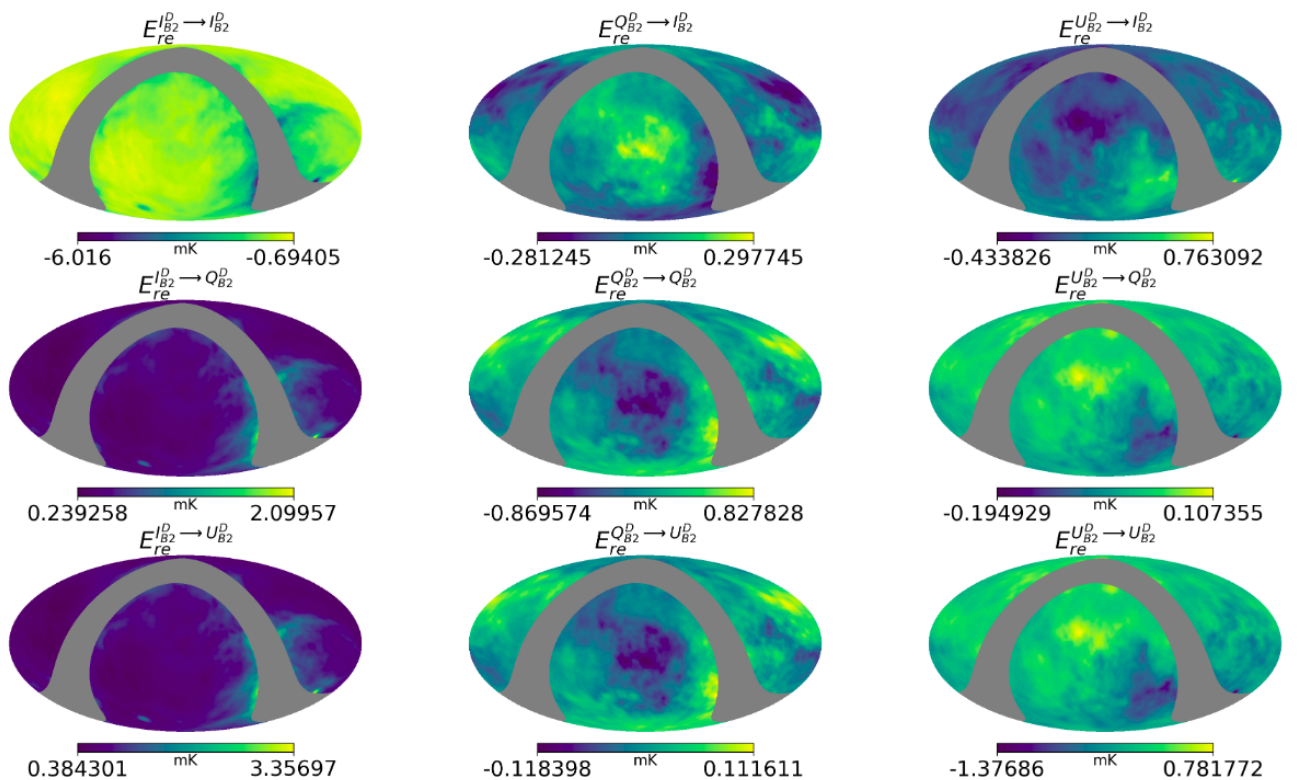


Figure 6.17: Systematic errors of measured maps due to feed displacement at 990.5 MHz.

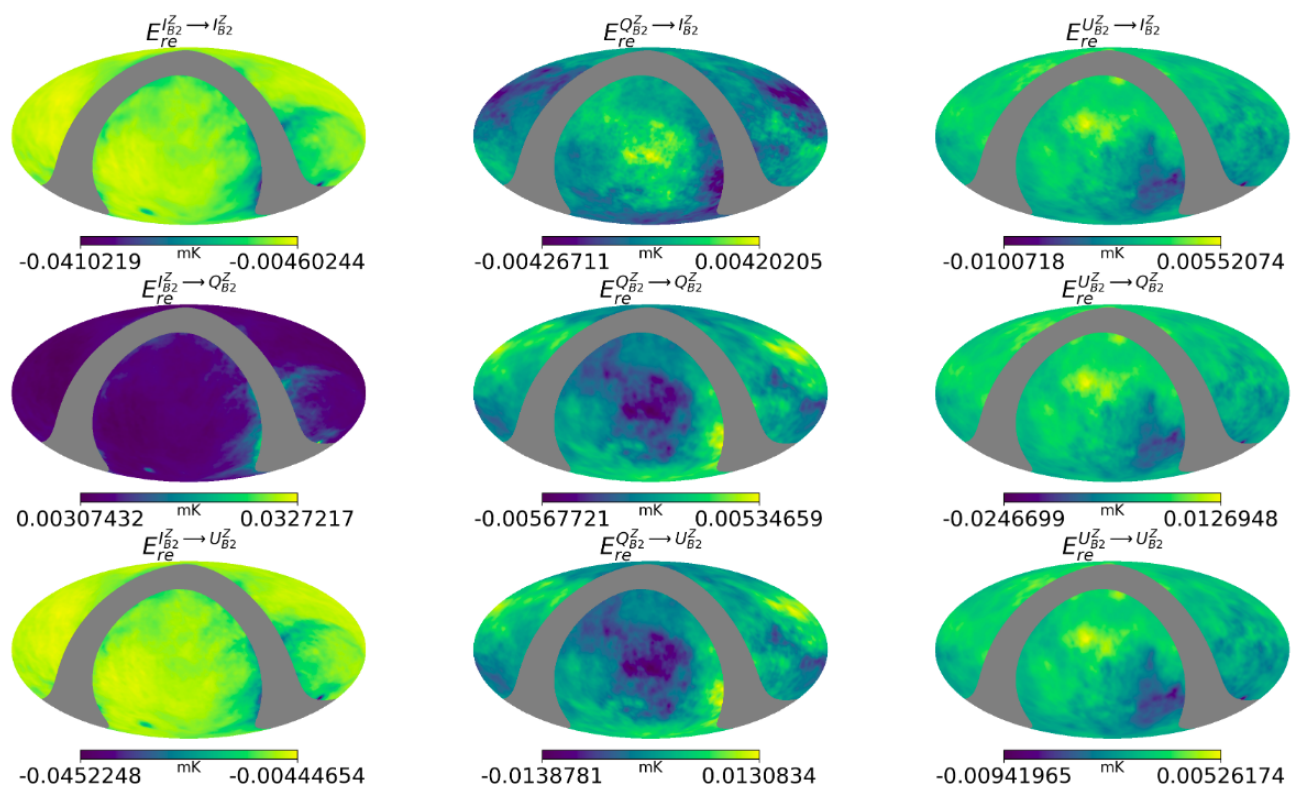


Figure 6.18: Systematic errors of measured maps using Zernike model beams at 990.5 MHz.

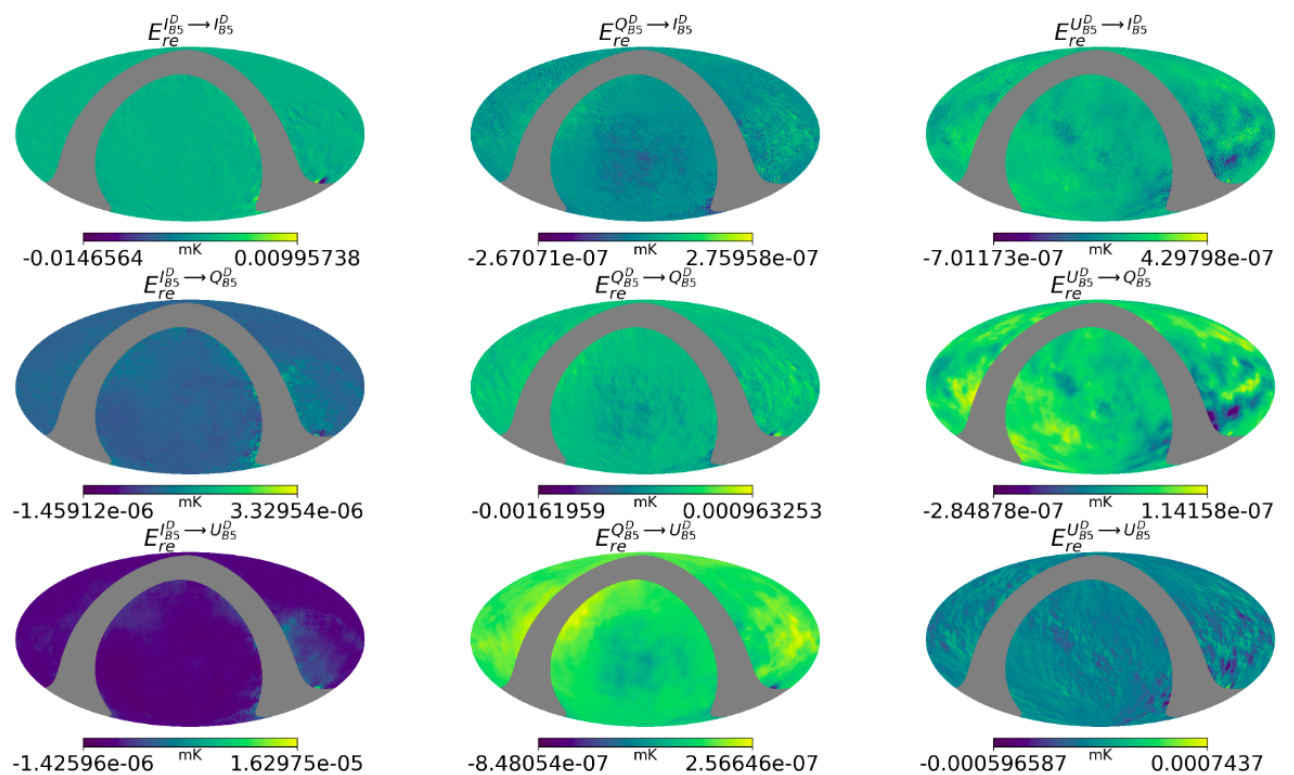


Figure 6.19: Systematic errors of measured maps due to feed displacement at 13.6 GHz.

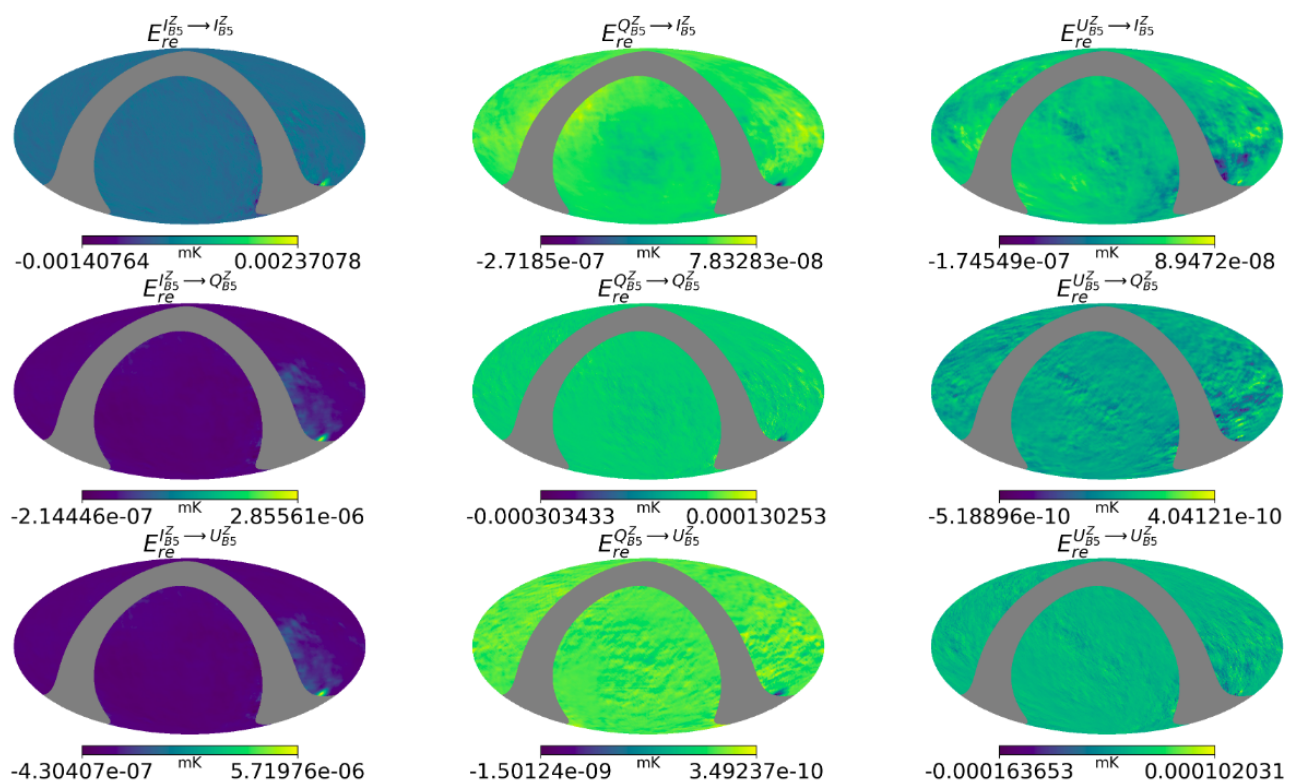


Figure 6.20: Systematic errors of measured maps using Zernike model beams at 13.6 GHz.

Fig. 6.21 is produced when we convolve the full-sky polarization maps in Fig. 3.7 with the primary beams at 13.6 GHz. The maps in the first row are the convolved foregrounds, using the complete beams of the original simulated GRASP model in Fig. 6.6 (Data row). The second row is obtained for using the perturbed beams in Fig. 6.13 (Distorted row) and the third row is as a result of using the Zernike beam models in Fig. 6.6 (Model row). The remaining two rows are the respective errors in Stokes I, Q and U for using distorted and reconstructed beam models. Next, we quantify the foregrounds measured by transforming these spatial distributions into spherical harmonics to determine the angular power spectrum.

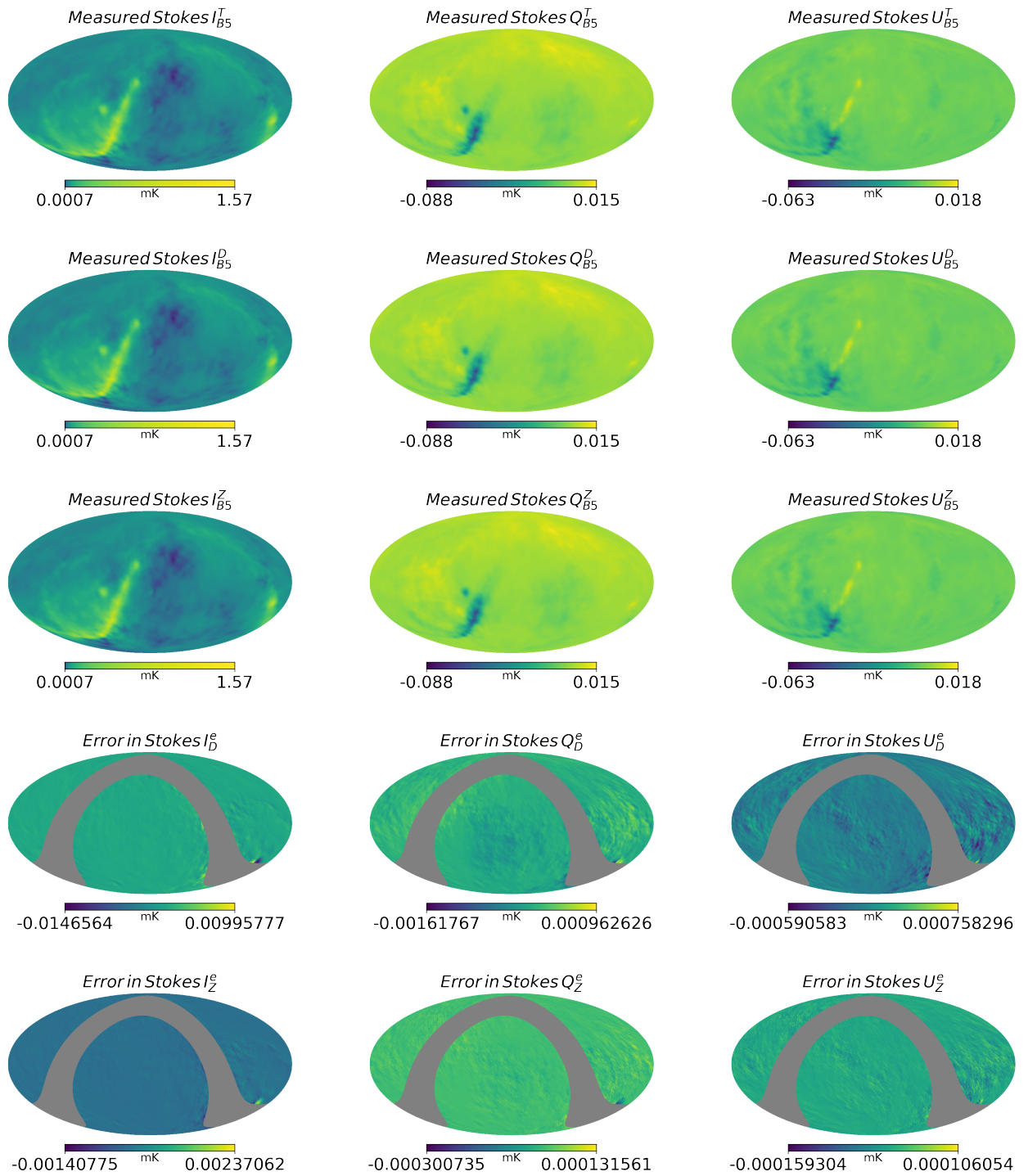


Figure 6.21: Convolved full-sky maps at 13.6 GHz with respective error in Stokes I , Q and U .

The power spectra plots reported in Fig. 6.22 enable us to estimate both the HI (grey-magenta circular spectral plots) and CO (grey spectral plots) signals at a specific multipole moment. The left spectra plots in Figs. 6.22a, 6.22b, 6.22c show how we recovered the HI and CO signals in Stokes I when the errors in the primary beams of a particular band are corrected. For instance, in Band 1 (at 450 MHz), when the beam errors are corrected in Stokes I , we expect the HI signal at $z \approx 0.67$ to be measured at a multipole moment of $l \lesssim 50$ which is about 3 orders of magnitude greater than that of the foreground at lower scales. In the case of Band 2 (at 990.5 MHz), the HI signal is also measured at a multipole moment of $l \lesssim 50$ and about 4 orders of magnitude greater than the foreground at lower scales. For the Band 5 (at 13.6 GHz), the CO signal at $z \approx 3$ is expected to be measured at a multipole moment of $l \ll 50$ which is about 3 orders of magnitude lower than the foreground at lower scales. On the other hand, the right spectra plots in Figs. 6.22a, 6.22b, 6.22c show how we measure the signals when the intrinsic linear polarization leakage in Stokes I is known whilst the errors in the primary beams of a particular band are not corrected. The power spectrum of the HI signal for Bands 1 and 2 can be estimated at a multipole moment of ≈ 50 and ≈ 100 respectively. For Band 5, the estimated power spectrum of the CO signal can be estimated up to a multipole moment of ≈ 50 . In addition, the spectra plots due to Zernike model of the beam for all bands clearly predicted both the HI and CO signals to be at a multipole moment of $l \lesssim 50$, making Zernike fitting a good reconstructed model for intensity mapping experiments.

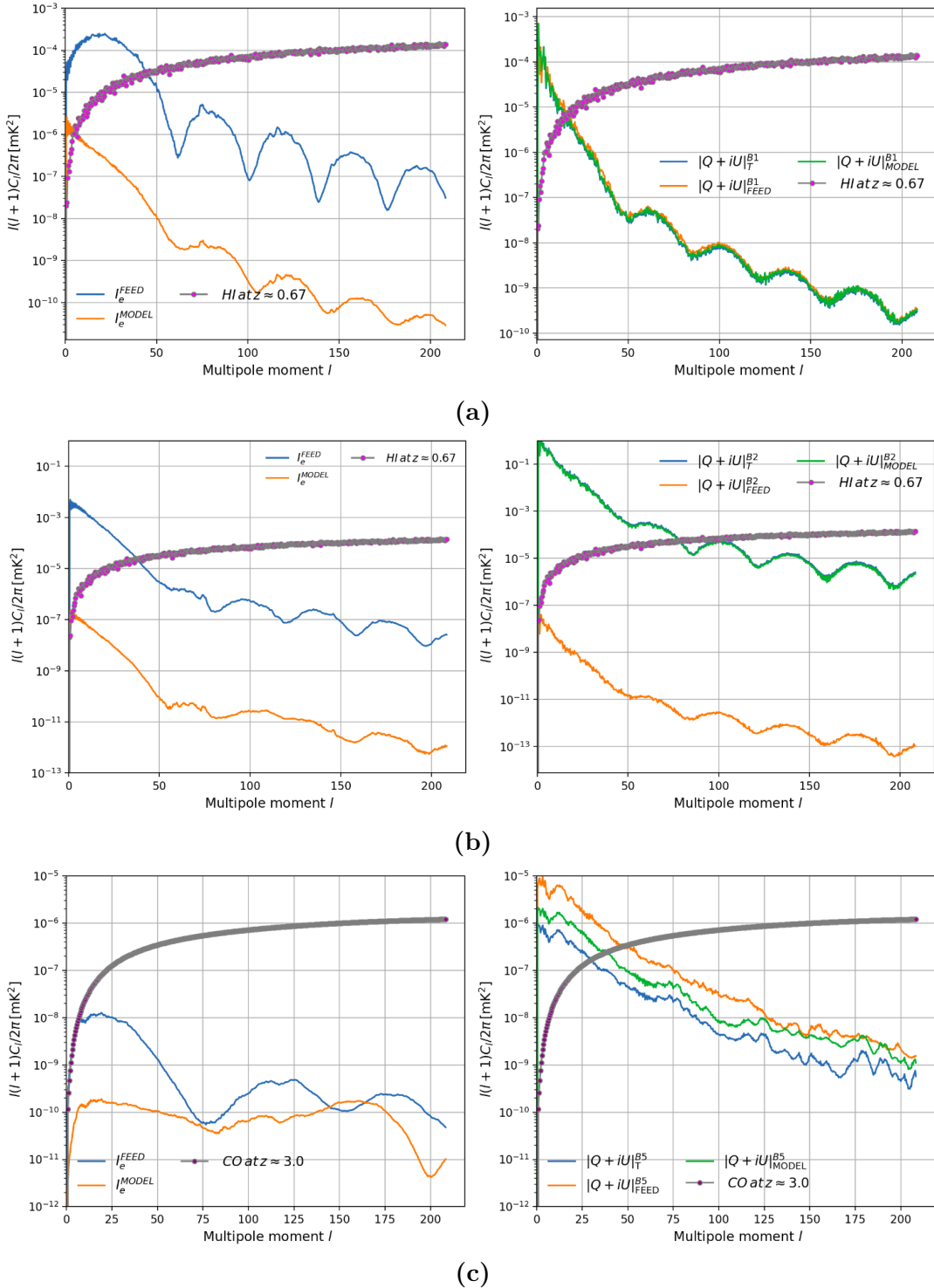


Figure 6.22: Comparing the distribution of angular power plots between corrected beam errors due to Zernike fits or feed displacement in Stokes I map (left plots) and intrinsic polarization leakage in I (right plots) and how these affect both the 21 cm and CO signal (solid circular spectrum plot). (a) For Band 1 at 450 MHz (b) For Band 2 at 990.5 MHz (c) For Band 5 at 13.6 GHz

6.6 Conclusion

This work showed how to simulate EM primary beams of SKA1-mid for Bands 1, 2 and 5 using **GRASP**, a commercial software package. A Zernike fit was then used to reproduce these EM beams and then went on further to produce errors beams by including a systematic phase perturbations across the aperture to corrupt the beam pattern. HI IM experiment was performed with the primary beams of Bands 1 (at 450 MHz) and 2 (at 990.5 MHz) and then CO IM with Band 5 (at 13.6 GHz) in order to estimate the power spectrum of both HI and CO signals. The following are the key findings of the research:

- We can use the MSE approach to choose the required number of Zernike modes with the corresponding coefficients to reconstruct the beams. Here, we select the modes where the MSE converges (refer to Fig. 6.3). Note that the selected coefficients are what we define as the strongest coefficients.
- Reconstructing the original EM beams with the Zernike model, produces a maximum residual error of $\simeq 1\%$ (refer to the bottom rows of Figs. 6.4, 6.5 and 6.6) for Bands 1 (at 450 MHz), 2 (at 990.5 MHz) and 5 (at 13.6 GHz).
- In addition, Zernike polynomial is a good model to study the ripple effect in the beams for all channels (refer to Figs. 6.7 to 6.10). The research shows that, due to the order of wavelength of the beams, the ripple effect is much less at higher bands as compared to the lower bands.
- There are different ways to realistically introduce inaccuracies in the primary beams. For the purpose of this work, a very simple way to do this is to include systematic phase errors in the beam-forming weight ($\sim 2^\circ$) in order to displace the mechanical feed slightly from its focus. The effect of this is seen Figs. 6.11 to 6.13.
- Ideally, to measure the intrinsic polarization leakage of the beam irrespective of the pointing direction, we adopt the IXR approach. Therefore, as we observe closely to the Zenith direction, we obtain an $|IXR|$ of 20 dB. This value increases as we gradually move away from the phase centre (refer to Figs. 6.14).
- The angular power spectra plots in Figs. 6.22a, 6.22b, 6.22c show that when we correct the errors in the beam in Stokes I , the power of the 21 cm signal can be determined at a multipole moment of $l \lesssim 50$ for Bands 1 and 2 and that of the CO signal can be estimated up to a multipole moment of $l \ll 50$ for Band 5. However, if the errors in the beam are not corrected in Stokes I because we do not have a prior knowledge of a true modelled beam, then we expect both signals to be estimated at $l > 50$ (for Bands 2 and 5) and at $l > 25$ (for Band 1).

In summary, the study shows that Zernike is a very good model for performing HI and CO IM experiments. In addition, although the SKA1-mid is not exclusively built for

IM experiments, these simulations have clearly shown that it can be used to investigate HI and CO IM experiments. However, care should be taken when performing CO IM, since the narrow beamwidth of the instrument at higher bands requires accurate dish surface regularity in addition to strong pointing accuracy. This is relatively less of a problem at lower bands with broader beamwidth.

Chapter 7

Conclusions and Recommendations

IM is very sensitive to the aggregate line emission of galaxies other than the limiting magnitude of traditional galaxy surveys, which focus on only discrete sources whose emission lies above some flux threshold, defined within a limited aperture. As such it represents a promising technique for statistical studies of galaxies that are faint. However, to extract the meaningful information we have to address the exact subtraction of the foreground continuum signal from Galactic and extra-galactic radio sources. The main focus of this work is to develop IM techniques for mapping out primary beams of a radio telescope and then, introduce realistic errors to perturb these modelled beams. We then attempt a correction and calibration of these distorted modelled beams and ultimately, use the final data for IM experiments. Thus, we use these modelled beams to simulate the full-sky polarization maps and then, determine the amount of foregrounds that have corrupted the total intensity due to polarization leakage and errors in the primary beams which have not been accounted for. Therefore, the two critical things the study addresses are:

- (i) the contribution of polarization leakage to the measured HI and CO power spectrum, given some more or less realistic primary beams; and
- (ii) the uncertainty on the estimate of (i) introduced by unmodelled perturbations in the primary beam.

The following are some of the main findings of the research:

- A realistic primary beam pattern can be simulated with the **OSKAR** software by modelling a single dish as a collection of dipoles, such that the orientation of the dipoles are uniformly distributed across the radius of the dish.
- Zernike fitting is a good model to reconstruct primary beams especially at Bands 1 and 2 hence, a very useful tool for IM experiments .
- If we consider a correct model of the primary beam, then the intrinsic partial leakage of linear polarization ($|Q + iU|_T \rightarrow I$) is given at $\approx 1.0\%$, hence, making it possible to evaluate the angular spectrum of both CO and 21 cm at

a multipole moment of $l \lesssim 50$ which agrees with when we correct for the beam errors in Stokes I . However, this is contrary if no beam correction is made.

- Convolution is also a very good technique for IM experiments since we can use this approach to measure total intensity of a signal.
- CO IM is more difficult to perform as compared to HI IM, because this type of experiment is observed at high frequencies and when an antenna has a very large gain, the beamwidth is also very small and the antenna requires very careful control over its position.

Future expansion of this work is as follows:

- Use the PCA and Spherical harmonics models of MeerKAT L-band primary beams that are discussed in [9] to perform IM experiment and validate our existing results.
- Explore other beam distortions schemes such as dish mis-alignment and secondary blockage (supporting frames) to give a better understanding of the primary beam effects on IM.
- Adopt recent techniques such as deep learning algorithms to also investigate the potential of IM experiments.

In short, with a good model of the primary beams we can actually estimate the amount of foregrounds that leak from intensity to polarization.

Appendices

Appendix A

OSKAR BEAMPATTERN AND FOREGROUND SIMULATIONS

A.1 Modelled and measured beams

The Mueller matrix representations in Fig. A.1 show the different perturbation methods (i.e. gain, phase and surface orientation errors) used to corrupt the OSKAR beam model. Note that the distortions in Fig. A.1, are clearly visible at the upper and lower diagonals of the beams. These perturbed beams are then compared with the errors produced from “real” measured beams of the VLA in Fig. A.2. The PBs presented in Fig. A.2 are taken from 2 different stations (i.e. antennas 5 and 6) whose fractional differences (refer to Fig. 4.4d) are relatively higher than any other pair of stations.

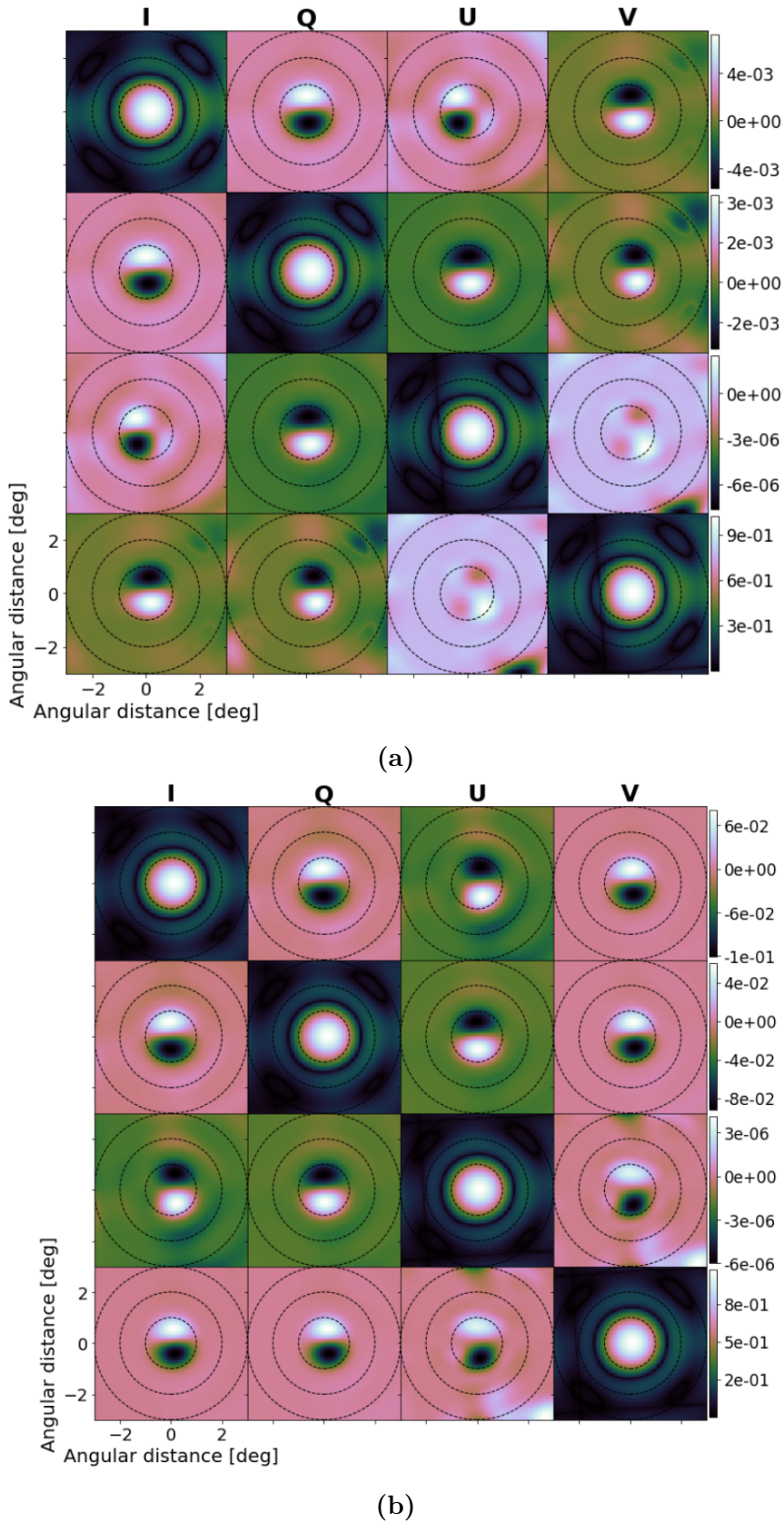


Figure A.1: Fully polarised distorted primary beams of KAT-7. (a) Due to gain and phase errors. (b) Due to dipole orientation errors.

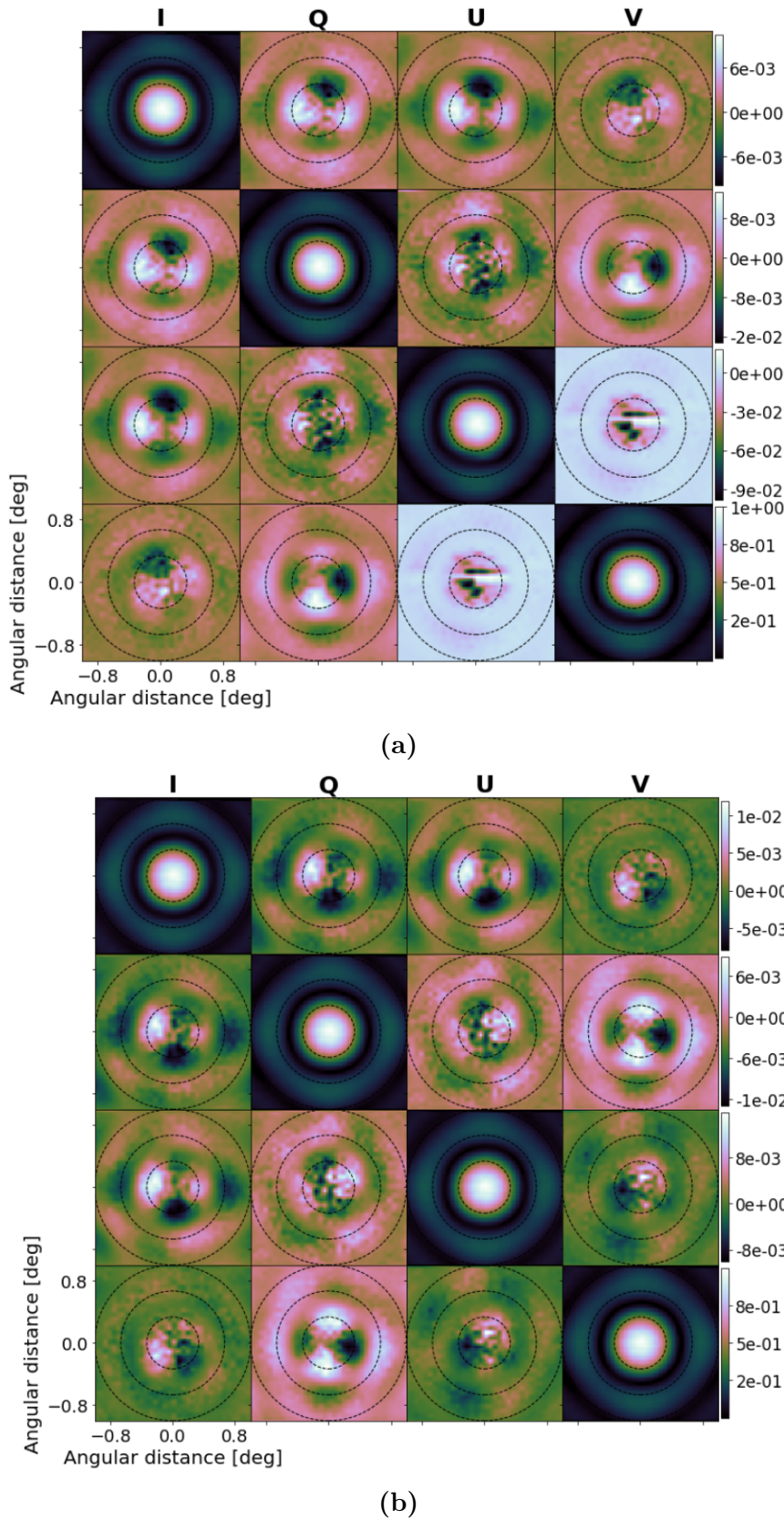


Figure A.2: 1 GHz holography measured Mueller beams of VLA. (a) Antenna 5. (b) Antenna 6.

A.2 Measured Full-sky maps

Figs. A.4 and A.5 represent the respective systematic error maps and the overall full-sky convolved maps simulated with the holography measured beams JVLA in Fig. A.2. The latter maps are used to produce the convolved power spectrum of the JVLA as presented in Fig. 4.7.

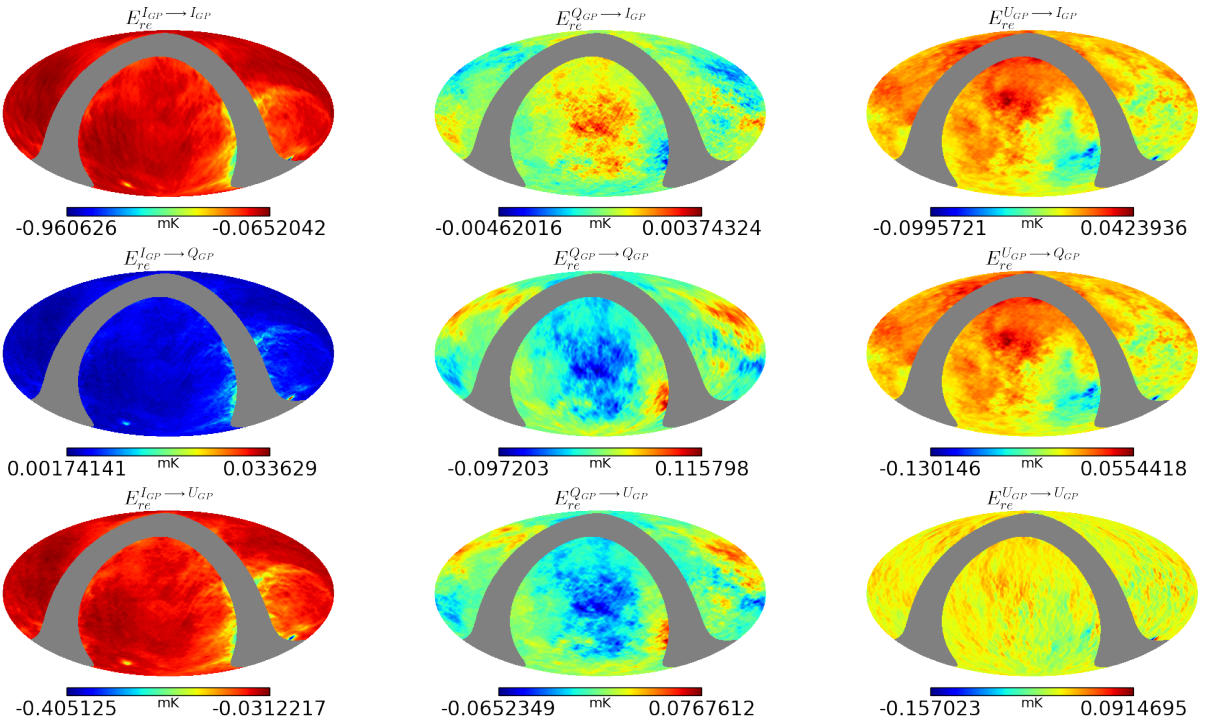


Figure A.3: Systematic errors of full-sky maps produced by computing the relative error between the absolute of the convolved true sky maps and the corrupted sky maps due to gain and phase error beams.

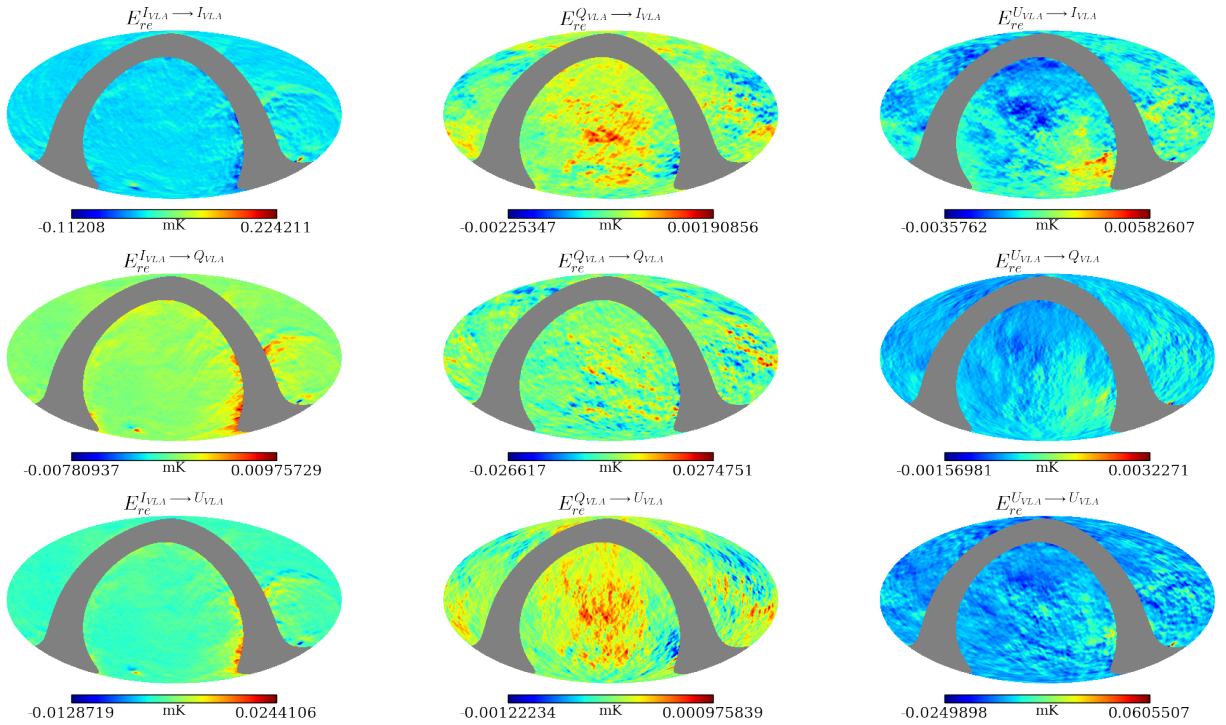


Figure A.4: Systematic differences of the full-sky polarisation maps produced by computing the relative error between the convolved sky using VLA PBs in Fig. A.2.

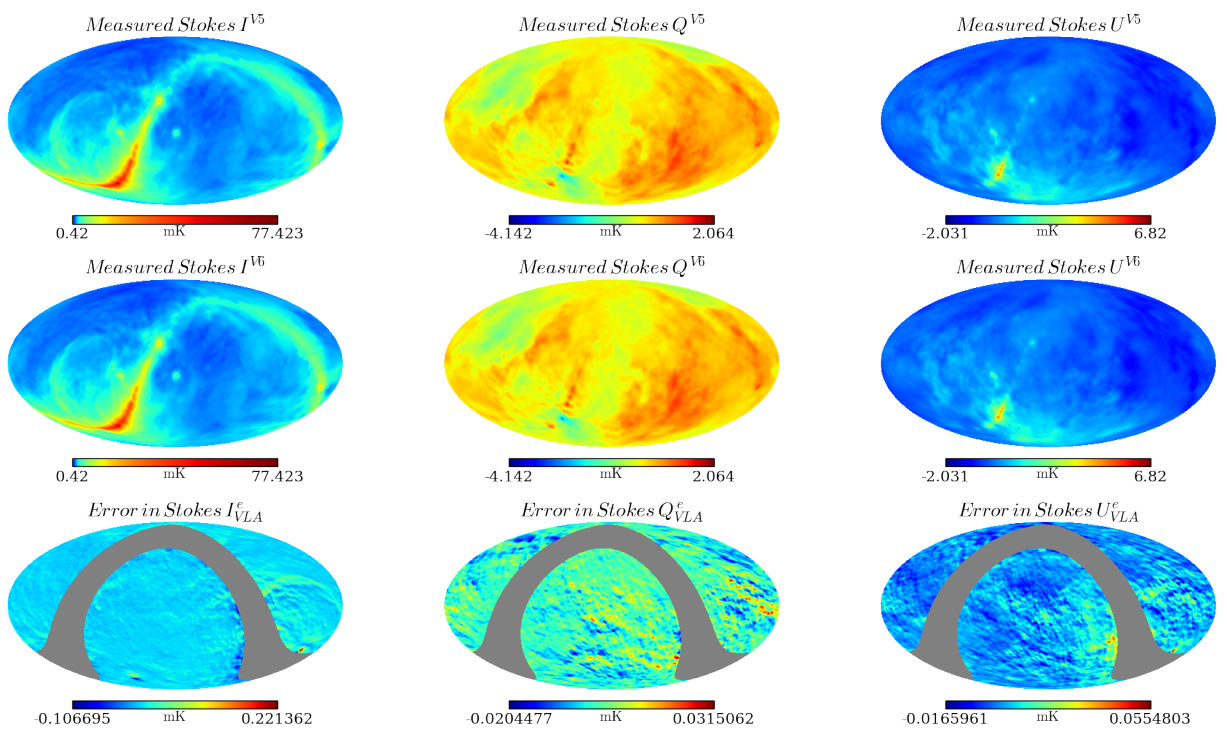


Figure A.5: Measured Stokes I , Q and U for holography measured beams of JVLA with corresponding errors terms.

Appendix B

Zernike Polynomial Sequence

In this research, we will deal exclusively with the double indexed Zernike polynomials as portrayed by Campbell [21], Lakshminarayanan & Fleck [69].

Table B.1: Relationship between single and double index schemes to third order.

Radial order, n	Angular frequency, m						
	-3	-2	-1	0	1	2	3
0				$j = 0$			
1			$j = 1$		$j = 2$		
2		$j = 3$		$j = 4$		$j = 5$	
3		$j = 6$		$j = 7$		$j = 8$	$j = 9$

B.1 Orthonormality

The orthonormality of the Zernike polynomials of modes k and k' can be expressed as:

$$\frac{\int_0^1 \int_0^{2\pi} Z_k(\rho, \theta) Z_{k'}(\rho, \theta) \rho d\rho d\theta}{\int_0^1 \int_0^{2\pi} \rho d\rho d\theta} = \delta_{kk'} \quad (\text{B.1})$$

where $\delta_{kk'} = \begin{cases} 1 & \text{if } k = k' \\ 0 & \text{if } k \neq k' \end{cases}$. The function in Equation B.1 can be defined in radial orthogonality term as:

$$\int_0^1 R_n^m(\rho, \theta) R_{n'}^{m'}(\rho, \theta) \rho d\rho = \frac{1}{2(n+1)} \delta_{nn'} \quad (\text{B.2})$$

and angular orthogonality term as:

$$\int_0^{2\pi} d\theta \begin{cases} \cos m\theta \cos m'\theta \\ \sin m\theta \sin m'\theta \\ \cos m\theta \sin m'\theta \\ \sin m\theta \cos m'\theta \end{cases} = \begin{cases} \pi(1 + \delta_{m0})\delta_{mm'} \\ \pi\delta_{mm'} \\ 0 \\ 0 \end{cases} \quad (\text{B.3})$$

Bibliography

- [1] Abitbol M. H., Hill J. C., Johnson B. R., 2016, *MNRAS*, **457**, 1796
- [2] Ade P. A. R., et al., 2016, *Astron. Astrophys.*, **594**, A13
- [3] Adriani O., et al., 2011, *Physical Review Letters*, **106**, 201101
- [4] Alonso D., Ferreira P. G., Santos M. G., 2014, *MNRAS*, **444**, 3183
- [5] Alonso D., Bull P., Ferreira P. G., Santos M. G., 2015, *MNRAS*, **447**, 400
- [6] Amin S., Ahmed B., Amin M., Abbasi M. I., Elahi A., Aftab U., 2017, in 2017 IEEE Asia Pacific Microwave Conference (APMC). pp 57–60, doi:10.1109/APMC.2017.8251376
- [7] Ansah-Narh T., Abdalla F. B., Smirnov O. M., Asad K. M. B., Shaw J. R., 2018, *MNRAS*, **481**, 2694
- [8] Asad K. M. B., et al., 2015, *MNRAS*, **451**, 3709
- [9] Asad K. M. B., et al., 2018, *MNRAS*, in preparation
- [10] Balanis C. A., 2005, Antenna Theory Analysis and Design. John Wiley & Sons, Inc, Hoboken, New Jersey
- [11] Battye R., et al., 2013, *MNRAS*, **434**, 1239
- [12] Bell M. R., Enßlin T. A., 2012, *A&A*, **540**, A80
- [13] Bennett C. L., et al., 2013, *ApJS*, **208**, 20
- [14] Booth R., Jonas J., 2012, African Skies, **16**, 101
- [15] Born M., Wolf E., 1980, Principles of Optics Electromagnetic Theory of Propagation, Interference and Diffraction of Light
- [16] Brentjens M. A., de Bruyn A. G., 2005, *A&A*, **441**, 1217
- [17] Brisken W., 2003, A cassegrain antenna simulator, A program for Cassegrain antenna modelling. <http://packages.ubuntu.com/lucid/cassbeam>
- [18] Burn B. J., 1966, *MNRAS*, **133**, 67

- [19] Calabretta M. R., Roukema B. F., 2007, MNRAS, 381, 865
- [20] Camera S., Santos M. G., Ferreira P. G., Maartens R., 2014, in Journal of Physics: Conference Series. p. 012004
- [21] Campbell C. E., 2003, Optometry & Vision Science, 80, 79
- [22] Cárcamo M., Román P. E., Casassus S., Moral V., Rannou F. R., 2018, Astronomy and computing, 22, 16
- [23] Carozzi T. D., 2015, in 2015 1st URSI Atlantic Radio Science Conference (URSI AT-RASC). pp 1–1, [doi:10.1109/URSI-AT-RASC.2015.7303206](https://doi.org/10.1109/URSI-AT-RASC.2015.7303206)
- [24] Carozzi T., Woan G., 2011, IEEE Transactions on Antennas and Propagation, 59, 2058
- [25] Chai X., Liu B., Yu L., Yu S., Wu D., Liu L., 2016, Experimental Astronomy, 42, 301
- [26] Chang T.-C., Pen U.-L., Peterson J. B., McDonald P., 2008, Phys. Rev. Lett., 100, 091303
- [27] Chang T.-C., Pen U.-L., Bandura K., Peterson J. B., 2010, Nature, 466, 463
- [28] Charman W., 2005, Contact Lens and Anterior Eye, 28, 75
- [29] Chong-Yaw Wee Paramesran R., Takeda F., 2004, in 2004 IEEE Region 10 Conference TENCON 2004.. pp 203–206 Vol. 1, [doi:10.1109/TENCON.2004.1414392](https://doi.org/10.1109/TENCON.2004.1414392)
- [30] Condon J. J., Ransom S. M., 2016, Essential radio astronomy. Princeton University Press
- [31] Decker F.-J., 1994, 6th workshop on beam instrumentation, Beam Distributions Beyond RMS. Standford Linear Accelerator Center, University of Stanford
- [32] Deng X., et al., 2017, Publications of the Astronomical Society of Australia, 34
- [33] Dewdney P., Turner W., Braun R., Santander-Vela J., Waterson N., Tan G., 2015, SKA document SKA-TEL-SKO-0000308
- [34] Dulwich F., Mort B. J., Salvini S., Zarb Adami K., Jones M. E., 2009, in Wide Field Astronomy & Technology for the Square Kilometre Array. p. 31
- [35] Ellingson S., Craig J., Dowell J., Taylor G., Helmboldt J., 2013, in Phased Array Systems & Technology, 2013 IEEE International Symposium on. pp 776–783
- [36] Emerson D. T., Graeve R., 1988, A&A, 190, 353
- [37] Faulkner A. J., 2011, in 2011 XXXth URSI General Assembly and Scientific Symposium. pp 1–4, [doi:10.1109/URSIGASS.2011.6051208](https://doi.org/10.1109/URSIGASS.2011.6051208)

- [38] Ferrara A., Ellis R., 2008, First Light in the Universe. Saas-Fee Advanced Course. Springer
- [39] Ferreira C., Lopez J. L., Navarro R., Perez Sinusia E., 2015, preprint, ([arXiv:1506.07396](https://arxiv.org/abs/1506.07396))
- [40] Fleisch D., 2008, A student's guide to Maxwell's equations. Cambridge University Press
- [41] Foley A., et al., 2016, Monthly Notices of the Royal Astronomical Society, 460, 1664
- [42] Foster G., 2015, Research report, Required Instrumentation Information for Interferometrists and Radio Astronomers. RATT, Department of Physics and Electronics, Rhodes University
- [43] Garrett M. A., 2013, in AFRICON, 2013. pp 1–5
- [44] Garrett M. A., et al., 2010, preprint, ([arXiv:1008.2871](https://arxiv.org/abs/1008.2871))
- [45] Gaylard M., 2012, Technical report, Radio Astronomy with a Single-Dish Radio Telescope. Hartebeesthoek Radio Astronomy Observatory
- [46] Gong Y., Cooray A., Silva M. B., Santos M. G., Lubin P., 2011, *ApJ*, **728**, L46
- [47] Gong Y., Cooray A., Silva M., Santos M. G., Bock J., Bradford C. M., Zemcov M., 2012, *ApJ*, **745**, 49
- [48] Górski K. M., Hivon E., Banday A. J., Wandelt B. D., Hansen F. K., Reinecke M., Bartelmann M., 2005, *ApJ*, **622**, 759
- [49] Gu J., Xu H., Wang J., An T., Chen W., 2013, *ApJ*, **773**, 38
- [50] Hamaker J. P., Bregman J. D., Sault R. J., 1996, *A&AS*, **117**, 137
- [51] Hampshire D. P., 2018, *Philosophical Transactions of the Royal Society A: Mathematical, Physical and Engineering Sciences*, 376, 20170447
- [52] Haslam C. G. T., Klein U., Salter C. J., Stoffel H., Wilson W. E., Cleary M. N., Cooke D. J., Thomasson P., 1981, *A&A*, **100**, 209
- [53] Haslam C. G. T., Salter C. J., Stoffel H., Wilson W. E., 1982, *A&A*, **47**, 1
- [54] Herron C. A., et al., 2018, *ApJ*, **855**, 29
- [55] Högbom J., 1974, *Astronomy and Astrophysics Supplement Series*, 15, 417
- [56] Jelić V., Zaroubi S., Labropoulos P., Bernardi G., de Bruyn A. G., Koopmans L. V. E., 2010, *MNRAS*, **409**, 1647
- [57] Johnston S., Feain I. J., Gupta N., 2009, arXiv preprint arXiv:0903.4011

- [58] Jonas J., Team M., 2018, MeerKAT Science: On the Pathway to the SKA (MeerKAT2016), eds Taylor P., Camilo F., Leeuw L., Moodley K. (International School for Advanced Studies, Trieste, Italy), 277
- [59] Jones R. C., 1942, Journal of the Optical Society of America (1917-1983), **32**, 486
- [60] Jones R. C., 1948, Journal of the Optical Society of America (1917-1983), **38**, 671
- [61] Khotanzad A., Lu J.-H., 1990, IEEE Transactions on Acoustics, Speech, and Signal Processing, 38, 1028
- [62] Klessen R. S., Glover S. C., 2016, in , Star Formation in Galaxy Evolution: Connecting Numerical Models to Reality. Springer, pp 85–249
- [63] Knee L. B., Brunt C. M., 2001, Nature, 412, 308
- [64] Kogut A., et al., 2007, *ApJ*, **665**, 355
- [65] Krachmalnicoff N., Baccigalupi C., Aumont J., Bersanelli M., Mennella A., 2016, *A&A*, **588**, A65
- [66] Kraus J. D., 1966, Radio Astronomy. McGraw-Hill, Inc, New York
- [67] La Porta L., Burigana C., Reich W., Reich P., 2008, *A&A*, **479**, 641
- [68] Labate M. G., Braun R., Dewdney P., Waterson N., Wagg J., 2017, in 2017 XXXIIInd General Assembly and Scientific Symposium of the International Union of Radio Science (URSI GASS). pp 1–4, [doi:10.23919/URSIGASS.2017.8105424](https://doi.org/10.23919/URSIGASS.2017.8105424)
- [69] Lakshminarayanan V., Fleck A., 2011, Journal of Modern Optics, 58, 545
- [70] Lidz A., Furlanetto S. R., Oh S. P., Aguirre J., Chang T.-C., Dore O., Pritchard J. R., 2011, *Astrophys. J.*, 741, 70
- [71] Lightman A., 1979, Radiative Processes in Astrophysics Wiley Interscience
- [72] Loeb A., Wyithe J. S. B., 2008, *Physical Review Letters*, **100**, 161301
- [73] Lonsdale C. J., et al., 2009, *IEEE Proceedings*, **97**, 1497
- [74] Makoni M., 2018, *Physics World*, **31**, 8
- [75] Miville-Deschénes M.-A., Ysard N., Lavabre A., Ponthieu N., Macías-Pérez J. F., Aumont J., Bernard J. P., 2008, *A&A*, **490**, 1093
- [76] Mort B. J., Dulwich F., Salvini S., Adami K. Z., Jones M. E., 2010, in Phased Array Systems and Technology (ARRAY), 2010 IEEE International Symposium on. pp 690–694

- [77] Newburgh L. B., et al., 2014, in Ground-based and Airborne Telescopes V. p. 91454V
- [78] Noll R. J., 1976, Journal of the Optical Society of America (1917-1983), **66**, 207
- [79] Norhazman H., Jalil N. A., 2012, in 2012 Sixth Asia Modelling Symposium. pp 81–86, [doi:10.1109/AMS.2012.45](https://doi.org/10.1109/AMS.2012.45)
- [80] Oosterloo T., Verheijen M., van Cappellen W., Bakker L., Heald G., Ivashina M., 2009, arXiv preprint arXiv:0912.0093
- [81] Oppermann N., et al., 2012, *A&A*, **542**, A93
- [82] Padmanabhan H., 2017, arXiv preprint arXiv:1706.01471
- [83] Padmanabhan H., 2018, *MNRAS*, **475**, 1477
- [84] Parsons A. R., et al., 2010, *The Astronomical Journal*, **139**, 1468
- [85] Perley R., Sowinski K., et al. 2015, Evla memo xxx, Optimizing VLA Antenna Performance
- [86] Peterson J. B., et al., 2009, in astro2010: The Astronomy and Astrophysics Decadal Survey. p. 234 ([arXiv:0902.3091](https://arxiv.org/abs/0902.3091))
- [87] Planck Collaboration et al., 2016a, *A&A*, **594**, A8
- [88] Planck Collaboration et al., 2016b, *A&A*, **594**, A10
- [89] Pogany T. K., Nadarajah S., 2009, Research Report 18, On the characteristic function of the generalized normal distribution. Probability and Statistics Group School of Mathematics, The University of Manchester
- [90] Rahmat-Samii Y., Williams L. I., Yaccarino R. G., 1995, *IEEE Antennas and Propagation Magazine*, **37**, 16
- [91] Rau U., Bhatnagar S., Voronkov M. A., Cornwell T. J., 2009, Proc. IEEE, 97
- [92] Remazeilles M., Dickinson C., Banday A. J., Bigot-Sazy M. A., Ghosh T., 2015, *MNRAS*, **451**, 4311
- [93] Renil R., van Rooyen R., 2018, in Society of Photo-Optical Instrumentation Engineers (SPIE) Conference Series. p. 107041U, [doi:10.1117/12.2312482](https://doi.org/10.1117/12.2312482)
- [94] Robishaw T., Quataert E., Heiles C., 2008, *ApJ*, **680**, 981
- [95] Roy J., Bhattacharyya B., Gupta Y., 2012, *MNRAS*, **427**, L90
- [96] Saha R., Jain P., Souradeep T., 2006, *ApJ*, **645**, L89

- [97] Santiago B. X., Strauss M. A., Lahav O., Davis M., Dressler A., Huchra J. P., 1995, *ApJ*, **446**, 457
- [98] Santiago B. X., Strauss M. A., Lahav O., Davis M., Dressler A., Huchra J. P., 1996, *ApJ*, **461**, 38
- [99] Santos M. G., Cooray A., Knox L., 2005, *ApJ*, **625**, 575
- [100] Santos M., et al., 2015, in Advancing Astrophysics with the Square Kilometre Array (AASKA14). p. 19 ([arXiv:1501.03989](https://arxiv.org/abs/1501.03989))
- [101] Santos M. G., et al., 2017, in Proceedings, MeerKAT Science: On the Pathway to the SKA (MeerKAT2016): Stellenbosch, South Africa, May 25-27, 2016. ([arXiv:1709.06099](https://arxiv.org/abs/1709.06099))
- [102] Schediwy S., Gozzard D., Gravestock C., Stobie S., Whitaker R., Malan J., Boven P., Grainge K., 2018a, arXiv e-prints, p. [arXiv:1805.11455](https://arxiv.org/abs/1805.11455)
- [103] Schediwy S., et al., 2018b, in American Astronomical Society Meeting Abstracts #231. p. 215.03
- [104] Schramm D. N., Galeotti P., 1997, Generation of Cosmological Large-Scale Structure. Kluwer Academic, Netherlands
- [105] Shaw J. R., Sigurdson K., Pen U.-L., Stebbins A., Sitwell M., 2014, *ApJ*, **781**, 57
- [106] Shaw J. R., Sigurdson K., Sitwell M., Stebbins A., Pen U.-L., 2015, Physical Review D, **91**, 083514
- [107] Silva M., Santos M. G., Cooray A., Gong Y., 2015, *ApJ*, **806**, 209
- [108] Smirnov O. M., 2011, *A&A*, **527**, A106
- [109] Smoot G. F., 1999, arXiv e-prints, pp [astro-ph/9902201](https://arxiv.org/abs/astro-ph/9902201)
- [110] Souradeep T., Saha R., Jain P., 2006, *New A Rev.*, **50**, 854
- [111] Stark D. P., et al., 2017, *MNRAS*, **464**, 469
- [112] Sudarvizhi D., 2016, in 2016 International Conference on Recent Trends in Information Technology (ICRTIT). pp 1–6, doi:[10.1109/ICRTIT.2016.7569541](https://doi.org/10.1109/ICRTIT.2016.7569541)
- [113] Tapken C., Appenzeller I., Noll S., Richling S., Heidt J., Meinkoehn E., Mehlert D., 2007, *Astron. Astrophys.*
- [114] Taylor A. R., Jarvis M., 2017, in IOP Conference Series: Materials Science and Engineering. p. 012014

- [115] Teh C.-H., Chin R. T., 1988, in Proceedings CVPR'88: The Computer Society Conference on Computer Vision and Pattern Recognition. pp 556–561
- [116] Testori J. C., Reich P., Reich W., 2008, *A&A*, **484**, 733
- [117] Thompson A. R., Bracewell R. N., 1974, *Astro. J.*, **79**
- [118] Thompson A. R., Moran J., Swenson G., 2001, Interferometry and Synthesis in Radio Astronomy, 2nd edition. John Wiley & Sons Inc.
- [119] Vallini L., Pallottini A., Ferrara A., Gallerani S., Sobacchi E., Behrens C., 2017, *Monthly Notices of the Royal Astronomical Society*, **473**, 271
- [120] Vermij E., Fiorin L., Hagleitner C., Bertels K., 2014, in International Supercomputing Conference. pp 35–52
- [121] White M., 1998, *Phys. Rev. D*, **57**, 5273
- [122] Wijnholds S., van der Tol S., Nijboer R., van der Veen A.-J., 2010, *IEEE Signal Processing Magazine*, **27**, 30
- [123] Wilson T. L., Rohlfs K., Hüttemeister S., 2009, Tools of Radio Astronomy. Springer-Verlag, Berlin, Germany
- [124] Wilson T. L., Rohlfs K., Hüttemeister S., 2013, Tools of radio astronomy. Springer Science & Business Media
- [125] Wolleben M., Landecker T. L., Reich W., Wielebinski R., 2006, *A&A*, **448**, 411
- [126] Wolleben M., et al., 2009, in Strassmeier K. G., Kosovichev A. G., Beckman J. E., eds, IAU Symposium Vol. 259, Cosmic Magnetic Fields: From Planets, to Stars and Galaxies. pp 89–90 ([arXiv:0812.2450](https://arxiv.org/abs/0812.2450)), doi:10.1017/S1743921309030117
- [127] Wolleben M., Landecker T., Hovey G., Messing R., Davison O., House N., Somaratne K., Tashev I., 2010, *The Astronomical Journal*, **139**, 1681
- [128] Wolz L., Abdalla F. B., Blake C., Shaw J. R., Chapman E., Rawlings S., 2014, *MNRAS*, **441**, 3271
- [129] Wolz L., et al., 2015, Advancing Astrophysics with the Square Kilometre Array (AASKA14), p. 35
- [130] Woudt P. A., Fender R. P., Armstrong R. P., Carignan C., 2013, *South African Journal of Science*, **109**, 01
- [131] Wyant J. C., Creath K., 1992, *Applied optics and optical engineering*, **11**, 28
- [132] Yue B., Ferrara A., Pallottini A., Gallerani S., Vallini L., 2015, *MNRAS*, **450**, 3829

- [133] Zitrin A., et al., 2015, *ApJ*, **810**, L12
- [134] de Villiers M., 2015, in 2015 IEEE International Symposium on Antennas and Propagation USNC/URSI National Radio Science Meeting. pp 1526–1527, doi:[10.1109/APS.2015.7305152](https://doi.org/10.1109/APS.2015.7305152)
- [135] van Cappellen W., de Vaate J. G. B., Warnick K., Veidt B., Gough R., Jackson C., Roddis N., 2011, in 2011 XXXth URSI General Assembly and Scientific Symposium. pp 1–4, doi:[10.1109/URSIGASS.2011.6051207](https://doi.org/10.1109/URSIGASS.2011.6051207)